Monthly Notices
of the
ROYAL ASTRONOMICAL SOCIETY

MNRAS **433,** 457–497 (2013) doi:10.1093/mnras/stt740
Advance Access publication 2013 June 4

76 T dwarfs from the UKIDSS LAS: benchmarks, kinematics and an updated space density

Ben Burningham,[1,2]★ C. V. Cardoso,[1,3] L. Smith,[1] S. K. Leggett,[4] R. L. Smart,[3] A. W. Mann,[5] S. Dhital,[6] P. W. Lucas,[1] C. G. Tinney,[7,8] D. J. Pinfield,[1] Z. Zhang,[1] C. Morley,[9] D. Saumon,[10] K. Aller,[5] S. P. Littlefair,[11] D. Homeier,[12,13] N. Lodieu,[14,15] N. Deacon,[16] M. S. Marley,[17] L. van Spaandonk,[1] D. Baker,[1] F. Allard,[13] A. H. Andrei,[2,3,18,19] J. Canty,[1] J. Clarke,[1] A. C. Day-Jones,[1,20] T. Dupuy,[21] J. J. Fortney,[9] J. Gomes,[1] M. Ishii,[22] H. R. A. Jones,[1] M. Liu,[5] A. Magazzú,[23] F. Marocco,[1] D. N. Murray,[1] B. Rojas-Ayala[24] and M. Tamura[25]

[1]*Centre for Astrophysics Research, Science and Technology Research Institute, University of Hertfordshire, Hatfield AL10 9AB, UK*
[2]*Observatório Nacional, Rua General José Cristino, 77 – São Cristóvão, Rio de Janeiro – RJ 20921-400, Brazil*
[3]*Istituto Nazionale di Astrofisica, Osservatorio Astrofisico di Torino, Strada Osservatorio 20, I-10025 Pino Torinese, Italy*
[4]*Gemini Observatory, 670 N. A'ohoku Place, Hilo, HI 96720, USA*
[5]*Institute for Astronomy, University of Hawai'i, 2680 Woodlawn Drive, Honolulu, HI 96822, USA*
[6]*Department of Astronomy, Boston University, 725 Commonwealth Ave, Boston, MA 02215, USA*
[7]*Australian Centre for Astrobiology, University of New South Wales, NSW 2052, Australia*
[8]*School of Physics, University of New South Wales, NSW 2052, Australia*
[9]*Department of Astronomy and Astrophysics, University of California, Santa Cruz, CA 95064, USA*
[10]*Los Alamos National Laboratory, PO Box 1663, MS F663, Los Alamos, NM 87545, USA*
[11]*Department of Physics and Astronomy, University of Sheffield, Sheffield S3 7RH, UK*
[12]*Institut fur Astrophysik, Georg-August-Universitat, Friedrich-Hund-Platz 1, D-37077 Gottingen, Germany*
[13]*C.R.A.L. (UMR 5574 CNRS), Ecole Normale Superieure, F-69364 Lyon Cedex 07, France*
[14]*Instituto de Astrofísica de Canarias (IAC), Calle Vía Láctea s/n, E-38200 La Laguna, Tenerife, Spain*
[15]*Instituto de Astrofísica de Canarias, E-38200 La Laguna, Spain*
[16]*Max Planck Institute for Astronomy, Koenigstuhl 17, D-69117 Heidelberg, Germany*
[17]*NASA Ames Research Center, Mail Stop 245-3, Moffett Field, CA 94035, USA*
[18]*Shanghai Astronomical Observatory/CAS, 80 Nandan Road, Shanghia 200030, China*
[19]*Observatório do Valongo/UFRJ, Ladeira Pedro Antonio 43, Rio de Janeiro – RJ 20080-090, Brazil*
[20]*Universidad de Chile, Camino el Observatorio # 1515, Santiago, Casilla 36-D, Chile*
[21]*Harvard–Smithsonian Center for Astrophysics, 60 Garden Street, Cambridge, MA 02138, USA*
[22]*Subaru Telescope, 650 North A'ohoku Place, Hilo, HI 96720, USA*
[23]*Fundación Galileo Galilei – INAF, Apartado 565, E-38700 Santa Cruz de La Palma, Spain*
[24]*Department of Astrophysics, American Museum of Natural History, Central Park West at 79th Street, New York, NY 10024, USA*
[25]*National Astronomical Observatory, Mitaka, Tokyo 181-8588, Japan*

Accepted 2013 April 26. Received 2013 April 23; in original form 2013 February 7

ABSTRACT

We report the discovery of 76 new T dwarfs from the UKIRT Infrared Deep Sky Survey (UKIDSS) Large Area Survey (LAS). Near-infrared broad- and narrow-band photometry and spectroscopy are presented for the new objects, along with *Wide-field Infrared Survey Explorer* (*WISE*) and warm-*Spitzer* photometry. Proper motions for 128 UKIDSS T dwarfs are presented from a new two epoch LAS proper motion catalogue. We use these motions to identify two new benchmark systems: LHS 6176AB, a T8p+M4 pair and HD 118865AB, a T5.5+F8 pair. Using age constraints from the primaries and evolutionary models to constrain the radii, we have estimated their physical properties from their bolometric luminosity. We compare the colours and properties of known benchmark T dwarfs to the latest model atmospheres and draw two principal conclusions. First, it appears that the $H - [4.5]$ and $J - W2$ colours are more sensitive to metallicity than has previously been recognized, such that differences in

★ E-mail: b.burningham@herts.ac.uk

metallicity may dominate over differences in $T_{\rm eff}$ when considering relative properties of cool objects using these colours. Secondly, the previously noted apparent dominance of young objects in the late-T dwarf sample is no longer apparent when using the new model grids and the expanded sample of late-T dwarfs and benchmarks. This is supported by the apparently similar distribution of late-T dwarfs and earlier type T dwarfs on reduced proper motion diagrams that we present. Finally, we present updated space densities for the late-T dwarfs, and compare our values to simulation predictions and those from *WISE*.

Key words: surveys – brown dwarfs – stars: low-mass.

1 INTRODUCTION

The current generation of wide-field surveys is bringing about a step change in our understanding of the coolest and lowest mass components of the solar neighbourhood. The total number of cool T dwarfs, substellar objects with $1400 \gtrsim T_{\rm eff} \gtrsim 500$ K, has been taken into the hundreds by infrared surveys such as the UKIRT Infrared Deep Sky Survey (UKIDSS; Lawrence et al. 2007), the Canada-France Brown Dwarf Survey (CFBDS; e.g. Delorme et al. 2010) and most recently the *Wide-field Infrared Survey Explorer* (*WISE*; Wright et al. 2010). The last of these, which is an all-sky mid-infrared survey, has extended the substellar census to well below $T_{\rm eff} = 500$ K, and the adoption of a new spectral class 'Y' has been suggested to classify these new extremely cool objects (Cushing et al. 2011; Kirkpatrick et al. 2012). The VISTA Hemisphere Survey (VHS; McMahon et al., in preparation) and VIKING survey are now also adding to the census (Lodieu et al. 2012c; Pinfield et al. 2012).

Our exploitation of the UKIDSS Large Area Survey (LAS) has focused on using the photometric characteristics of mid-to late-T dwarfs at red optical and near-infrared (NIR) wavelengths (see e.g. Kirkpatrick 2005 for a review of the L and T spectral classes) to select a statistically complete sample of T dwarfs across the T6–T8+ range (Lodieu et al. 2007b; Pinfield et al. 2008; Burningham et al. 2010b). This allowed us to identify an apparent dearth of late-T dwarfs in the solar neighbourhood compared to Monte Carlo simulations based on functional forms of the initial mass function (IMF) that have been fitted to observations of the substellar component of young clusters (Pinfield et al. 2008; Burningham et al. 2010b).

Interpreting this result is hampered by the inherently indirect nature of the observations, and the problems associated with determining the properties of a mixed-age population of brown dwarfs, which by their nature have no single mass–radius relationship. Leggett et al. (2010a) found that colours of the late-T dwarfs that were identified in UKIDSS suggest they are a predominantly young and low-mass population from comparisons to the model atmospheres of Saumon & Marley (2008). This surprising result could have significant bearing on the interpretation of observed space densities of late-T dwarfs.

Benchmark brown dwarfs provide the opportunity to break the degeneracies in age, mass and metallicity that hamper the characterization of cool substellar objects (Pinfield et al. 2006). As part of our search of the UKIDSS LAS, and more recently *WISE* and VISTA, we have identified several wide binary systems that allow fiducial constraints to be placed on the properties of the T dwarf secondary component (Burningham et al. 2009, 2011; Day-Jones et al. 2011; Pinfield et al. 2012). Comparisons of these objects with both the BT Settl (Allard, Homeier & Freytag 2010) model colours, and those of Saumon & Marley (2008) also appear to support the result of Leggett et al. (2010a).

In this paper, we present the results of the extension of our search of the UKIDSS LAS up to and including the sky available in Data Release 9 (DR9), with near-complete follow-up of Data Release 8 (DR8). We have used the significantly enhanced sample of late-T dwarfs, along with two epoch UKIDSS LAS proper motions from the catalogue of Smith et al. (in preparation) to perform a systematic search for wide binary benchmark objects, and compare the observed properties of the benchmark sample and the wider UKIDSS sample with the latest model prediction from Saumon et al. (2012) and Morley et al. (2012). We also use the proper motions for our sample to briefly investigate the kinematics of UKIDSS T dwarfs. Finally, we provide an updated estimate of the space densities of T6–T8+ dwarfs, and discuss possible routes to reconciling the observations of the field and young clusters.

2 CANDIDATE SELECTION

Our initial candidate selection followed a similar method to that described in Pinfield et al. (2008) and Burningham et al. (2010b), which we summarize here. The selection process consists of two channels: (1) those sources that are detected in the three UKIDSS LAS *YJH* bands (the *YJH* channel); and (2) those sources that are only detected in the *YJ* bands (the *YJ*-only channel). We did not employ *WISE* data for guiding our selection since the all-sky catalogue became available part way through our follow-up campaign, and consistent selection is crucial for establishing a well-characterized statistical sample. Additionally, for fainter T6 and earlier dwarfs, the *WISE* faint limits are effectively shallower than the UKIDSS LAS.

2.1 The *YJH* selection channel

Our *YJH* selection channel requires sources to lie within the UKIDSS LAS sky that overlaps with the Sloan Digital Sky Survey (SDSS) DR8 footprint and have the following photometric characteristics:

(i) $J - H < 0.1$
(ii) $J - K < 0.1$ or K band non-detection
(iii) $z' - J > 2.5$ or no SDSS detection within 2 arcsec.

We also imposed a number of data quality constraints to minimize contamination from artefacts and poor signal-to-noise (S/N) data for which we refer the reader to Appendix A, which includes the SQL queries we used to access the LAS via the WFCAM Science Archive (WSA; Hambly et al. 2008). The epoch difference between the UKIDSS data and SDSS data is variable and ranges up to six years. Our inclusion of UKIDSS sources with no SDSS counterpart within 2 arcsec introduced sources with $z' - J < 2.5$ and proper motions above $\sim$300 mas yr^{-1} to our candidate list. This source of contamination was relatively small and in most cases such objects were identified as fast moving earlier type objects prior to detailed follow-up. Figs 1 and 2 show the UKIDSS LAS *YJH* photometry of our selected candidates from DR5 to DR8. The greatest degree of contamination in our *YJH* selection channel is from photometrically

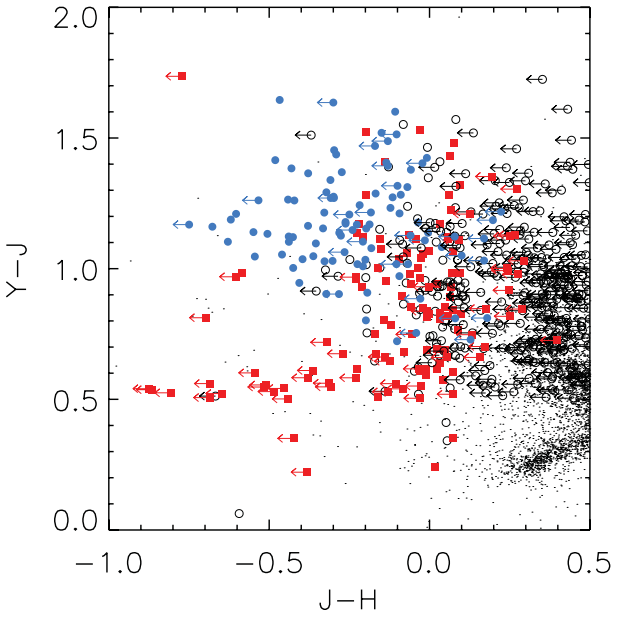

Figure 1. *YJH* colour–colour plot showing UKIDSS LAS photometry of candidate T dwarfs from DR5 to DR8. Confirmed T dwarfs are shown with blue filled circles, with arrows indicating limits on $J - H$ colours for candidates from the *YJ*-only channel. Limits are for illustrative purposes, and are based on the canonical 5σ depth for the LAS of $H = 18.8$. Rejected candidates are shown with filled red squares, whilst yet-to-be followed-up targets are shown with black open circles. For reference, field stars from a randomly selected 1 square degree region of LAS sky are shown as black dots.

scattered M dwarfs, with the greatest frequency of contaminants found at faint J, blue $Y - J$ and red $J - H$.

2.2 The *YJ*-only selection channel

Our *YJ*-only selection channel ensures that we do not exclude bona fide late-T dwarfs that are fainter than the LAS H-band detection limit due to the inherently blue $J - H$ colours of such objects. To minimize contamination from scattered and blue M dwarfs we impose a $Y - J$ constraint for this selection, such that our photometric criteria are:

(i) $Y - J > 0.5$ or $J < 18.5$
(ii) H and K band non-detection
(iii) $z' - J > 2.5$ or no SDSS detection within 2 arcsec.

We applied the same data quality restrictions to the *YJ*-only channel as were applied to *YJH* selection channel. In addition, to minimize contamination from Solar system Objects (SSOs), which can appear as non-detections in the H and K bands due to different epochs of observation, we also imposed a criterion that Y- and J-band coordinates must agree to within 0.75 arcsec for observations taken within a day of each other. For observations taken more than a day apart, we remove this requirement to avoid excluding bona fide candidates with high proper motion. We again refer the reader to Appendix A for details of the SQL queries that we used to access the WSA. The additional SSO contamination present in the *YJ*-only selection channel can be seen in Fig. 2 as relatively bright and blue $Y - J$ contaminants with very blue limits on their $J - H$ colours.

3 FOLLOW-UP PHOTOMETRY

To remove contaminants such as photometrically scattered M dwarfs and SSOs, we used a combination of NIR and optical photometry. We followed two distinct strategies in removing contaminants. Prior to 2010 December, we continued the strategy previously described in Burningham et al. (2010b). Briefly, this involved obtaining higher SNR H-band photometry to remove early-type objects that had been scattered into our $J - H < 0.1$ selection (or to fill in the missing data for H-band drop-outs in the *YJ*-only channel), and repeat J-band observations to remove SSOs. Whilst adequate for drawing a roughly complete sample of T4+ dwarfs, this method was unable to effectively prioritize objects with spectral types of T6 and later for follow-up. Since the T6–T9 region is most useful for constraining the form of the field mass function (e.g. Burgasser 2004), we revised our strategy to allow the rejection of most of the T4 dwarfs that dominated our Burningham et al. (2010b) sample.

Our revised strategy involved using relatively short exposure (15–30 min) z'-band imaging to confirm red $z' - J > 2.5$ colours for targets with no SDSS detection and for which the limits were not sufficient to rule out a bluer $z' - J$ colour. For targets from the *YJ*-only channel, this step was preceded by short J-band observations to remove SSO contaminants. Targets with confirmed $z' - J > 2.5$

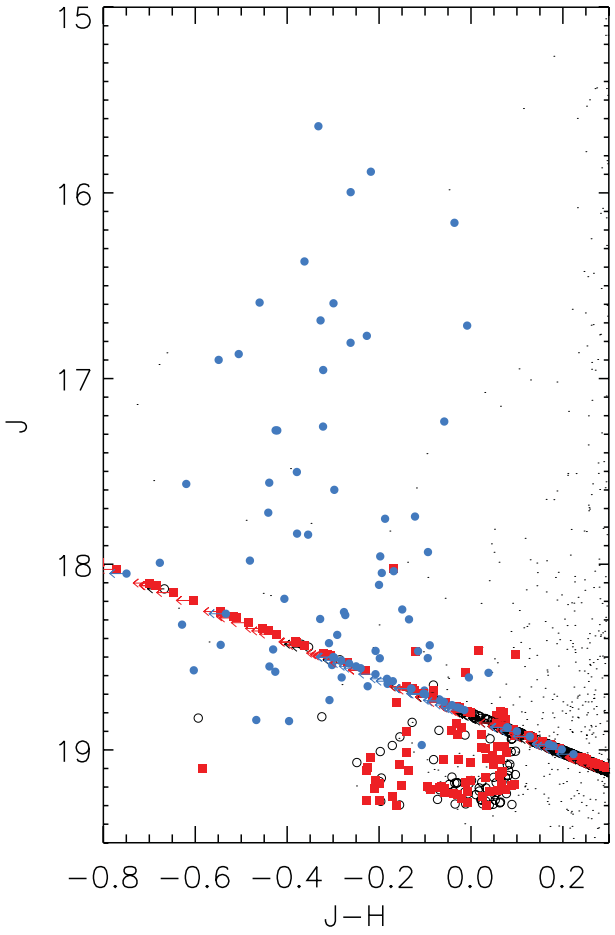

Figure 2. *JH* colour–magnitude plot showing UKIDSS LAS photometry of candidate T dwarfs from DR5 to DR8. Confirmed T dwarfs are shown with blue filled circles, with arrows indicating limits on $J - H$ colours for candidates from the *YJ*-only channel. Limits are for illustrative purposes, and are based on the canonical 5σ depth for the LAS of $H = 18.8$, this results in these candidates forming a straight diagonal sequence across the plot. Rejected candidates are shown with filled red squares, whilst yet-to-be followed-up targets are shown with open circles. For reference, field stars from a randomly selected 1 square degree region of LAS sky are shown as black dots.

were then targeted with CH_4 imaging to identify late-type T dwarfs. Targets with $CH_4s - CH_4l < -0.5$ were prioritized for spectroscopy based on the methane colours of T dwarfs reported by Tinney et al. (2005).

In the following subsections, we outline the photometric observations and data reduction that were carried out for this follow-up programme. Details of the observations carried out for each target are given in Appendix B.

3.1 Broad-band photometry

Our broad-band NIR photometry was obtained using the UKIRT Fast Track Imager (UFTI; Roche et al. 2003) and WFCAM (Casali et al. 2007), both mounted on UKIRT across a number of observing runs spanning 2009 to the end of 2010. UFTI data were dark subtracted, flat-field corrected, sky subtracted and mosaicked using the ORAC-DR pipeline.[1] WFCAM data were processed using the WFCAM science pipeline by the Cambridge Astronomical Surveys Unit (CASU) (Irwin et al. 2004), and archived at the WSA (Hambly et al. 2008). Observations consisted of a three-point jitter pattern in the *Y* and *J* bands, and five-point jitter patterns in the *H* and *K* bands repeated twice. All data were acquired with 2×2 microstepping. The WFCAM and UFTI filters are on the Mauna Kea Observatories (MKO) photometric system (Tokunaga, Simons & Vacca 2002).

The majority of our z' photometry was taken using the Device Optimized for the LOw RESolution (DOLORES; Molinari, Conconi & Pucillo 1997) at the Telescopio Nazionale Galileo (TNG). The observations were taken under programme AOT22 TAC 96 spanning from 2010 to 2012. DOLORES is equipped with a 2048 × 2048 pixels CCD with a field of view of 8.6 × 8.6 arcmin with a 0.252 arcsec pixel^{-1} scale. The observations were taken with the z' Sloan filter. A small number of targets were observed in the z' band using the using the ESO Faint Object Spectrograph and Camera (EFOSC2) mounted on the New Technology Telescope (NTT; programme 082.C-0399) and using the Auxiliary-port Camera (ACAM) on the William Herschel Telescope (WHT). For each epoch a set of standard calibration flat-fields and darks observations were taken. The images were dark subtracted, flat-fielded and in the case of multiple exposures combined using standard IRAF routines. The data were taken in different observing conditions, from photometric conditions to cirrus. No attempts to perform defringing to the images were made. The E2V4240 CCD detector in use in DOLORES has a low fringing level, the science object was also normally located in the top-right section of the CCD where fringing is even smaller. Photometry was performed with IRAF using a fixed circular aperture with radius 2 arcsec. The photometric zero-point was calibrated using the non-saturated SDSS stars present in the field of view.

The SDSS z' band filter is slightly peculiar in that it has no red cut-off. Instead, the red cut-off is defined by the detector sensitivity. So, although the DOLORES and ACAM data were taken through an SDSS z' band filter, this does not trivially lead to the photometry being on the SDSS system, since there may be differences in the detectors' long-wavelength responses. To check the consistency of the DOLORES and ACAM photometric systems with SDSS, we have compared synthetic photometry for a set of reference stellar spectra convolved with the combined filter and detector response curves for each of the systems. The difference was found to be much smaller than the typical scatter in the zero-point from the reference stars, which dominate our quoted errors, and so we did not correct the SDSS reference stars magnitudes before calibration. For objects as red as T dwarfs, however, the difference can be more significant. Synthesized photometry using template-T dwarf spectra found a mean offset of close to zero for DOLORES (z'(DOLORES) − z'(SDSS) = -0.02 ± 0.02). For ACAM, we found a small offset of z'(ACAM) − z'(SDSS) = $+0.09 \pm 0.03$.

For the EFOSC2 observations, a Gunn z-band filter (ESO Z#623) was used and we used the transform given in Burningham et al. (2009) to calculate $z_{\rm EFOSC2}$ for the SDSS secondary calibrators. To place the resulting $z_{\rm EFOSC2}$(AB) photometry on the Sloan z'(AB) system, we used the transform determined in Burningham et al. (2010b): z(EFOSC2) − z'(SDSS) = -0.19 ± 0.02.

The best available broad-band photometry for all targets presented here is given in Table 1.

3.2 CH_4 photometry

Differential methane photometry was obtained using the Near Infrared Camera Spectrometer (NICS; Baffa et al. 2001) mounted on the TNG under programme AOT22 TAC 96 spanning from 2010 to 2012. NICS contains a set of MKO NIR filters as specified by Tokunaga et al. (2002). More information about the narrow-band and intermediate-band sets are given by A. Tokunaga.[2] The methane filters used in this work are denoted as CH_4s and CH_4l. The comparison of these two filters provides information about the strength of the methane absorption bands in late-T dwarfs. CH_4l samples the methane absorption bands present between 1.6 and 1.8 μm, while the CH_4s samples a pseudo-continuum outside the methane band.

The final image mosaics were produced using the Speedy Near-infrared data Automatic Pipeline (SNAP) provided by TNG (version 1.3). SNAP is an automated wrapper of existing pieces of software (IRDR, IRAF, SEXTRACTOR and DRIZZLE) to perform a full reduction with a single command. SNAP performs flat-fielding, computes the offsets between the dithered images, creates a mosaic image with double-pass sky subtraction and correction for field distortion.

The data were taken in different observing conditions, from photometric conditions to cirrus. Photometry was performed with IMCORE, part of CASUTOOLS (version 1.0.21), using a fixed circular aperture of 2 arcsec. CASUTOOLS[3] is a suite of programs developed and used by the CASU for survey data reduction tasks associated with the UKIDSS and VISTA surveys, amongst others.

Differential photometric calibration of the methane colour $CH_4s - CH_4l$ was performed using the UKIDSS field stars present in the field, and the method defined by Tinney et al. (2005) in their section 2.5. Tinney et al. (2005) only provides the parametrization for the 2MASS system. Using the information available on their table 3, we performed the parametrization for the UKIDSS system avoiding the region $0.48 < (J-H)_{\rm MKO} < 0.512$ where the sequence is degenerate. The sequence was fitted with two separate quadratics to the regions $-0.050 < (J-H)_{\rm MKO} < 0.480$,

$$CH_4s - CH_4l = +0.000\,46 - 0.012\,59(J-H) + 0.318\,17(J-H)^2 \quad (1)$$

and $0.512 < (J-H)_{\rm MKO} < 1.000$,

$$CH_4s - CH_4l = -0.173\,17 + 0.927\,44(J-H) - 0.589\,69(J-H)^2. \quad (2)$$

[1] http://www.oracdr.org/

[2] See http://www.ifa.hawaii.edu/~tokunaga/NB_special_ordersorting.html.

[3] http://apm49.ast.cam.ac.uk/surveys-projects/software-release

Table 1. Best available NIR photometry for our sample. No superscript on a broad-band photometric value indicates UKIDSS survey photometry for *YJHK*, SDSS DR8 for z' band. Unless indicated otherwise, all CH_4 photometry is from TNG/NICS. Superscripts refer to the following instruments: A = ACAM (WHT); D = DOLORES (TNG); E = EFOSC2 (NTT); L = LIRIS(WHT); U = UFTI (UKIRT); W = WFCAM (UKIRT). z' band photometry has been converted to the SDSS system as described in the text.

Name	α (J2000)	δ (J2000)	z'	Y_{MKO}	J_{MKO}	H_{MKO}	K_{MKO}	$CH_4s - CH_4l$	CH_4 type	CH_4 type (min)	CH_4 type (max)	Spectral type
ULAS J000734.90+011247.1	00:07:34.90	+01:12:47.10	–	19.22 ± 0.07	18.05 ± 0.04	–	–	-0.91 ± 0.13	T6.1	T5.8	T6.4	T7
ULAS J012735.66+153905.9	01:27:35.66	+15:39:05.90	–	19.47 ± 0.13	18.22 ± 0.07	18.62 ± 0.14	–	-0.88 ± 0.17	T6.0	T5.5	T6.4	T6.5
ULAS J012855.07+063357.0	01:28:55.07	+06:33:57.00	22.73 ± 0.40^{A}	19.66 ± 0.14	18.93 ± 0.12	–	–	-0.81 ± 0.14	T5.8	T5.4	T6.2	T6
ULAS J013017.79+080453.9	01:30:17.79	+08:04:53.90	–	19.06 ± 0.03^{W}	17.93 ± 0.02^{W}	18.21 ± 0.02^{W}	18.35 ± 0.04^{W}	-0.72 ± 0.07	T5.5	T5.3	T5.7	T6
CFBDS J013302+023128[a]	01:33:02.48	+02:31:28.90	–	19.36 ± 0.11	18.34 ± 0.08	18.51 ± 0.15	–	<-1.19	N/A	N/A	N/A	T8
ULAS J013950.51+150307.6	01:39:50.51	+15:03:07.60	–	19.72 ± 0.17	18.44 ± 0.1	18.53 ± 0.18	–	-0.83 ± 0.11	T5.9	T5.6	T6.2	T7
ULAS J020013.18+090835.2	02:00:13.18	+09:08:35.20	–	18.98 ± 0.07	17.81 ± 0.04	18.18 ± 0.11	18.18 ± 0.2	-0.83 ± 0.11	T5.9	T5.5	T6.1	T6
ULAS J022603.18+070231.4	02:26:03.18	+07:02:31.40	–	19.62 ± 0.05^{W}	18.52 ± 0.04^{W}	18.82 ± 0.03^{W}	18.79 ± 0.06^{W}	–	N/A	N/A	N/A	T7
ULAS J024557.88+065359.4	02:45:57.88	+06:53:59.40	–	19.43 ± 0.1	18.36 ± 0.04^{W}	18.95 ± 0.17	–	–	N/A	N/A	N/A	T7
ULAS J025545.28+061655.8	02:55:45.28	+06:16:55.80	–	19.15 ± 0.07	18.04 ± 0.03^{W}	18.4 ± 0.02^{W}	–	–	N/A	N/A	N/A	T6
ULAS J032920.22+043024.5	03:29:20.22	+04:30:24.50	20.75 ± 0.17	18.55 ± 0.02^{W}	17.55 ± 0.02^{W}	17.89 ± 0.02^{W}	18.4 ± 0.04^{W}	–	N/A	N/A	N/A	T5
ULAS J074502.79+233240.3	07:45:02.79	+23:32:40.30	–	20.0 ± 0.15	18.88 ± 0.07	–	–	-1.62 ± 0.17	T7.6	T7.4	T7.9	T9[d]
ULAS J074616.98+235532.2	07:46:16.98	+23:55:32.20	$>20.99^{D}$	20.18 ± 0.19	19.0 ± 0.08	–	–	-0.87 ± 0.17^{L}	N/A	N/A	N/A	T7
ULAS J074720.07+245516.3	07:47:20.07	+24:55:16.30	–	19.35 ± 0.05^{W}	18.17 ± 0.05^{W}	18.5 ± 0.04^{W}	18.53 ± 0.07^{W}	–	N/A	N/A	N/A	T6.5
ULAS J075829.83+222526.7	07:58:29.83	+22:25:26.70	–	18.68 ± 0.04	17.62 ± 0.02^{W}	17.91 ± 0.02^{W}	17.87 ± 0.12	–	N/A	N/A	N/A	T6.5
ULAS J075937.75+185555.0	07:59:37.75	+18:55:55.00	23.32 ± 0.09^{D}	20.21 ± 0.18	18.7 ± 0.07	–	–	-0.95 ± 0.12	T6.2	T5.9	T6.5	T6
ULAS J080048.27+190823.8	08:00:48.27	+19:08:23.80	22.05 ± 0.16^{D}	19.76 ± 0.12	18.55 ± 0.06	–	–	-0.73 ± 0.28^{L}	N/A	N/A	N/A	N/A
ULAS J080918.41+212615.2	08:09:18.41	+21:26:15.20	–	19.65 ± 0.09	18.58 ± 0.03^{W}	18.99 ± 0.03^{W}	18.65 ± 0.22	–	N/A	N/A	N/A	T8
ULAS J081110.86+252931.8	08:11:10.86	+25:29:31.80	–	18.76 ± 0.03	17.57 ± 0.02	18.19 ± 0.12	18.02 ± 0.19	-1.03 ± 0.13	T6.4	T6.1	T6.7	T7
ULAS J081407.51+245200.9	08:14:07.51	+24:52:00.90	$>21.05^{D}$	19.6 ± 0.1	18.54 ± 0.05	–	–	-0.30 ± 0.10^{L}	N/A	N/A	N/A	T5p
ULAS J081507.26+271119.2	08:15:07.26	+27:11:19.20	–	19.48 ± 0.1	18.31 ± 0.03^{W}	18.6 ± 0.03^{W}	–	–	N/A	N/A	N/A	T7p
ULAS J081918.58+210310.4	08:19:18.58	+21:03:10.40	21.93 ± 0.08^{E}	18.25 ± 0.03	16.95 ± 0.01	17.28 ± 0.03	17.18 ± 0.06	–	N/A	N/A	N/A	T6
ULAS J082155.49+250939.6	08:21:55.49	+25:09:39.60	–	18.61 ± 0.04	17.23 ± 0.01^{W}	17.24 ± 0.01^{W}	17.23 ± 0.09	–	N/A	N/A	N/A	T4.5
ULAS J084743.93+035040.2	08:47:43.93	+03:50:40.20	21.90 ± 0.10^{A}	19.61 ± 0.05^{W}	18.53 ± 0.04^{W}	18.71 ± 0.03^{W}	18.99 ± 0.08^{W}	-0.65 ± 0.14	T5.3	T4.7	T5.7	N/A
ULAS J092608.82+040239.7	09:26:08.82	+04:02:39.70	–	19.7 ± 0.09	18.59 ± 0.06	–	–	-0.69 ± 0.14	T5.4	T4.9	T5.8	T6
ULAS J092744.20+341308.7	09:27:44.20	+34:13:08.70	$>21.8^{D}$	19.66 ± 0.14	18.77 ± 0.11	–	–	-1.27 ± 0.28	T7.0	T6.4	T7.5	T5.5
WISEP J092906.77+040957.9[b]	09:29:06.75	+04:09:57.70	–	17.89 ± 0.01^{W}	16.87 ± 0.01^{W}	17.24 ± 0.01^{W}	17.61 ± 0.02^{W}	-0.92 ± 0.07	T6.1	T6.0	T6.3	T7
ULAS J093245.48+310206.4	09:32:45.48	+31:02:06.40	–	20.0 ± 0.09	18.73 ± 0.05	19.04 ± 0.23	–	–	N/A	N/A	N/A	T2
ULAS J095047.28+011734.3	09:50:47.28	+01:17:34.30	–	18.9 ± 0.03^{W}	18.02 ± 0.03^{W}	18.4 ± 0.03^{W}	18.85 ± 0.07^{W}	–	N/A	N/A	N/A	T8p
ULAS J095429.90+062309.6	09:54:29.90	+06:23:09.60	–	17.73 ± 0.01^{W}	16.6 ± 0.01^{W}	16.87 ± 0.01^{W}	17.05 ± 0.01^{W}	-0.58 ± 0.09	T5.0	T4.6	T5.3	T5
ULAS J102144.87+054446.1	10:21:44.87	+05:44:46.10	–	18.82 ± 0.03^{W}	17.66 ± 0.02^{W}	17.96 ± 0.02^{W}	17.97 ± 0.03^{W}	-0.99 ± 0.26	T6.3	T5.6	T6.9	T6
ULAS J102305.44+044739.2	10:23:05.44	+04:47:39.20	23.50 ± 0.17^{D}	19.49 ± 0.05^{W}	18.39 ± 0.04^{W}	18.73 ± 0.04^{W}	18.58 ± 0.07^{W}	-0.52 ± 0.12^{L}	N/A	N/A	N/A	T6.5
ULAS J102940.52+093514.6	10:29:40.52	+09:35:14.60	–	18.24 ± 0.02^{W}	17.28 ± 0.01^{W}	17.63 ± 0.01^{W}	17.64 ± 0.02^{W}	-1.56 ± 0.17	T7.5	T7.3	T7.8	T8
ULAS J104224.20+121206.8	10:42:24.20	+12:12:06.80	–	19.58 ± 0.09	18.52 ± 0.06	18.9 ± 0.12	–	-0.93 ± 0.15	T6.2	T5.8	T6.5	T7.5p
ULAS J104355.37+104803.4	10:43:55.37	+10:48:03.40	–	19.21 ± 0.03^{W}	18.23 ± 0.02^{W}	18.58 ± 0.02^{W}	18.66 ± 0.05^{W}	-1.36 ± 0.22	T7.2	T6.7	T7.5	T8
ULAS J105134.32−015449.8	10:51:34.32	−01:54:49.80	–	18.85 ± 0.03^{W}	17.75 ± 0.02^{W}	18.07 ± 0.02^{W}	18.27 ± 0.04^{W}	-0.56 ± 0.14	T4.9	T4.4	T5.4	T6
ULAS J105334.64+015719.7	10:53:34.64	+01:57:19.70	–	19.77 ± 0.1	18.5 ± 0.06	–	–	-1.10 ± 0.16	T6.6	T6.2	T6.9	T6.5
ULAS J111127.77+051855.5	11:11:27.77	+05:18:55.50	–	19.87 ± 0.1	18.74 ± 0.07	–	–	–	N/A	N/A	N/A	T4.5
ULAS J113717.17+112657.2	11:37:17.17	+11:26:57.20	$>22.24^{D}$	20.14 ± 0.21	18.5 ± 0.09	–	–	-0.51 ± 0.16	T4.7	T4.0	T5.3	N/A
ULAS J115229.68+035927.3	11:52:29.68	+03:59:27.30	–	18.54 ± 0.03	17.28 ± 0.02	17.7 ± 0.05	17.77 ± 0.12	-0.69 ± 0.06	T5.4	T5.2	T5.6	T6
ULAS J115239.94+113407.6	11:52:39.94	+11:34:07.60	–	19.3 ± 0.06	18.26 ± 0.04	18.66 ± 0.1	18.32 ± 0.17	<-1.38	N/A	N/A	N/A	T8.5[d]
ULAS J115508.39+044502.3	11:55:08.39	+04:45:02.30	–	19.38 ± 0.07	18.33 ± 0.05	–	–	–	N/A	N/A	N/A	T7
ULAS J120444.67−015034.9	12:04:44.67	−01:50:34.90	–	17.99 ± 0.03	16.74 ± 0.02^{U}	17.1 ± 0.02^{U}	17.29 ± 0.09	–	N/A	N/A	N/A	T4.5

Table 1 – *continued*

Name	α (J2000)	δ (J2000)	z'	Y_{MKO}	J_{MKO}	H_{MKO}	K_{MKO}	$CH_4s - CH_4l$	CH_4 type	CH_4 type (min)	CH_4 type (max)	Spectral type
ULAS J120621.03+101802.9	12:06:21.03	+10:18:02.90	–	20.57 ± 0.23	19.11 ± 0.15^{W}	19.53 ± 0.09^{W}	–	–	N/A	N/A	N/A	T5
ULAS J121226.80+101007.4	12:12:26.80	+10:10:07.40	–	20.48 ± 0.25	18.69 ± 0.09^{W}	19.06 ± 0.08^{W}	–	–	N/A	N/A	N/A	T5
ULAS J122343.35-013100.7	12:23:43.35	−01:31:00.70	–	19.71 ± 0.13	18.7 ± 0.09	–	–	-0.66 ± 0.16	T5.3	T4.7	T5.8	T6
ULAS J125446.35+122215.7	12:54:46.35	+12:22:15.70	–	19.51 ± 0.11	18.29 ± 0.06	18.62 ± 0.17	18.26 ± 0.2	-0.56 ± 0.19	T4.9	T4.1	T5.6	N/A
ULAS J125835.97+030736.1	12:58:35.97	+03:07:36.10	–	19.7 ± 0.14	18.38 ± 0.05^{W}	18.59 ± 0.05^{W}	–	–	N/A	N/A	N/A	T5
ULAS J125939.44+293322.4	12:59:39.44	+29:33:22.40	–	19.65 ± 0.09	18.39 ± 0.06	18.55 ± 0.14	–	-0.59 ± 0.13	T5.0	T4.5	T5.4	T5
ULAS J130227.54+143428.0	13:02:27.54	+14:34:28.00	$>19.12^{D}$	19.75 ± 0.13	18.6 ± 0.04^{W}	18.8 ± 0.04^{W}	–	-0.23 ± 0.10	T3.1	T2.4	T3.7	T4.5
ULAS J133502.11+150653.5	13:35:02.11	+15:06:53.50	–	19.03 ± 0.03^{U}	17.97 ± 0.02^{U}	18.3 ± 0.03^{U}	18.23 ± 0.14	-0.60 ± 0.09	T5.1	T4.8	T5.4	T6
ULAS J133828.69−014245.4	13:38:28.69	−01:42:45.40	–	19.57 ± 0.08^{W}	18.69 ± 0.1^{W}	19.14 ± 0.09^{W}	19.21 ± 0.12^{W}	–	N/A	N/A	N/A	T7.5
ULAS J133933.64−005621.1	13:39:33.64	−00:56:21.10	–	19.21 ± 0.05^{W}	18.24 ± 0.05^{W}	18.48 ± 0.04^{W}	18.39 ± 0.05^{W}	–	N/A	N/A	N/A	T7
ULAS J133943.79+010436.4	13:39:43.79	+01:04:36.40	–	19.15 ± 0.05^{W}	18.08 ± 0.04	18.39 ± 0.13	18.39 ± 0.05^{W}	–	N/A	N/A	N/A	T5
ULAS J141756.22+133045.8	14:17:56.22	+13:30:45.80	20.42 ± 0.16	17.94 ± 0.03	16.77 ± 0.01	17.0 ± 0.03	17.0 ± 0.04	-0.51 ± 0.08	T4.7	T4.4	T5.0	T5
ULAS J142145.63+013619.0	14:21:45.63	+01:36:19.00	–	19.31 ± 0.12	18.52 ± 0.04^{W}	18.54 ± 0.03^{W}	–	–	N/A	N/A	N/A	T4.5
ULAS J142536.35+045132.3	14:25:36.35	+04:51:32.30	$>21.87^{D}$	20.02 ± 0.14	18.7 ± 0.09	–	–	-0.93 ± 0.12	T6.2	T5.9	T6.4	T6.5
ULAS J144902.02+114711.4	14:49:02.02	+11:47:11.40	–	18.35 ± 0.04	17.36 ± 0.02	17.73 ± 0.07	18.1 ± 0.15	-0.48 ± 0.13	T4.6	T4.0	T5.1	T5.5
ULAS J151637.89+011050.1	15:16:37.89	+01:10:50.10	–	19.48 ± 0.12	18.41 ± 0.05^{W}	18.67 ± 0.06^{W}	18.49 ± 0.2	-0.96 ± 0.20	T6.3	T5.7	T6.7	T6.5
WISE J151721.13+052929.3[c]	15:17:21.12	+05:29:29.03	–	19.57 ± 0.07	18.54 ± 0.05	18.85 ± 0.15	–	–	N/A	N/A	N/A	T8p
ULAS J153406.06+055643.9	15:34:06.06	+05:56:43.90	22.52 ± 0.15^{D}	20.24 ± 0.19	19.02 ± 0.1	–	–	-0.56 ± 0.13	T4.9	T4.4	T5.3	T5
ULAS J153653.80+015540.6	15:36:53.80	+01:55:40.60	–	19.15 ± 0.08	17.93 ± 0.05	18.03 ± 0.1	18.01 ± 0.16	–	N/A	N/A	N/A	T5
ULAS J154914.45+262145.6	15:49:14.45	+26:21:45.60	–	19.15 ± 0.07	18.05 ± 0.03^{W}	18.29 ± 0.03^{W}	–	-0.60 ± 0.12	T5.1	T4.6	T5.5	T5
ULAS J160143.75+264623.4	16:01:43.75	+26:46:23.40	21.35 ± 0.05^{D}	19.48 ± 0.08^{W}	18.43 ± 0.05^{W}	18.82 ± 0.07^{W}	18.75 ± 0.08^{W}	–	N/A	N/A	N/A	T6.5
ULAS J161436.96+244230.1	16:14:36.96	+24:42:30.10	22.36 ± 0.35^{D}	19.42 ± 0.08	18.52 ± 0.04	–	–	-1.01 ± 0.15	T6.4	T6.0	T6.7	T7
ULAS J161710.39+235031.4	16:17:10.39	+23:50:31.40	–	18.99 ± 0.05	17.72 ± 0.02	18.16 ± 0.08	–	-0.70 ± 0.09	T5.4	T5.1	T5.7	T6
ULAS J161934.78+235829.3	16:19:34.78	+23:58:29.30	–	19.72 ± 0.11	18.62 ± 0.06^{W}	18.91 ± 0.06^{W}	–	-0.75 ± 0.11	T5.6	T5.3	T5.9	T6
ULAS J161938.12+300756.4	16:19:38.12	+30:07:56.40	–	19.84 ± 0.11	18.61 ± 0.07^{W}	18.79 ± 0.06^{W}	–	-0.43 ± 0.09	T4.3	T3.9	T4.7	T5
ULAS J162655.04+252446.8	16:26:55.04	+25:24:46.80	–	19.82 ± 0.11	18.4 ± 0.04^{W}	18.62 ± 0.04^{W}	–	–	N/A	N/A	N/A	T5
ULAS J163931.52+323212.7	16:39:31.52	+32:32:12.70	20.30 ± 0.11	18.14 ± 0.02	16.71 ± 0.01	16.72 ± 0.03	16.8 ± 0.06	–	N/A	N/A	N/A	T3
ULAS J211616.26-010124.3	21:16:16.26	−01:01:24.30	$>22.10^{D}$	19.53 ± 0.12	18.27 ± 0.07	–	–	-1.10 ± 0.31	T6.6	T5.8	T7.2	T6
ULAS J223728.91+064220.1	22:37:28.91	+06:42:20.10	–	19.79 ± 0.08^{W}	18.78 ± 0.05^{W}	19.23 ± 0.04^{W}	19.94 ± 0.18^{W}	–	N/A	N/A	N/A	T6.5p
ULAS J230049.08+070338.0	23:00:49.08	+07:03:38.00	21.6 ± 0.12^{D}	18.97 ± 0.04^{W}	17.67 ± 0.02^{W}	17.77 ± 0.03^{W}	17.74 ± 0.05^{W}	-0.43 ± 0.08	T4.3	T3.9	T4.7	T4.5
ULAS J231536.93+034422.7	23:15:36.93	+03:44:22.70	–	19.89 ± 0.12	18.79 ± 0.08	–	–	< -0.77	N/A	N/A	N/A	T7
ULAS J231856.24+043328.5	23:18:56.24	+04:33:28.50	25.6 ± 0.32^{D}	20.18 ± 0.13	18.78 ± 0.07	–	–	< -0.95	N/A	N/A	N/A	T7.5
ULAS J232600.40+020139.2	23:26:00.40	+02:01:39.20	–	19.4 ± 0.08	17.98 ± 0.04	18.46 ± 0.12	18.41 ± 0.2	-1.64 ± 0.16	T7.7	T7.5	T7.9	T8
ULAS J232624.07+050931.6	23:26:24.07	+05:09:31.60	21.85 ± 0.21^{D}	19.75 ± 0.15	18.61 ± 0.1	18.61 ± 0.14	–	-0.51 ± 0.12	T4.7	T4.2	T5.1	N/A
ULAS J233104.12+042652.6	23:31:04.12	+04:26:52.60	22.12 ± 0.26^{D}	20.16 ± 0.14	18.67 ± 0.08	–	–	–	N/A	N/A	N/A	T4
ULAS J234228.97+085620.1	23:42:28.97	+08:56:20.10	20.15 ± 0.12	17.37 ± 0.01^{W}	16.39 ± 0.01^{W}	16.77 ± 0.01^{W}	17.1 ± 0.02^{W}	–	N/A	N/A	N/A	T6
ULAS J235204.62+124444.9	23:52:04.62	+12:44:44.90	–	19.64 ± 0.11	18.27 ± 0.05	18.55 ± 0.16	18.41 ± 0.21	-0.95 ± 0.12	T6.2	T5.9	T6.5	T6.5
ULAS J235715.98 +0:3:40.	23:57:15.98	+01:32:40.30	21.42 ± 0.22^{D}	19.78 ± 0.06^{W}	18.5 ± 0.04^{W}	18.68 ± 0.03^{W}	18.6 ± 0.05^{W}	–	N/A	N/A	N/A	T5.5p

[a]Albert et al. (2011); UKIDSS designation: ULAS J013302.48+023128.9.
[b]Kirkpatrick et al. (2011); UKIDSS designation: ULAS J092906.75+04:0957.7.
[c]Mace et al. (2013); UKIDSS designation: ULAS J151721.12+052929.0.
[d]On the spectral typing system of Burningham et al. (2008).

An estimate of the spectral type was obtained using the conversion defined by equation 2 from Tinney et al. (2005). The resulting methane colours for all targets with spectra presented here are given in Table 1, along with spectroscopically determined spectral types (see Section 4) and photometric spectral types. We also present CH_4 photometry for several DR8 targets which have $CH_4s - CH_4l < -0.5$, but which for various reasons were not followed up with spectroscopy. These targets are included as they form part of our UKIDSS DR8 space density estimate outlined in Section 9. A full summary of all the CH_4 photometry obtained, including earlier type objects and the extension of our analysis to include photometrically confirmed T dwarfs in DR9, along with a more detailed description of the CH_4 calibration can be found in Cardoso et al. (in preparation).

For a small number of targets, we obtained differential methane photometry using the Long-slit Infrared Imaging Spectrograph (LIRIS; Manchado et al. 1998) mounted on the WHT. These data were flat-field corrected, sky subtracted and mosaicked using LIRIS-DR.[4] In these cases, the methane colours are constructed as $H - [CH_4]l$, and calibrated assuming that the average $H - [CH_4]l$ of bright secondary calibrators in the field was zero (see also Kendall et al. 2007; Pinfield et al. 2008). Since no calibration for spectral type is yet determined for the $H - CH_4l$ colour, we do not present photometric estimates for the spectral types from these data.

4 SPECTROSCOPIC CONFIRMATION

Spectroscopic confirmation of most T dwarf candidates that survived the photometric follow-up programme was achieved using the Near InfraRed Imager and Spectrometer (NIRI; Hodapp et al. 2003) and the Gemini Near Infrared Spectrograph (GNIRS; Elias et al. 2006) on the Gemini North Telescope[5] and the InfraRed Camera and Spectrograph (IRCS; Kobayashi et al. 2000) on the Subaru telescope, both on Mauna Kea, Hawaii. In addition a smaller number of spectra were obtained using the Folded port InfraRed Echellette (FIRE) spectrograph (Simcoe et al. 2008, 2010) mounted on the Baade 6.5 m Magellan telescope at Las Campanas Observatory. We also obtained spectroscopy for a single target using XSHOOTER (Vernet et al. 2011) on UT2 of the VLT (Programme ID: 086.C-0450).

All observations were made up of a set of subexposures in an ABBA jitter pattern to facilitate effective background subtraction, with a slit width of 1 arcsec for NIRI, GNIRS and IRCS, whilst 0.6 arcsec was used for the FIRE observations. The length of the A–B jitter was 10 arcsec. For targets brighter than $J = 18.5$ total integrations were typically 4×300 s for NIRI, GNIRS and IRCS observations, whilst fainter targets were typically integrated for 8×300 s. FIRE integrations were 2×120 s for $J < 18.0$, 4×150 s for $18.0 < J < 18.5$, 6×150 s for $18.50 < J < 18.6$ and 8×150 s for our faintest targets. The programme numbers and dates of individual observations are summarized in Appendix C.

The NIRI and GNIRS observations were reduced using standard IRAF Gemini packages (Cooke & Rodgers 2005). The Subaru IRCS spectra were extracted using standard IRAF packages. The AB pairs were subtracted using generic IRAF tools, and median stacked. The NIRI, GNIRS and IRCS spectra were calibrated in a similar manner. Comparison argon arc frames were used to obtain dispersion solutions, which were then applied to the pixel coordinates in the dispersion direction on the images. The resulting wavelength-calibrated subtracted pairs had a low-level of residual sky emission removed by fitting and subtracting this emission with a set of polynomial functions fitted to each pixel row perpendicular to the dispersion direction, and considering pixel data on either side of the target spectrum only. The spectra were then extracted using a linear aperture, and cosmic rays and bad pixels removed using a sigma-clipping algorithm. Telluric correction was achieved by dividing each extracted target spectrum by that of an early A- or F-type standard star observed just before or after the target and at a similar airmass. Prior to division, hydrogen lines were removed from the standard star spectrum by interpolating the stellar continuum. Relative flux calibration was then achieved by multiplying through by a blackbody spectrum of the appropriate $T_{\rm eff}$. This $T_{\rm eff}$ was taken from Masana, Jordi & Ribas (2006) where available, or else was estimated from the spectral type of the telluric standard. Since the near-infrared region is well into the Rayleigh–Jeans tail of an A or F star's spectrum, very little systematic error is likely to be introduced from a crude estimate of this $T_{\rm eff}$.

The FIRE spectra were extracted using the low-dispersion version of the FIREHOSE pipeline, which is based on the MASE pipeline (Bochanski et al. 2009; Simcoe et al. 2010). The pipeline uses a flat-field constructed from two quartz lamp images taken with the lamp at high (2.5 V) and low (1.5 V) voltage settings. The data were divided by this pixel flat before being wavelength calibrated. The pipeline performs sky subtraction following the method outlined in Bochanski et al. (2011), adapted for the low-dispersion configuration of the spectrograph. The spectra were optimally extracted before being combined using a weighted mean, using an adaptation of the xcombspec routine from SPEXTOOL (Cushing, Vacca & Rayner 2004). The T dwarf spectra were then corrected for telluric absorption and flux calibrated using a FIRE-specific version of the xtellcor routine (Vacca, Cushing & Rayner 2003). Finally, residual outlying points due to cosmic rays and bad pixels were removed using a simple 3σ clipping algorithm.

The XSHOOTER data were reduced using the ESO pipeline (version 1.3.7). The pipeline removes non-linear pixels, subtracts the bias (in the VIS arm) or dark frames (in the NIR arm) and divides the raw frames by flat-fields. Images are pair-wise subtracted to remove sky background. The pipeline then extracts and merges the different orders in each arm, rectifying them using a multipinhole arc lamp (taken during the day-time calibration) and correcting for the flexure of the instrument using single-pinhole arc lamps (taken at night, one for each object observed). Telluric stars are reduced in the same way, except that sky subtraction is done by fitting the background (as tellurics are not observed in nodding mode). The spectra were telluric corrected and flux calibrated using IDL routines, following a standard procedure: first the telluric spectrum is cleared of H I absorption lines (by interpolating over them) and scaled to match the measured magnitudes; then is divided by a blackbody curve for the appropriate temperature (estimated from the telluric standard's spectral type), to obtain the instrument + atmosphere response curve; finally the target spectra are multiplied by the response curve obtained to flux calibrate it. The arms (VIS and NIR) were then merged by matching the flux level in the overlapping regions between them.

Complete details of the spectroscopic observations obtained for each of the T dwarfs presented here are given in Appendix C. The resulting spectra are shown in Fig. 3. This includes one T dwarf (ULAS J0929+0409) confirmed by Kirkpatrick et al. (2011), three

[4] http://www.iac.es/galeria/jap/lirisdr/LIRIS_DATA_REDUCTION.html

[5] under programmes GN-2009A-Q-16, GN-2009B-Q-62, GN-2009B-Q-99, GN-2010A-Q-44, GN-2010B-Q-41, GN-2011A-Q-73, GN-2011B-Q-5, GN-2011B-Q-43 and GN-2012A-Q-84

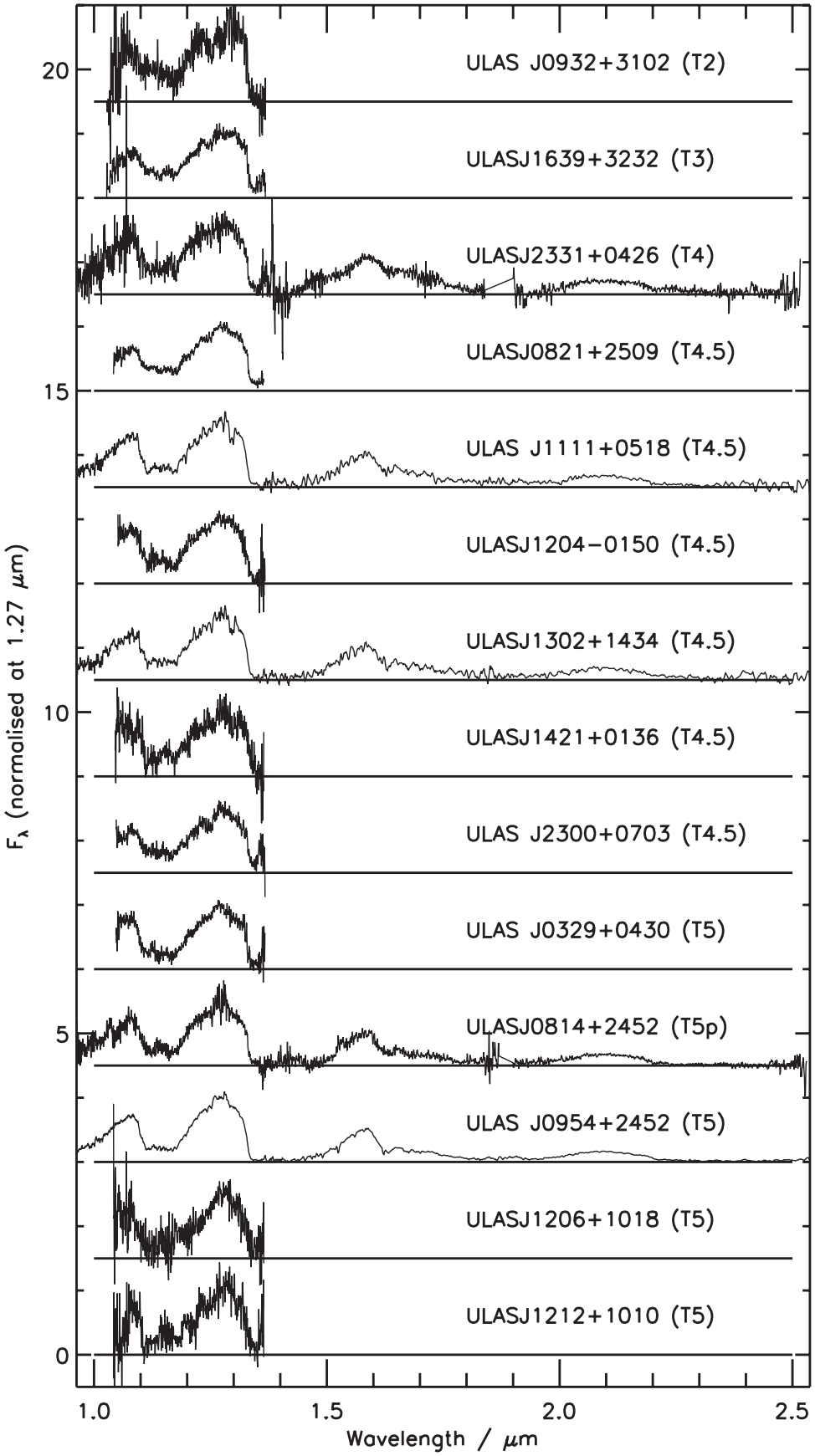

Figure 3. Spectra of the 76 T dwarfs presented here. Each spectrum is normalized at 1.27 ± 0.005 μm and offset for clarity. The GNIRS, NIRI and IRCS spectra have been rebinned by a factor of 3 as a compromise to maximize S/N and not sacrifice resolution.

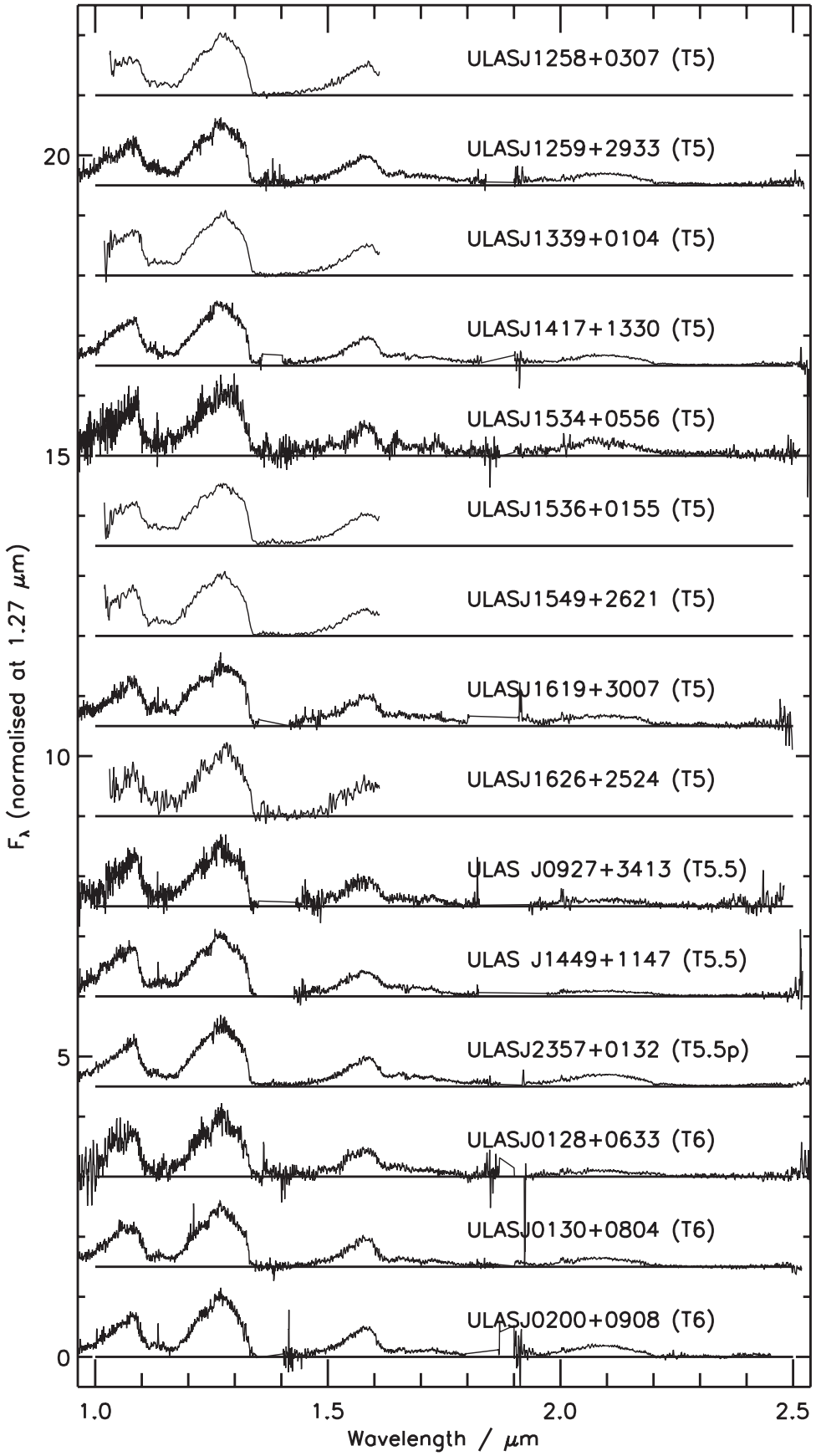

Figure 3 – *continued*

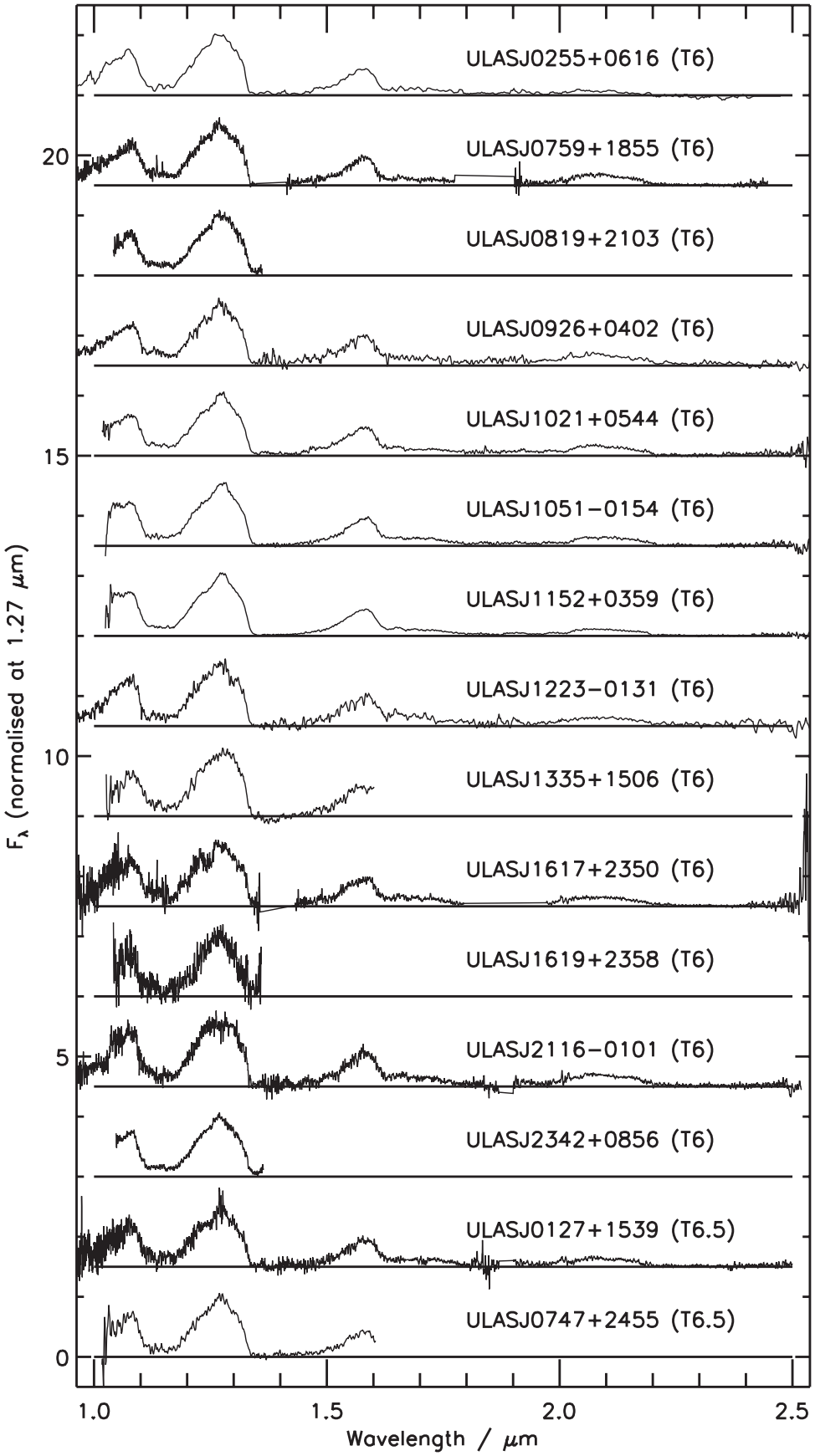

Figure 3 – *continued*

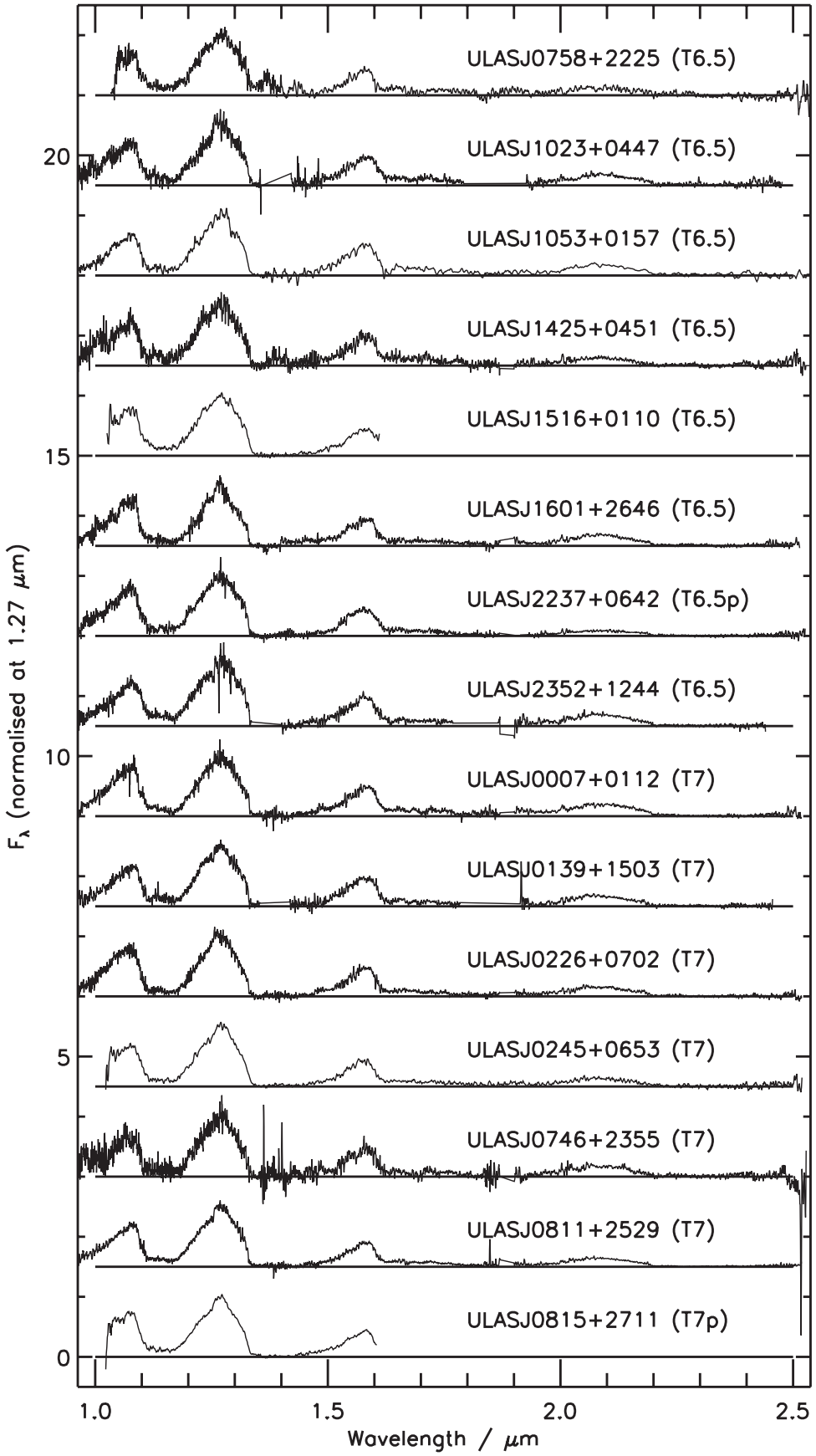

Figure 3 – *continued*

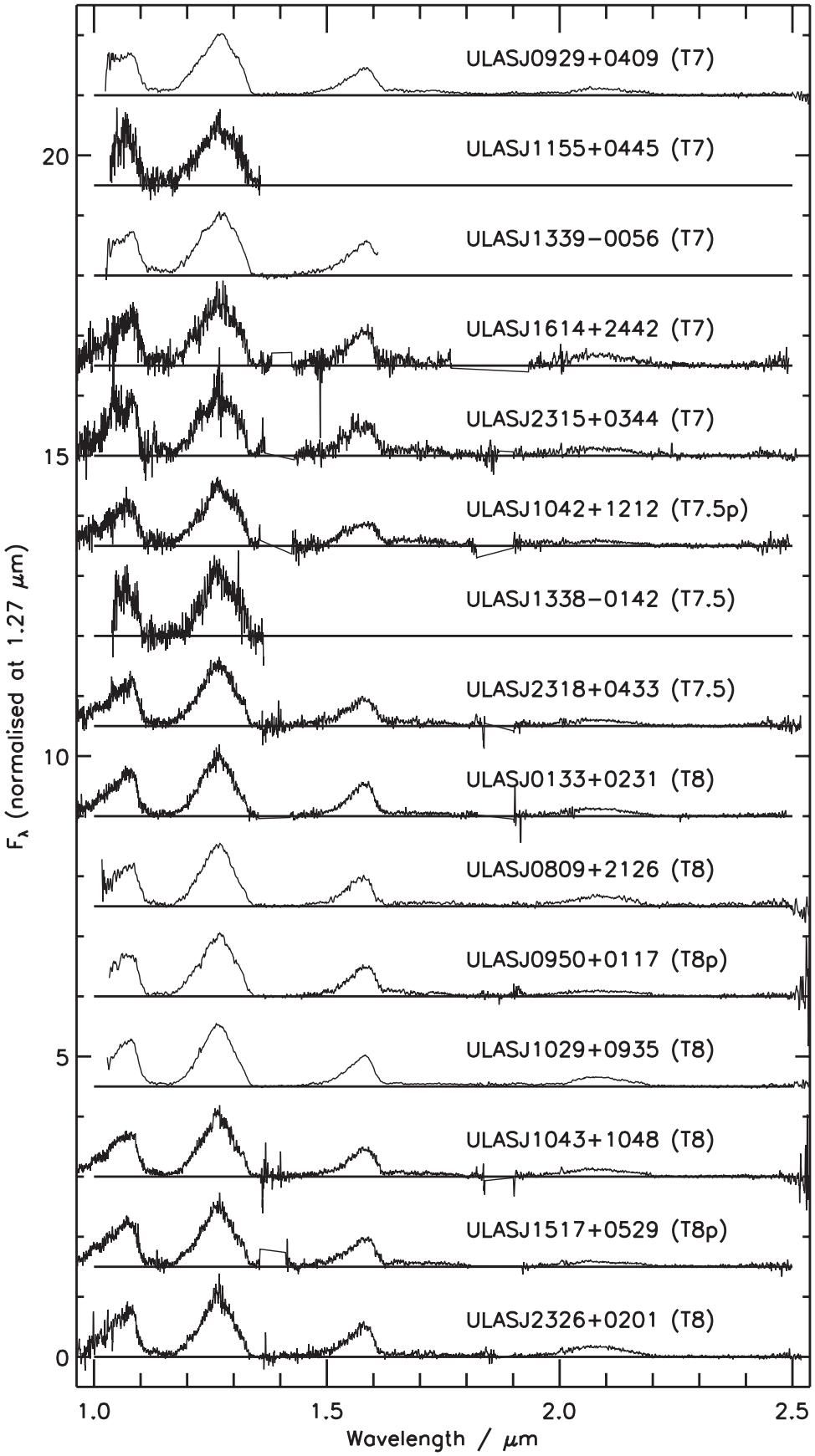

Figure 3 – *continued*

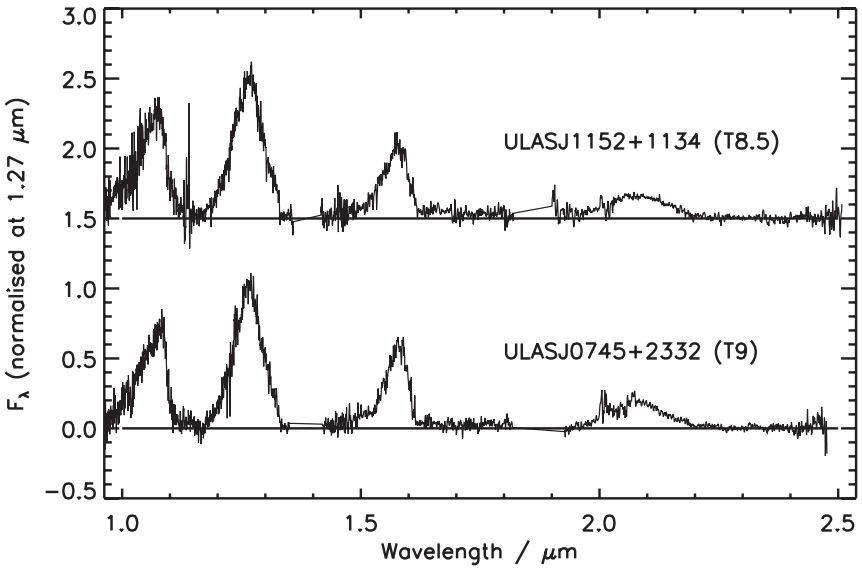

Figure 3 – *continued*

(ULAS J0954+0623, ULAS J1204-0150, ULAS J1152+0359) confirmed by Scholz et al. (2012) and one (ULAS J1517+0529) confirmed by Mace et al. (2013) since our spectroscopic follow-up, but prior to this publication.

4.1 Spectral types

We have assigned spectral types following the scheme of Burgasser et al. (2006) for types as late as T8, and the extension of Burningham et al. (2008) for types beyond T8. We have adopted this scheme in this work for two reasons. First, it provides continuity with our previous work (Burningham et al. 2008, 2009, 2010b), allowing a meaningful update to our previous space density estimate. Secondly, as was discussed in detail in Burningham et al. (2008), this scheme provides excellent continuity with the evolution of spectral index values from earlier types. This does not diminish the scheme's fundamentally empirical nature; it is anchored to template objects. However, it does seek to minimize the subjectivity as to the degree of spectral difference required for the distinction of two subtypes. We have only identified two new T8+ dwarfs in this paper, so this issue is of minor importance, and we have indicated the spectral types of these two objects on the Cushing et al. (2011) extension scheme in the notes column for completeness, and to avoid any future confusion. Objects that show substantial discrepancy either between the spectral types indicated by their spectral indices, or in comparison to their best-fitting spectral template have been classified as peculiar, and are denoted with the suffix 'p'. The most common feature leading to this designation is the suppression or enhancement of the *K*-band peak relative to the template. Table 2 summarizes our spectral type measurements and adopted classifications.

In Fig. 4, we have plotted our full UKIDSS LAS sample of 146 spectroscopically confirmed T dwarfs with *YJH* photometry (from a total of 171) on a *YJH* colour–colour diagram. Spectral types are distinguished by coloured symbols in whole subtype bins. Although there is significant scatter, a general trend from top right to lower left is apparent for the T4–T8 dwarfs, with the earliest type objects dominating the top right of the plot, whilst the later type objects dominate the lower left. This is consistent with the reduced *H*-band flux due to deepening CH_4 absorption, and a general trend to bluer $Y - J$ colours with decreasing $T_{\rm eff}$ that have previously been noted for the T spectral sequence (Burningham et al. 2010b; Leggett et al. 2010a; Liu et al. 2012).

5 SPACE-BASED MID-IR PHOTOMETRY

5.1 *WISE* cross-matched photometry

We cross-matched our full list of 171 spectroscopically confirmed T dwarfs within the UKIDSS LAS (which includes some objects that were confirmed in the literature rather than by our follow-up) against the *WISE* all-sky release catalogue, with matching radius of 6 arcsec. The typical epoch difference between the UKIDSS and *WISE* observations is less than 3 yr, so this ensured that high proper motion targets would still be matched. All apparent matches were visually inspected to remove spurious correlations. 67 T dwarfs were found with *WISE* photometry, of which 6 were affected by blending with another source. 25 of the 67 T dwarfs with *WISE* photometry are confirmed here for the first time, and their details are given in Table 3.

In Figs 5 and 6, we compare the numbers of T dwarfs detected by UKIDSS with those detected by both *WISE* and UKIDSS for objects brighter than $J = 18.3$ and for objects in the $J = 18.3$–18.8 range (the faintest 0.5 mag bin of our complete sample). It can be seen that UKIDSS is considerably more sensitive to earlier type objects than *WISE*, with roughly twice as many T4–T6.5 dwarfs identified in the $J < 18.3$ regime. In the fainter $18.3 < J < 18.8$ regime, this effect is even more pronounced, and extends to the T7–T7.5 bin. This highlights that although *WISE* now dominates the search for cool and faint T8+ dwarfs, wide and deep NIR surveys such as UKIDSS, and the (wider) VHS and (deeper) VIKING surveys continue represent an important resource for exploring the L and T dwarf sequences.

The faint nature of the large number of L and T dwarfs that will be revealed by VHS and VIKING, in particular, will be extremely challenging to confirm spectroscopically. To take advantage of the opportunity these offer for robust statistical studies of the substellar component of the Galaxy, it will be essential to develop methods for determining their properties from the photometric data that will be supplied by the surveys.

Table 2. Spectral typing ratios for the confirmed T dwarfs as set out by Burgasser et al. (2006) and Burningham et al. (2009), along with the types from by-eye comparison to template spectral standards and the final adopted types. The notes column indicates spectral types determined by authors where: A11 = Albert et al. (2011); K11 = Kirkpatrick et al. (2011); S10 = Scholz (2010); S12 = Scholz et al. (2012). In the case of T8+ objects, the notes column indicates the spectral type using the Cushing et al. (2011) system.

Name	Adopted	Templ.	H_2O-J	CH_4-J	W_J	H_2O-H	CH_4-H	CH_4-K	Note
ULAS J0007+0112	T7	T7	0.103 ± 0.008 (T7)	0.286 ± 0.007 (T6/7)	0.398 ± 0.015 (T6/7)	0.320 ± 0.018 (T5/6)	0.233 ± 0.007 (T7)	0.118 ± 0.010 (>T6)	
ULAS J0127+1539	T6.5	T6.5	0.179 ± 0.011 (T5/6)	0.307 ± 0.007 (T6)	0.451 ± 0.021 (<T7)	0.264 ± 0.016 (T6/7)	0.280 ± 0.011 (T6)	0.127 ± 0.012 (T6/7)	
ULAS J0128+0633	T6	T6	0.142 ± 0.009 (T6)	0.320 ± 0.008 (T6)	0.459 ± 0.009 (<T7)	0.298 ± 0.021 (T6)	0.392 ± 0.014 (T5)	0.172 ± 0.023 (T5/6)	
ULAS J0130+0804	T6	T6	0.170 ± 0.011 (T5/6)	0.338 ± 0.005 (T6)	0.497 ± 0.014 (<T7)	0.275 ± 0.010 (T6)	0.291 ± 0.009 (T6)	0.100 ± 0.012 (>T6)	T8.5 A11
CFBDS J0133+0231	T8	T8	0.051 ± 0.020 (T7/8)	0.191 ± 0.018 (>T7)	0.301 ± 0.009 (T8)	0.163 ± 0.011 (T8)	0.113 ± 0.006 (>T7)	0.030 ± 0.027 (>T6)	
ULAS J0139+1503	T7	T7	0.122 ± 0.015 (T6/7)	0.268 ± 0.014 (T6/7)	0.386 ± 0.008 (T7)	0.257 ± 0.030 (T6/7)	0.209 ± 0.010 (T7)	0.084 ± 0.019 (>T6)	
ULAS J0200+0908	T6	T6	0.146 ± 0.011 (T6)	0.285 ± 0.008 (T6/7)	0.453 ± 0.005 (<T7)	0.294 ± 0.008 (T6)	0.237 ± 0.008 (T7)	0.079 ± 0.013 (>T6)	
ULAS J0226+0702	T7	T7	0.082 ± 0.005 (T7)	0.230 ± 0.004 (T7)	0.374 ± 0.005 (T7)	0.273 ± 0.010 (T6)	0.219 ± 0.008 (T7)	0.108 ± 0.010 (>T6)	
ULAS J0245+0653	T7	T7	0.101 ± 0.004 (T7)	0.260 ± 0.003 (T7)	0.394 ± 0.003 (T7)	0.271 ± 0.009 (T6)	0.229 ± 0.008 (T7)	0.056 ± 0.025 (>T6)	
ULAS J0255+0616	T6	T6	0.154 ± 0.002 (T6)	0.282 ± 0.002 (T6/7)	0.481 ± 0.003 (<T7)	0.337 ± 0.003 (T5)	0.251 ± 0.002 (T6/7)	0.027 ± 0.012 (>T6)	
ULAS J0329+0430	T5	T5	0.238 ± 0.007 (T5)	0.452 ± 0.007 (T4/5)	0.540 ± 0.006 (<T7)	–	–	–	T7 (photometric) S10
ULAS J0745+2332	T9	T9	0.024 ± 0.010 (>T7)	0.130 ± 0.039 (>T7)	0.231 ± 0.012 (T9)	0.172 ± 0.022 (T8)	0.069 ± 0.012 (>T7)	0.102 ± 0.023 (>T6)	T8.5
ULAS J0746+2355	T7	T7	0.111 ± 0.012 (T7)	0.226 ± 0.009 (T7)	0.379 ± 0.011 (T7)	0.261 ± 0.023 (T6/7)	0.183 ± 0.016 (T7)	0.126 ± 0.017 (T6/7)	
ULAS J0747+2455	T6.5	T6.5	0.126 ± 0.008 (T6/7)	0.284 ± 0.005 (T6/7)	0.443 ± 0.005 (<T7)	0.295 ± 0.012 (T6)	0.058 ± 0.025 (>T7)	–	
ULAS J0758+2225	T6.5	T6.5	0.130 ± 0.005 (T6/7)	0.340 ± 0.006 (T6)	0.410 ± 0.004 (<T7)	0.236 ± 0.017 (T7)	0.273 ± 0.016 (T6)	0.260 ± 0.035 (T4/5)	
ULAS J0759+1855	T6	T6	0.191 ± 0.006 (T5)	0.324 ± 0.004 (T6)	0.467 ± 0.005 (<T7)	0.318 ± 0.012 (T5/6)	0.274 ± 0.008 (T6)	0.090 ± 0.008 (>T6)	
ULAS J0809+2126	T8	T8	0.026 ± 0.005 (>T7)	0.193 ± 0.003 (>T7)	0.304 ± 0.003 (T8)	0.202 ± 0.007 (T7/8)	0.097 ± 0.009 (>T7)	0.175 ± 0.022 (T5/6)	
ULAS J0811+2529	T7	T7	0.113 ± 0.003 (T7)	0.259 ± 0.002 (T7)	0.399 ± 0.002 (T6/7)	0.263 ± 0.004 (T6/7)	0.229 ± 0.003 (T7)	0.091 ± 0.004 (>T6)	
ULAS J0814+2452	T5p	T5	0.237 ± 0.007 (T5)	0.408 ± 0.007 (T5)	0.533 ± 0.008 (<T7)	0.189 ± 0.015 (T7/8)	0.464 ± 0.011 (T5)	0.152 ± 0.011 (T6)	
ULAS J0815+2711	T7p	T7	0.112 ± 0.004 (T7)	0.243 ± 0.002 (T7)	0.412 ± 0.002 (<T7)	0.327 ± 0.005 (T5)	0.050 ± 0.017 (>T7)	–	
ULAS J0819+2103	T6	T6	0.183 ± 0.004 (T5/6)	0.350 ± 0.004 (T6)	0.437 ± 0.003 (<T7)	–	–	–	T5.5 (photometric) S10
ULAS J0821+2509	T4.5	T4.5	0.326 ± 0.004 (T4)	0.508 ± 0.004 (T4)	0.574 ± 0.004 (<T7)	–	–	–	
ULAS J0926+0402	T6	T6	0.186 ± 0.008 (T5/6)	0.317 ± 0.007 (T6)	0.451 ± 0.009 (<T7)	0.392 ± 0.045 (T4/5)	0.309 ± 0.019 (T6)	0.266 ± 0.025 (T4)	
ULAS J0927+3413	T5.5	T5.5	0.200 ± 0.016 (T5)	0.347 ± 0.011 (T6)	0.509 ± 0.015 (<T7)	0.313 ± 0.032 (T5/6)	0.334 ± 0.022 (T6)	0.166 ± 0.044 (T6/7)	
WISEP J0929+0409	T7	T7	0.087 ± 0.003 (T7)	0.276 ± 0.002 (T7)	0.374 ± 0.002 (T7)	0.243 ± 0.004 (T7)	0.204 ± 0.004 (T7)	0.092 ± 0.014 (>T6)	T6.5 K11
ULAS J0932+3102	T2	T2	0.431 ± 0.023 (T2/3)	0.643 ± 0.027 (T2)	0.726 ± 0.023 (<T7)	–	–	–	
ULAS J0950+0117	T8p	T8p	0.043 ± 0.004 (>T7)	0.218 ± 0.003 (T7)	0.337 ± 0.003 (T8)	0.156 ± 0.005 (T8)	0.187 ± 0.003 (T7)	0.168 ± 0.014 (T5/6)	
ULAS J0954+0623	T5	T5	0.200 ± 0.003 (T5)	0.370 ± 0.003 (T5)	0.517 ± 0.003 (<T7)	0.314 ± 0.005 (T6)	0.407 ± 0.005 (T5)	0.209 ± 0.009 (T5)	T5.5 S12
ULAS J1021+0544	T6	T6	0.167 ± 0.004 (T6)	0.331 ± 0.002 (T6)	0.448 ± 0.003 (<T7)	0.346 ± 0.006 (T5)	0.292 ± 0.005 (T6)	0.113 ± 0.012 (>T6)	
ULAS J1023+0447	T6.5	T6.5	0.100 ± 0.012 (T7)	0.279 ± 0.010 (T6/7)	0.375 ± 0.010 (T7)	0.282 ± 0.021 (T6)	0.266 ± 0.014 (T6)	0.103 ± 0.015 (>T6)	
ULAS J1029+0935	T8	T8	0.049 ± 0.002 (>T7)	0.182 ± 0.001 (>T7)	0.303 ± 0.001 (T8)	0.191 ± 0.003 (T8)	0.117 ± 0.002 (>T7)	0.071 ± 0.010 (>T6)	
ULAS J1042+1212	T7.5p	T7.5p	0.064 ± 0.009 (T7/8)	0.286 ± 0.007 (T6/7)	0.333 ± 0.007 (T8)	0.144 ± 0.018 (T8/9)	0.263 ± 0.013 (T6)	0.279 ± 0.028 (T4)	
ULAS J1043+1048	T8	T8	0.047 ± 0.004 (>T7)	0.221 ± 0.003 (T7)	0.320 ± 0.004 (T8)	0.203 ± 0.009 (T7/8)	0.173 ± 0.006 (T7)	0.066 ± 0.009 (>T6)	
ULAS J1051−0154	T6	T6	0.146 ± 0.003 (T6)	0.354 ± 0.002 (T6)	0.436 ± 0.002 (<T7)	0.290 ± 0.005 (T6)	0.301 ± 0.004 (T6)	0.095 ± 0.013 (>T6)	
ULAS J1053+0157	T6.5	T6.5	0.092 ± 0.013 (T7)	0.245 ± 0.029 (T7)	0.390 ± 0.046 (T7/8)	0.295 ± 0.028 (T5/6)	0.267 ± 0.012 (T6)	0.130 ± 0.035 (T6/7)	
ULAS J1111+0518	T4.5	T4.5	0.292 ± 0.037 (T4/5)	0.408 ± 0.051 (T5/6)	0.569 ± 0.071 (<T7)	0.343 ± 0.033 (T5/6)	0.553 ± 0.018 (T4)	0.259 ± 0.068 (T4/5)	
ULAS J1152+0359	T6	T6	0.142 ± 0.002 (T6)	0.345 ± 0.001 (T6)	0.448 ± 0.001 (<T7)	0.295 ± 0.003 (T6)	0.287 ± 0.002 (T6)	0.158 ± 0.009 (T6)	T6 S12
ULAS J1152+1134	T8.5	T8.5	0.038 ± 0.006 (>T7)	0.147 ± 0.004 (>T7)	0.260 ± 0.005 (T9)	0.168 ± 0.011 (T8)	0.134 ± 0.008 (>T7)	0.052 ± 0.011 (>T6)	T8.5
ULAS J1155+0445	T7	T7	0.126 ± 0.016 (T6/7)	0.319 ± 0.017 (T6)	0.379 ± 0.013 (T7)	–	–	–	
ULAS J1204−0150	T4.5	T4.5	0.348 ± 0.008 (T4)	0.426 ± 0.008 (T5)	0.611 ± 0.006 (<T7)	–	–	–	T5.5 S12
ULAS J1206+1018	T5	T5	0.227 ± 0.019 (T5)	0.430 ± 0.020 (T5)	0.426 ± 0.015 (<T7)	–	–	–	
ULAS J1212+1010	T5	T5	0.333 ± 0.020 (T4/5)	0.455 ± 0.022 (T4/5)	0.460 ± 0.016 (<T7)	–	–	–	

Table 2 – *continued*

Name	Adopted	Templ.	H_2O-J	CH_4-J	W_J	H_2O-H	CH_4-H	CH_4-K	Note
ULAS J1223−0131	T6	T6	0.147 ± 0.019 (T6/7)	0.315 ± 0.037 (T6/7)	0.466 ± 0.055 (<T7)	0.312 ± 0.027 (T5/6)	0.434 ± 0.018 (T5)	0.293 ± 0.058 (T4/5)	
ULAS J1258+0307	T5	T5	0.187 ± 0.006 (T5)	0.383 ± 0.004 (T5)	0.462 ± 0.004 (<T7)	0.332 ± 0.008 (T5)	–	–	
ULAS J1259+2933	T5	T5	0.227 ± 0.005 (T5)	0.408 ± 0.004 (T5)	0.530 ± 0.004 (<T7)	0.382 ± 0.009 (T4)	0.415 ± 0.006 (T5)	0.193 ± 0.007 (T5)	
ULAS J1302+1434	T4.5	T4.5	0.276 ± 0.049 (T4/5)	0.432 ± 0.076 (T5/6)	0.561 ± 0.098 (<T7)	0.378 ± 0.028 (T4/5)	0.516 ± 0.018 (T4)	0.317 ± 0.054 (T3/4)	
ULAS J1335+1506	T6	T6	0.148 ± 0.010 (T6)	0.371 ± 0.007 (T5)	0.450 ± 0.007 (<T7)	0.289 ± 0.015 (T6)	–	–	
ULAS J1338−0142	T7.5	T7.5	0.010 ± 0.045 (>T7)	0.237 ± 0.045 (T7/8)	0.237 ± 0.033 (T9)	–	–	–	
ULAS J1339−0056	T7	T7	0.073 ± 0.004 (T7/8)	0.275 ± 0.003 (T7)	0.354 ± 0.003 (T7)	0.226 ± 0.006 (T7)	–	–	
ULAS J1339+0104	T5	T5	0.215 ± 0.004 (T5)	0.402 ± 0.003 (T5)	0.500 ± 0.004 (<T7)	0.288 ± 0.006 (T6)	–	–	
ULAS J1417+1330	T5	T5	0.204 ± 0.004 (T5)	0.381 ± 0.003 (T5)	0.491 ± 0.002 (<T7)	0.306 ± 0.003 (T6)	0.378 ± 0.002 (T5)	0.174 ± 0.002 (T6)	T5.5 (photometric) S10
ULAS J1421+0136	T4.5	T4.5	0.374 ± 0.015 (T3/4)	0.610 ± 0.018 (T2)	0.582 ± 0.014 (<T7)	–	–	–	
ULAS J1425+0451	T6.5	T6.5	0.122 ± 0.009 (T6/7)	0.284 ± 0.008 (T6/7)	0.424 ± 0.010 (<T7)	0.263 ± 0.016 (T6/7)	0.282 ± 0.012 (T6)	0.097 ± 0.021 (>T6)	
ULAS J1449+1147	T5.5	T5.5	0.235 ± 0.004 (T5)	0.378 ± 0.003 (T5)	0.522 ± 0.003 (<T7)	0.301 ± 0.009 (T6)	0.389 ± 0.005 (T5)	0.254 ± 0.010 (T4)	T7 (photometric) S10
ULAS J1516+0110	T6.5	T6.5	0.126 ± 0.007 (T6/7)	0.323 ± 0.004 (T6)	0.437 ± 0.005 (<T7)	0.301 ± 0.009 (T6)	–	–	
WISE J1517+0529	T8p	T8p	0.045 ± 0.004 (>T7)	0.220 ± 0.003 (T7)	0.331 ± 0.004 (T8)	0.224 ± 0.010 (T7)	0.168 ± 0.006 (T7)	0.201 ± 0.018 (T5)	T8 M13
ULAS J1534+0556	T5	T5	0.256 ± 0.016 (T5)	0.395 ± 0.015 (T5)	0.515 ± 0.016 (<T7)	0.351 ± 0.025 (T4/5)	0.442 ± 0.022 (T5)	0.237 ± 0.021 (T4/5)	
ULAS J1536+0155	T5	T5	0.298 ± 0.004 (T5)	0.475 ± 0.003 (T4)	0.570 ± 0.003 (<T7)	0.348 ± 0.004 (T5)	–	–	
ULAS J1549+2621	T5	T5	0.233 ± 0.005 (T5)	0.381 ± 0.004 (T5)	0.543 ± 0.004 (<T7)	0.318 ± 0.007 (T5/6)	–	–	
ULAS J1601+2646	T6.5	T6.5	0.084 ± 0.005 (T7)	0.224 ± 0.004 (T7)	0.310 ± 0.004 (T8)	0.278 ± 0.012 (T6)	0.205 ± 0.009 (T7)	0.080 ± 0.008 (>T6)	
ULAS J1614+2442	T7	T7	0.096 ± 0.012 (T7)	0.289 ± 0.010 (T6/7)	0.375 ± 0.011 (T7)	0.062 ± 0.030 (T9)	0.160 ± 0.014 (T7/8)	0.088 ± 0.023 (>T6)	
ULAS J1617+2350	T6	T6	0.181 ± 0.006 (T5/6)	0.383 ± 0.003 (T5)	0.522 ± 0.004 (<T7)	0.313 ± 0.010 (T5/6)	0.348 ± 0.006 (T6)	0.170 ± 0.007 (T6)	
ULAS J1619+2358	T6	T7	0.074 ± 0.017 (T7/8)	0.273 ± 0.018 (T6/7)	0.362 ± 0.012 (T7)	–	–	–	
ULAS J1619+3007	T5	T5	0.321 ± 0.007 (T4/5)	0.441 ± 0.005 (T5)	0.605 ± 0.006 (<T7)	0.389 ± 0.015 (T4)	0.402 ± 0.010 (T5)	0.199 ± 0.010 (T5)	
ULAS J1626+2524	T5	T5	0.243 ± 0.020 (T5)	0.468 ± 0.014 (T4)	0.472 ± 0.014 (<T7)	0.294 ± 0.023 (T6)	–	–	
ULAS J1639+3232	T3	T3	0.387 ± 0.005 (T3)	0.584 ± 0.007 (T2/3)	0.631 ± 0.005 (<T7)	–	–	–	
ULAS J2116−0101	T6	T6	0.175 ± 0.010 (T5/6)	0.377 ± 0.011 (T5)	0.511 ± 0.014 (<T7)	0.291 ± 0.014 (T6)	0.339 ± 0.010 (T6)	0.138 ± 0.013 (T6/7)	
ULAS J2237+0642	T6.5p	T6.5p	0.128 ± 0.006 (T6/7)	0.295 ± 0.005 (T6)	0.430 ± 0.007 (<T7)	0.190 ± 0.014 (T7/8)	0.241 ± 0.010 (T6/7)	0.139 ± 0.016 (T6/7)	
ULAS J2300+0703	T4.5	T4.5	0.316 ± 0.008 (T4/5)	0.504 ± 0.009 (T4)	0.583 ± 0.006 (<T7)	–	–	–	
ULAS J2315+0344	T7	T7	0.093 ± 0.017 (T7)	0.270 ± 0.023 (T6/7)	0.382 ± 0.018 (T6/7)	0.184 ± 0.024 (T7/8)	0.193 ± 0.016 (T7)	0.254 ± 0.046 (T4/5)	
ULAS J2318+0433	T7.5	T7.5	0.054 ± 0.007 (>T7)	0.248 ± 0.005 (T7)	0.343 ± 0.006 (T8)	0.257 ± 0.015 (T6/7)	0.182 ± 0.011 (T7)	0.077 ± 0.019 (>T6)	
ULAS J2326+0201	T8	T8	0.052 ± 0.006 (>T7)	0.169 ± 0.012 (>T7)	0.304 ± 0.006 (T8)	0.203 ± 0.011 (T7/8)	0.097 ± 0.006 (>T7)	0.046 ± 0.010 (>T6)	
ULAS J2331+0426	T4	T4	0.388 ± 0.013 (T3/4)	0.489 ± 0.010 (T4)	0.693 ± 0.013 (<T7)	0.466 ± 0.019 (T2/3)	0.654 ± 0.016 (T3)	0.429 ± 0.017 (T3)	
ULAS J2342+0856	T6	T6	0.156 ± 0.003 (T6)	0.340 ± 0.003 (T6)	0.437 ± 0.002 (<T7)	–	–	–	T7 (photometric) S10
ULAS J2352+1244	T6.5	T6.5	0.152 ± 0.008 (T6)	0.312 ± 0.006 (T6)	0.449 ± 0.009 (<T7)	0.276 ± 0.014 (T6)	0.206 ± 0.014 (T7)	0.091 ± 0.021 (>T6)	
ULAS J2357+0132	T5.5p	T5.5p	0.173 ± 0.003 (T6)	0.362 ± 0.004 (T5/6)	0.484 ± 0.005 (<T7)	0.313 ± 0.007 (T6)	0.420 ± 0.007 (T5)	0.186 ± 0.004 (T5)	

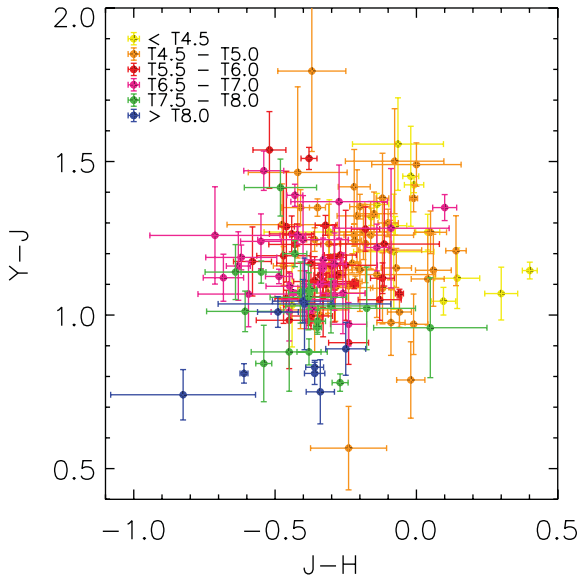

Figure 4. A $Y - J$ versus $J - H$ colour–colour diagram for 146 spectroscopically confirmed T dwarfs in the UKIDSS LAS with *YJH* photometry. Spectral types are indicated by coloured symbols.

5.2 Warm-*Spitzer* photometry

Warm-*Spitzer* IRAC photometry was obtained for some of the T dwarfs presented in this work via Cycles 6, 7 and 8 GO programmes 60093, 70058 and 80077 (PI Leggett). The observations were carried out in both the [3.6] and [4.5] bands (hereafter Ch1 and Ch2, respectively), with typically a 30 s frame time, repeated three to six times per pointing, and dither patterns consisting of 12 or 16 positions. In all cases the post-basic-calibrated-data mosaics generated by the Spitzer pipeline were used to obtain aperture photometry. Generally the sky levels were determined from annular regions. Aperture corrections were taken from the IRAC handbook.

Table 4 lists the targets observed, the associated programme ID, the date of the observation, the pipeline version used, the frame time, the total integration time, the aperture size, the derived photometry and uncertainties, and any notes on the data set. The table includes known sources not presented in this work, for which the IRAC data has not been previously published. We include it here so that it is available to the community.

6 WIDE COMMON PROPER MOTION BINARY SYSTEMS

6.1 Identifying companions

In Table 5, we present proper motions for the targets identified in this paper, along with those for late-T dwarfs found within the UKIDSS LAS sky in previous works. The vast majority of these proper motions have been drawn from the catalogue of Smith et al. (in preparation) which presents proper motions calculated from two epochs of *J*-band UKIDSS LAS observations. Here, we present only the absolute proper motions, and refer the reader to the Smith et al. catalogue for further astrometric parameters. A small number of additional proper motions have been calculated using an identical method to that used in Smith et al. (in preparation), but using our follow-up WFCAM *J*-band observations for the second epoch, instead of UKIDSS survey data.

We have cross-matched our full catalogue of T dwarfs identified within the UKIDSS LAS sky that have proper motions (128 targets) against several astrometric catalogues. We cross-matched our targets against the Hipparcos (Perryman et al. 1997; van Leeuwen 2007), LSPM-NORTH (Lépine & Shara 2005) and NOMAD (Zacharias et al. 2004) catalogues. We searched projected separations up to 200 00 au, assuming a minimum likely distance

Table 3. *WISE* photometry for 25 of the spectroscopically confirmed T dwarfs presented here for the first time.

Name	*W*1	*W*2	*W*3	*W*4	*WISE* blend?
CFBDS J0133+0231	17.78 ± 0.27	15.10 ± 0.09	>12.91	>9.26	N
ULAS J0139+1503	17.86 ± 0.26	15.94 ± 0.16	>12.93	>9.31	N
ULAS J0200+0908	16.16 ± 0.07	15.70 ± 0.14	>12.88	>9.24	Y
ULAS J0329+0430	17.52 ± 0.25	15.35 ± 0.14	>12.20	>8.53	N
ULAS J0745+2332	14.79 ± 0.04	14.47 ± 0.07	12.51 ± 0.50	>8.41	Y
ULAS J0758+2225	16.95 ± 0.16	15.23 ± 0.12	>12.65	>9.03	N
ULAS J0819+2103	17.16 ± 0.16	15.28 ± 0.10	>12.17	>8.81	N
ULAS J0821+2509	17.40 ± 0.22	15.48 ± 0.14	>12.67	>9.17	N
ULAS J0950+0117	18.05 ± 0.34	14.48 ± 0.06	>12.85	>9.20	N
ULAS J0954+0623	16.67 ± 0.13	14.66 ± 0.08	>12.64	>8.70	N
ULAS J1021+0544	16.63 ± 0.14	15.31 ± 0.28	>11.94	>8.14	N
ULAS J1029+0935	16.84 ± 0.13	14.29 ± 0.08	11.58 ± 0.33	>8.58	N
ULAS J1043+1048	>18.28	15.66 ± 0.18	12.10 ± 0.32	>9.07	N
ULAS J1152+0359	16.97 ± 0.15	15.34 ± 0.13	12.29 ± 0.38	>9.03	N
ULAS J1152+1134	16.89 ± 0.15	14.66 ± 0.08	12.37 ± 0.41	>8.57	N
ULAS J1204−0150	16.66 ± 0.11	14.70 ± 0.08	12.48 ± 0.42	>8.60	N
ULAS J1206+1018	17.55 ± 0.24	15.83 ± 0.19	>12.36	>8.86	N
ULAS J1338−0142	>18.22	16.12 ± 0.19	>13.01	>9.34	N
ULAS J1417+1330	16.67 ± 0.08	14.70 ± 0.06	12.51 ± 0.29	>9.49	N
ULAS J1449+1147	17.39 ± 0.16	14.84 ± 0.07	>12.40	>9.44	N
ULAS J1517+0529	>18.10	15.13 ± 0.08	>13.13	>9.52	N
ULAS J1549+2621	17.13 ± 0.10	16.09 ± 0.13	13.42 ± 0.5	>9.89	N
ULAS J1639+3232	16.62 ± 0.10	15.02 ± 0.08	12.28 ± 0.28	>9.05	N
ULAS J2326+0201	18.03 ± 0.42	15.45 ± 0.16	>12.53	>8.96	N
ULAS J2342+0856	16.07 ± 0.08	13.97 ± 0.05	12.63 ± 0.53	9.08 ± 0.54	N

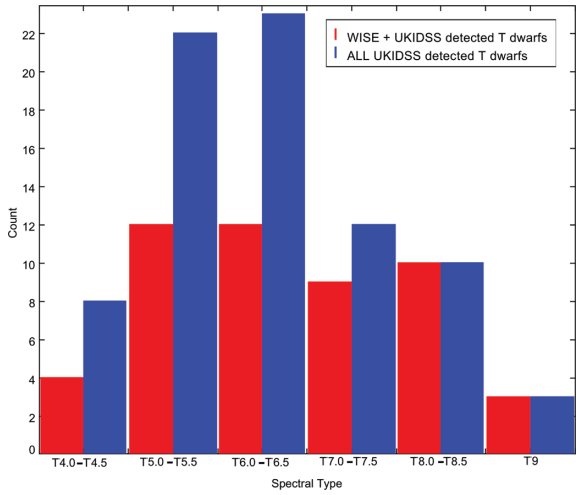

Figure 5. A histogram of UKIDSS and *WISE* + UKIDSS detected T dwarfs in our sample for objects with $J < 18.3$.

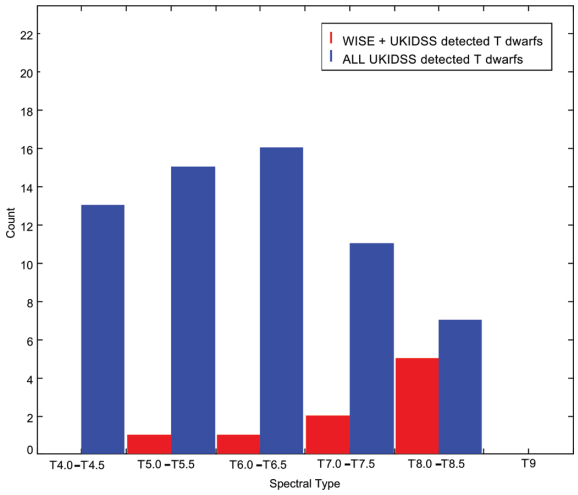

Figure 6. A histogram of UKIDSS and *WISE* + UKIDSS detected T dwarfs in our sample for objects with $18.3 < J < 18.8$.

for each source. Minimum and maximum likely distances for each source were determined by considering the ±0.5 subtype spectral type uncertainty, the mean M_J for each spectral subtype and the scatter about M_J as presented in Dupuy & Liu (2012). Since a significant fraction of wide-common proper motion companions are themselves multiple systems (e.g. Faherty et al. 2010), we also assigned an upper limit to the distance based on the target being an unresolved equal luminosity binary system. These distances are presented in Table 5.

To identify apparent pairs with common proper motion we selected only objects with total proper motions that are more than 3σ significant, and greater than 100 mas yr^{-1} (92 objects). To be considered common proper motion pairs we required 4σ matches in both $\mu_{\alpha\cos\delta}$ and μ_δ.

To assess if possible pairs share a common distance (in the absence of trigonometric parallax), we estimated the maximum and minimum plausible absolute magnitudes of the candidate primary stars based on the hypothesis that they lie at the same distance as their candidate companions. The candidate primary stars are compared to Hipparcos stars with *VJ* photometry in Fig. 7. Those targets whose maximum and minimum hypothesised M_J bracket the main sequence (or white dwarf or giant branches) were accepted as candidate common proper motion binary pairs to our T dwarfs. Of our nine candidate primaries with 4σ matched proper motions and *VJ* colours, five appear very likely to have common distance to our T dwarfs. One more has a minimum hypothetical M_J value that lies on the periphery of the main sequence and is thus consistent with the target sharing a common distance to the T dwarf, if the T dwarf is itself an unresolved binary. Three pairs are ruled out by the common distance test. The initial characterization of these pairs is given in Table 6.

It is worth highlighting that this method restricts us to investigating stars with *V*- and *J*-band photometry in the NOMAD and LSPM catalogues, and we have likely thus excluded a number of genuine binary companions. For example, we also recovered the white dwarf–T dwarf pair LSPM 1459+0851AB (Day-Jones et al. 2011) as a proper motion match; however, the lack of 2MASS photometry for the WD primary excluded it from our analysis at this stage. This was the only LSPM candidate with proper motion agreement that lacked *VJ* photometry. However, a large number of NOMAD candidate primaries with proper motion agreement lacked appropriate photometry for the common distance check. It is thus likely that a number of additional binary companions may remain unidentified in our sample, particularly for more distant red primaries that lack Tycho photometry (e.g. M dwarfs).

Of the five strong candidates, three are previously identified binary systems in our sample: Ross 458ABC (Goldman et al. 2010; Scholz 2010), BD+01 2930AB (Pinfield et al. 2012) and Hip 73786AB (LHS 3020AB Scholz 2010; Murray et al. 2011) and two are new candidates: ULAS J0950+0117 (T8) + LHS 6176 (estimated M4); ULAS J1339+0104 (T5) + HD 118865 (F8). The latter of these was also identified in our cross-match against Hipparcos, and the parallax for the primary is consistent with our estimated distance to the T dwarf secondary. The former has been independently identified as a candidate proper motion pair by Luhman et al. (2012) since our detailed study of it had already commenced.

To assess the probability of chance alignment for our new candidate binary pairs, we followed the method described in Dhital et al. (2010), which calculates the frequency of unrelated pairings using a Galactic model that is parametrized by empirically measured stellar number density (Jurić et al. 2008; Bochanski et al. 2010) and space velocity (Bochanski et al. 2007) distributions. All stars in the model are single (and hence unrelated); therefore any stars within the 5D ellipsoid defined by the binary's position, angular separation, distance and proper motions is a chance alignment. We performed 10^6 Monte Carlo realizations to calculate the probability of chance alignment. The chance-alignment probabilities for the three new candidates are given in the 'Notes' column of Table 6. The weaker candidate has a correspondingly higher probability of chance alignment, and in the absence of further data on the primary star, or improved distance estimates, it is not reasonable to pursue further analysis of this candidate system. The two strongest new candidates, however, are likely to be bona fide common proper motion systems and we proceed on this basis.

6.2 LHS 6176AB

6.2.1 Distance to LHS 6176AB

As part of our wider campaign for determining accurate distances to late-T dwarfs in our sample (e.g. Marocco et al. 2010; Smart et al. 2010), we have obtained a trigonometric parallax measurement for ULAS J0950+0117 (LHS 6176B), and also for the proposed primary LHS 6176. The astrometric observations and image reduction

Table 4. Spitzer photometry for a subset of T dwarfs, selected either as examples of late-T types, peculiar spectra or as benchmark objects. Full designations are given for those objects whose discoveries are reported in other publications, whilst abbreviated names are given for those objects whose discovery is presented in this work. Notes: A: The data were taken when *Spitzer* was cold, and longer wavelength photometry was also obtained: [5.8] = 14.24 ± 0.03, [8.0] = 13.31 ± 0.03. B: Separate, non-annular, skies used due to background structure.

Name	Spectral type	Programme number	Obs date (UT)	Pipeline version	Frame time (s)	Integration (min)	Aperture (arcsec)	[3.6] (mag)	[4.5] (mag)	Notes
CFBDS J005910.90−011401.3	T8.5[a]	50667	2009-01-26	S18.7.0	12	7.2	7.2	15.71 ± 0.01	13.66 ± 0.01	A
CFBDS J030135−161418	T7.5[b]	60093	2009-09-02	S18.12.0	30	48.0	7.2	16.95 ± 0.01	15.42 ± 0.01	
2MASS J07290002−3954043	T8[c]	60093	2009-12-04	S18.13.0	12	1.0	4.8	14.47 ± 0.01	12.95 ± 0.01	
ULAS J0809+2126	T8	70058	2011-05-31	S18.18.0	30	48.0	4.8	17.74 ± 0.05	16.03 ± 0.01	B
CFBDS J092250+152741		60093	2010-05-29	S18.18.0	30	48.0	7.2	17.45 ± 0.04	16.11 ± 0.01	
ULAS J0950+0117	T8p	60093	2010-01-06	S18.13.0	30	48.0	7.2	16.28 ± 0.01	14.35 ± 0.02	
ULAS J1043+1048	T8	70058	2012-02-01	S19.1.0	30	48.0	7.2	16.94 ± 0.01	15.34 ± 0.03	
ULAS J123327.45+121952.2	T3.5p[d]	80077	2012-09-03	S19.1.0	30	48.0	7.2	16.83 ± 0.01	15.61 ± 0.01	B
ULAS J1339+0104	T5	80077	2012-09-18	S19.1.0	30	48.0	7.2	16.93 ± 0.01	16.08 ± 0.02	
ULAS J2237+0642	T6.5p	80077	2012-09-08	S19.1.0	30	48.0	7.2	17.87 ± 0.01	15.48 ± 0.02	
ULAS J2326+0201	T8	80077	2012-01-31	S19.1.0	30	24.0	7.2	16.84 ± 0.03	15.37 ± 0.01	

[a]Cushing et al. (2011); [b]Albert et al. (2011); [c]Looper, Kirkpatrick & Burgasser (2007); [d]Burningham et al. (2010b).

procedures were identical to those described in Smart et al. (2010). Since the observing strategy was optimized for measuring the distance to the T dwarf, LHS 6176A was often close to saturation on the image and, as a result, the centroiding precision is reduced. For this reason, the original survey image from 2008 could not be used at all in the solution, so the final astrometric parameter precision for LHS 6176 is much lower than for the T dwarf. In total, 35 observations with 78 reference stars over a baseline of 4.22 yr were used for LHS 6176B, compared to 33 observations with 525 reference stars over 2.16 yr for LHS 6176A. The greater number of reference stars for LHS 6176A is due to their being drawn from the entire WFCAM chip, rather than from just the immediate vicinity of the target. All astrometric parameters indicate a common distance and common motion for the two objects, supporting our interpretation of the pair as a binary system. The proper motions are also consistent with those found for LHS 6176 in Lépine & Shara (2005) (249, −346 mas yr^{-1}). The resulting astrometric parameters for the pair are given in Table 7. When we re-run our chance alignment estimate calculation using the new trigonometric distance estimates, the probability of chance alignment is smaller than one part in 10^7. Assuming the more precise distance to LHS 6176B as the distance to the system, we find that the projected separation of the pair is thus 970 au.

6.2.2 *Spectroscopy of LHS 6176A*

Optical spectroscopy of LHS 6176A was obtained on the night of 2012 May 5 with the SuperNova Integral Field Spectrograph (SNIFS; Lantz et al. 2004) on the University of Hawaii 2.2 m telescope on Mauna Kea. SNIFS was operated with a dichroic mirror that separated the incoming light into blue (3200–5200 Å) and red (5100–9700 Å) spectrograph channels as well as an imaging channel that was used for guiding. The observations yielded a resolution of $R \approx 1000$ for the blue channel and $R \approx 1300$ for the red. Integration time was 210 s, which was sufficient for high S/N (≈80 per Å) in the red channel, which is our region of interest for spectral typing an object as red as LHS 6176A. Basic reduction was performed automatically by the SNIFS processing pipeline, which included dark, bias, flat-field corrections, and cleaning of bad pixels and cosmic rays. The clean data were then assembled into blue and red data cubes. Wavelengths were calibrated with arc lamp exposures taken at the same telescope pointing as the science data (to correct for flexures).

The calibrated spectrum was then sky-subtracted, and a 1D spectrum was extracted from the image cube using a point spread function model. Observations of the Feige 66, BD+75325 and G191B2B spectrophotometric standards (Oke 1990) taken over the course of the night were used to correct each spectrum for instrument response and remove telluric lines. Spectra were then shifted in wavelength to the rest frames of their source stars by cross correlating each spectrum with similar spectral type templates from the SDSS (Stoughton et al. 2002; Bochanski et al. 2007). More details on the SNIFS data processing pipeline can be found in Bacon et al. (2001) and Aldering et al. (2006), and more information on additional data processing can be found in Lepine et al. (2013).

Fig. 8 shows the extracted red channel. Overplotted is an M4 template spectrum based on mean spectra of inactive M dwarfs from Bochanski et al. (2007), their extremely close agreement across nearly the entire wavelength range covered by our data leads us to adopt a spectral type of M4V for LHS 6176. Their excellent agreement, and the lack of Hα in emission also suggests a lack of activity for this object. The absence of Hα in emission has been found to be typical of M4 dwarfs with ages of >3.5 Gyr (West et al. 2008).

We have also obtained NIR spectroscopy of LHS 6176A on 2012 April 30 UT at the NASA Infrared Telescope Facilty on the summit of Mauna Kea, Hawaii. We used the facility spectrograph SpeX (Vacca et al. 2003) in short-wavelength cross-dispersed mode with the 0.3 arcsec slit, which provided an average spectral resolution ($R \equiv \Delta\lambda/\lambda$) of ≈2000. We obtained six exposures, each with a 120 s integration time and dithered in an ABBA pattern, for a total of 12 min on-source. We observed the A0 V star HD 92245 contemporaneously for telluric calibration. All spectra were reduced using version 3.4 of the SPEXTOOL software package (Vacca et al. 2003; Cushing et al. 2004). The resulting *JHK* spectrum is shown in Fig. 9.

We have taken three approaches to estimating the metallicity of LHS 6176A

Method 1. Our parallax for LHS 6176 also allows us to estimate its metallicity using the improved [Fe/H] versus $M_{K_s}/V - K_s$ calibrations of Schlaufman & Laughlin (2010) and Neves et al. (2012). Since the uncertainty on the parallax of the T dwarf component is considerably smaller than that of LHS 6176A, we have adopted the former's distance for the system. To maximize the precision of our metallicity estimate we have obtained new *V*-band photometry of

Table 5. Proper motions for T dwarfs within UKIDSS LAS sky. Unless otherwise stated proper motions are drawn from the catalogue of Smith et al. (in preparation). Epoch baselines denoted with ^{W} indicate that the proper motion has been calculated from our own WFCAM follow-up following the same method as used for the Smith et al. catalogue. Spectral types are on the system of Burningham et al. (2008). Maximum and minimum plausible distances have been calculated using the mean magnitudes for each spectral subtype from Dupuy & Liu (2012) and assuming ±0.5 subtype precision on types. An additional maximum distance to account for possible unresolved binaries is given in the final column.

Name	α (J2000)	δ (J2000)	Spectral type	Ref.	$\mu_{\alpha\cos\delta}$ (mas yr^{-1})	μ_δ (mas yr^{-1})	Baseline (yr)	$D_{\rm min}$ (pc)	$D_{\rm max}$ (pc)	$D_{\rm max}$(binary) (pc)
ULAS J013017.79+080453.9	01:30:17.79	+08:04:53.90	T6		12.98 ± 24.45	− 43.98 ± 59.09	1.29^W	30.1	51.3	72.4
ULAS J020013.18+090835.2	02:00:13.18	+09:08:35.20	T6		7.16 ± 27.97	− 40.39 ± 28.01	1.28	28.4	48.4	68.4
ULAS J022603.18+070231.4	02:26:03.18	+07:02:31.40	T7		54.55 ± 16.02	59.24 ± 16.38	2.02^W	22.6	53.0	74.8
ULAS J024557.88+065359.4	02:45:57.88	+06:53:59.40	T7		− 101.13 ± 32.52	− 112.72 ± 29.84	1.05^W	21.0	49.2	69.5
SDSS J032553.17+042540.1	03:25:53.13	+04:25:40.10	T5.5	1	− 194.65 ± 15.04	− 102.68 ± 14.86	2.09^W	13.4	24.1	34.0
ULAS J032920.22+043024.5	03:29:20.22	+04:30:24.50	T5		225.25 ± 15.8	− 59.84 ± 15.51	2.09^W	31.5	53.2	75.2
SDSS J074149.14+235127.3	07:41:49.01	+23:51:25.90	T5	2	− 259.64 ± 11	− 216.24 ± 11.02	2.03	14.6	24.7	34.9
ULAS J074503.03+233240.3	07:45:03.03	+23:32:40.30	T9		− 251.7 ± 21.34	− 287.98 ± 21.1	2.03	8.7	19.4	27.4
ULAS J074617.17+235532.2	07:46:17.17	+23:55:32.20	T7		− 3.75 ± 24.51	− 120.29 ± 24.53	2.03	28.2	66.1	93.3
ULAS J074502.79+245516.3	07:45:02.79	+24:55:16.30	T6.5		− 84.88 ± 12.55	− 60.28 ± 12.52	2.03	31.6	45.1	63.7
WISEP J075003.84+272544.8	07:50:03.84	+27:25:44.80	T8.5	3	− 734.03 ± 14.2	− 195.27 ± 14.49	2.00	12.9	36.4	51.4
2MASS J07554795+2212169	07:55:47.95	+22:12:14.50	T5	4	− 4.2 ± 10.28	− 252.3 ± 10.65	2.91	12.1	20.4	28.9
ULAS J075829.83+222526.7	07:58:29.83	+22:25:26.70	T6.5		− 105.34 ± 10.37	− 57.49 ± 10.84	2.91	24.5	35.0	49.4
ULAS J075937.75+185555.0	07:59:37.75	+18:55:55.00	T6		− 48.17 ± 15.64	− 81.2 ± 15.91	2.9	42.9	73.1	103.3
ULAS J080918.41+212615.2	08:09:18.41	+21:26:15.20	T8		− 152.69 ± 15.28	− 154.7 ± 16.28	1.86	12.0	44.3	62.5
ULAS J081110.86+252931.8	08:11:10.86	+25:29:31.80	T7		45.25 ± 11.99	− 231.89 ± 12.05	1.97	14.6	34.2	48.3
ULAS J081407.51+245200.9	08:14:07.51	+24:52:00.90	T5p		− 51.29 ± 14.3	− 9.48 ± 14.11	2.03	49.7	83.9	118.6
ULAS J081507.26+271119.2	08:15:07.26	+27:11:19.20	T7p		− 50.15 ± 37.06	− 79.91 ± 36.98	0.90^W	20.5	48.1	67.9
ULAS J081918.58+210310.4	08:19:18.58	+21:03:10.40	T6		− 57.72 ± 11.49	− 181.4 ± 10.67	1.86	19.2	32.7	46.2
ULAS J081948.08+073323.3	08:19:48.08	+07:33:23.30	T6p	5	13.17 ± 9.41	− 68.5 ± 9.4	5.09	34.7	59.2	83.6
ULAS J082155.49+250939.6	08:21:55.49	+25:09:39.60	T4.5		− 449.31 ± 14.02	− 56.45 ± 10.26	2.03	31.3	45.9	64.9
ULAS J082327.46+002424.4	08:23:27.46	+00:24:24.40	T4.0	6	− 35.13 ± 10.06	− 221.22 ± 10.11	5.04	55.4	83.9	118.5
ULAS J082707.67−020408.2	08:27:07.67	−02:04:08.20	T5.5	7	23.21 ± 8.01	− 111.73 ± 7.97	6.07	22.7	40.8	57.6
SDSS J083048.81+012831.0	08:30:48.89	+01:28:28.90	T4.5	4	186.16 ± 9.08	− 361.52 ± 8.96	5.07	18.2	26.7	37.7
ULAS J083756.19−004156.0	08:37:56.19	−00:41:56.00	T3.0	6	− 13.13 ± 10.51	− 94.16 ± 10.53	6.06	48.8	78.0	110.2
ULAS J084036.72+075933.6	08:40:36.72	+07:59:33.60	T4.5	5	− 270.68 ± 12.98	− 82.66 ± 12.93	5.28	72.1	105.7	149.3
ULAS J084211.68+093611.9	08:42:11.68	+09:36:11.90	T5.5	5	− 201.73 ± 12.49	− 53.25 ± 12.62	5.20	39.8	71.4	100.9
ULAS J085139.03+005340.9	08:51:39.03	+00:53:40.90	T4.0	5	− 61.66 ± 11.07	− 39.68 ± 10.86	5.18	62.5	94.6	133.7
ULAS J085342.94+000651.8	08:53:42.94	+00:06:51.80	T6p	5	− 43.79 ± 9.51	120.23 ± 9.62	5.19	41.5	70.8	100
ULAS J090116.23−030635.0	09:01:16.23	−03:06:35.00	T7.5	7	− 56.37 ± 8.62	− 253.84 ± 10.39	6.18	16.1	31.3	44.2
ULAS J091309.55−003136.9	09:13:09.55	−00:31:36.90	T6		72.67 ± 11.54	− 51.54 ± 11.36	5.28	50.4	85.9	121.3
ULAS J092624.76+071140.7	09:26:24.76	+07:11:40.70	T3.5	5	− 51.48 ± 10.67	− 420.41 ± 12.3	5.12	34.5	47.7	67.4
WISEP J092906.77+040957.9	09:29:06.75	+04:09:57.70	T7	3	526.12 ± 32.38	− 438.45 ± 30.96	0.97^W	10.6	24.8	35.0
ULAS J092926.44+110547.3	09:29:26.44	+11:05:47.30	T2	5	− 41.48 ± 11.88	9.95 ± 11.8	5.12	63.1	100.5	141.9
ULAS J093245.48+310206.4	09:32:45.48	+31:02:06.40	T2		− 44.82 ± 14.75	− 6.29 ± 14.51	2.02	53.7	85.6	120.9
ULAS J093829.28−001112.6	09:38:29.28	−00:11:12.60	T4.5	6	− 255.55 ± 12.59	− 81.28 ± 11.48	5.32	57.3	83.9	118.6
ULAS J093951.0400:6:3.60	09:39:51.04	+00:16:53.60	T5.5	6	159.08 ± 11.15	− 299.34 ± 11.03	5.32	31.6	56.8	80.2
ULAS J094331.49+085849.2	09:43:31.49	+08:58:49.20	T5p	5	− 83.54 ± 11.48	− 78.78 ± 11.5	5.21	51.1	86.3	121.9
ULAS J094349.60+094203.4	09:43:49.60	+09:42:03.40	T4.5p	5	44.98 ± 13.17	− 123.92 ± 12.72	4.80	65.8	96.4	136.1
ULAS J094516.39+075545.6	09:45:16.39	+07:55:45.60	T5	5	− 129.17 ± 11.35	− 41.17 ± 10.61	5.33	30.6	51.8	73.1
ULAS J094806.06+064805.0	09:48:06.06	+06:48:05.00	T7	7	238.8 ± 12.16	− 273.6 ± 11.96	6.06	26.0	61.0	86.2
ULAS J095047.28+011734.3	09:50:47.28	+01:17:34.30	T8p		242.68 ± 11.79	− 386.56 ± 11.71	3.97	9.3	34.2	48.3

Table 5 – *continued*

Name	α (J2000)	δ (J2000)	Spectral type	Ref.	$\mu_{\alpha\cos\delta}$ (mas yr^{-1})	μ_{δ} (mas yr^{-1})	Baseline (yr)	$D_{\rm min}$ (pc)	$D_{\rm max}$ (pc)	$D_{\rm max}$(binary) (pc)
ULAS J095429.90+062309.6	09:54:29.90	+06:23:09.60	T5		−494.26 ± 9.92	−436.26 ± 10.79	2.75	20.3	34.4	48.5
ULAS J095829.86−003932.0	09:58:29.86	−00:39:32.00	T5.5	6	−59.18 ± 12.49	1.73 ± 12.33	6.24	51.8	92.9	131.2
CFBDS J100113+022622	10:01:13.04	+02:26:22.40	T5	8	−90.21 ± 13.7	49.41 ± 14.23	3.99	59.1	99.8	141.0
ULAS J100759.90−010031.1	10:07:59.90	−01:00:31.10	T5.5	7	−226.6 ± 11.08	145.69 ± 11.19	6.08	45.7	82.1	115.9
ULAS J101243.54+102101.7	10:12:43.54	+10:21:01.70	T5.5	5	−390.6 ± 11.94	−555 ± 15.99	4.74	19.9	35.6	50.4
ULAS J101721.40+011817.9	10:17:21.40	+01:18:17.90	T8p	9	−83 ± 12.46	−15.14 ± 11.74	5.05	11.7	43.3	61.1
ULAS J101821.78+072547.1	10:18:21.78	+07:25:47.10	T5	7	−168.38 ± 12.88	−14.81 ± 10.33	6.00	33.8	57.2	80.7
ULAS J102144.87+054446.1	10:21:44.87	+05:44:46.10	T6		−29.92 ± 36.78	30.79 ± 32.49	0.90^{W}	26.5	45.3	64.0
ULAS J102305.44+044739.2	10:23:05.44	+04:47:39.20	T6.5		15.49 ± 36.22	−83.08 ± 37.91	0.91^{W}	35.0	49.9	70.5
ULAS J102940.52+093514.6	10:29:40.52	+09:35:14.60	T8		−407.57 ± 37.19	−145.97 ± 26.38	0.91^{W}	6.6	24.3	34.4
ULAS J103434.52−001553.0	10:34:34.52	−00:15:53.00	T6.5p	5	−100.45 ± 14.95	−30.41 ± 14.54	4.01	43.5	61.9	87.5
ULAS J104355.37+104803.4	10:43:55.37	+10:48:03.40	T8		96.75 ± 37.4	−73.04 ± 37.95	0.91^{W}	10.2	37.7	53.2
ULAS J105134.32−015449.8	10:51:34.32	−01:54:49.80	T6		−65.76 ± 32.13	−40.03 ± 32.4	0.99^{W}	27.7	47.2	66.7
ULAS J105235.42+001632.7	10:52:35.42	+00:16:32.70	T5	5	−30.88 ± 18.54	−140.23 ± 18.4	2.39	56.8	95.9	135.5
SDSS J111010.01+011613.1	11:10:09.85	+01:16:10.50	T5.5	4	−235.42 ± 34.43	−273.03 ± 31.09	0.95^{W}	14.2	25.5	36.0
ULAS J114925.58−014343.2	11:49:25.58	−01:43:43.20	T5	5	−112.51 ± 13.11	11 ± 12.55	4.05	40.7	68.9	97.3
ULAS J115038.79+094942.9	11:50:38.79	+09:49:42.90	T6.5	6	−94.21 ± 13.94	−19.38 ± 14.08	5.59	40.0	57.0	80.5
ULAS J115338.74−014724.1	11:53:38.74	−01:47:24.10	T6	5	−568.28 ± 16.79	−333.86 ± 13.12	3.90	25.7	43.9	61.9
ULAS J115508.39+044502.3	11:55:08.39	+04:45:02.30	T7		483.25 ± 14.18	−533.47 ± 13.2	2.96	20.7	48.5	68.6
ULAS J115718.02−013923.9	11:57:18.02	−01:39:23.90	T5	5	108.24 ± 13.62	−20.85 ± 12.8	3.90	42.1	71.1	100.5
ULAS J115759.04+092200.7	11:57:59.04	+09:22:00.70	T2.5	6	−90.15 ± 11.89	30.25 ± 11.08	4.79	25.4	34.4	48.5
ULAS J120257.05+090158.8	12:02:57.05	+09:01:58.80	T5	5	−42.73 ± 12.09	−62.13 ± 10.63	4.79	21.4	36.1	51.1
ULAS J120444.67−015034.9	12:04:44.67	−01:50:34.90	T4.5		−402.6 ± 15.73	132.24 ± 11.38	3.64	25	36.6	51.8
ULAS J120621.03+101802.9	12:06:21.03	+10:18:02.90	T5		−400.83 ± 19.5	−87.42 ± 18.75	3.85	64.6	109.1	154.2
ULAS J120744.65+133902.7	12:07:44.65	+13:39:02.70	T6.0	5	−154.53 ± 12.49	0.84 ± 12.29	4.79	35.3	60.3	85.1
ULAS J121226.80+101007.4	12:12:26.80	+10:10:07.40	T5		−181.77 ± 16.23	−123.53 ± 16.5	3.86	53.2	89.9	127.1
ULAS J122343.35−013100.7	12:23:43.35	−01:31:00.70	T6		−168.28 ± 15.18	65.79 ± 14.32	3.64	42.8	73.0	103.1
ULAS J123153.60+091205.4	12:31:53.60	+09:12:05.40	T4.5p	5	82.62 ± 15.08	−80.16 ± 13.8	4.96	71.4	104.7	147.9
ULAS J123327.45+121952.2	12:33:27.45	+12:19:52.20	T4p	5	35.8 ± 10.74	92.94 ± 11.15	4.89	40.7	61.7	87.1
ULAS J123828.51+095351.3	12:38:28.51	+09:53:51.30	T8.5	9	−450.71 ± 15.46	41.72 ± 14.17	4.96	12.8	36.1	51.1
ULAS J123903.75+102518.6	12:39:03.75	+10:25:18.60	T0	5	−209.49 ± 13.53	92.23 ± 13.62	4.96	65.2	86.3	121.9
ULAS J124804.56+075904.0	12:48:04.56	+07:59:04.00	T7	5	−230.78 ± 12.95	−145.35 ± 11.95	5.03	15.6	36.6	51.7
ULAS J125708.07+110850.4	12:57:08.07	+11:08:50.40	T4.5	5	28.65 ± 14.42	−57.13 ± 13.94	4.81	53.5	78.3	110.7
ULAS J125835.97+030736.1	12:58:35.97	+03:07:36.10	T5		−170.86 ± 14.19	−30.75 ± 12.34	2.83	46.1	78.0	110.2
ULAS J130041.73+122114.7	13:00:41.73	+12:21:14.70	T8.5	10	−635.95 ± 14.43	−27.9 ± 12.29	3.83	5.1	14.3	20.2
ULAS J130217.21+130851.2	13:02:17.21	+13:08:51.20	T8.5	5	−427.96 ± 13.41	−9.34 ± 12.92	4.88	9.7	27.3	38.5
ULAS J130227.54+143428.0	13:02:27.54	+14:34:28.00	T4.5		−42.14 ± 16.29	−14.66 ± 15.2	3.71	58.9	86.3	121.9
ULAS J130303.54+001627.7	13:03:03.54	+00:16:27.70	T5.5	6	12.3 ± 20.99	−274.16 ± 19.97	2.64	53.5	95.9	135.5
ULAS J131508.42+082627.4	13:15:08.42	+08:26:27.40	T7.5	6	−36.52 ± 12.73	−103.85 ± 12.22	5.67	25.2	49.0	69.2
ULAS J131943.77+120900.2	13:19:43.77	+12:09:00.20	T5	5	−121.9 ± 16.04	−22.9 ± 14.59	4.87	58.6	99.1	140.0
ULAS J132048.12+102910.6	13:20:48.12	+10:29:10.60	T5	5	102.21 ± 11.03	−56.56 ± 11.44	4.94	35.6	60.3	85.1
ULAS J132605.18+120009.9	13:26:05.18	+12:00:09.90	T6p	5	70.63 ± 11.04	−29.76 ± 12.02	4.87	24.7	42.1	59.4
ULAS J133502.11+150653.5	13:35:02.11	+15:06:53.50	T6		3.02 ± 14.16	−106.03 ± 12.56	3.85	30.6	52.2	73.8
ULAS J133553.45+113005.2	13:35:53.45	+11:30:05.20	T9	9	−183.38 ± 13.1	−214.17 ± 10.92	4.86	5.5	12.1	17.1
ULAS J133828.69−014245.4	13:38:28.69	−01:42:45.40	T7.5		200.75 ± 21.02	−109.89 ± 20.2	2.56	23.3	45.3	64.0

Table 5 – *continued*

Name	α (J2000)	δ (J2000)	Spectral type	Ref.	$\mu_{\alpha\cos\delta}$ (mas yr^{-1})	μ_{δ} (mas yr^{-1})	Baseline (yr)	$D_{\rm min}$ (pc)	$D_{\rm max}$ (pc)	$D_{\rm max}$(binary) (pc)
ULAS J133933.64−005621.1	13:39:33.64	−00:56:21.10	T7		72.34 ± 17.15	− 14.95 ± 15.8	2.53	19.9	46.6	65.8
ULAS J133943.79+010436.4	13:39:43.79	+01:04:36.40	T5		− 130.23 ± 14.58	− 23.76 ± 14.72	2.72	40.1	67.9	95.9
SDSS J134646.43−003150.3	13:46:46.10	−00:31:51.40	T6.5	11	− 512.71 ± 12.41	− 112.02 ± 12.16	3.02	9.9	14.1	19.9
ULAS J134940.81+091833.3	13:49:40.81	+09:18:33.30	T7	5	− 154.6 ± 13.16	− 73.34 ± 12.13	5.05	30.3	71.1	100.5
ULAS J135607.41+085345.2	13:56:07.41	+08:53:45.20	T5	5	− 67.84 ± 12.12	− 2.95 ± 11.24	5.05	39.4	66.7	94.2
ULAS J141623.94+134836.3	14:16:23.94	+13:48:36.30	T7.5p	12	86.22 ± 12.43	128.58 ± 12.53	3.75	12.6	24.4	34.5
ULAS J141756.2213:0:5.80	14:17:56.22	+13:30:45.80	T5		− 123.05 ± 12.48	45.93 ± 10.32	4.88	22	37.2	52.5
ULAS J142145.63+013619.0	14:21:45.63	+01:36:19.00	T4.5		− 213.24 ± 17.99	57.23 ± 17.19	3.84	56.8	83.2	117.5
ULAS J142320.79+011638.2	14:23:20.79	+01:16:38.20	T8p		281.48 ± 19.56	− 492.01 ± 17.36	3.84	13.1	48.1	67.9
ULAS J142536.35+045132.3	14:25:36.35	+04:51:32.30	T6.5		137.3 ± 15.42	− 44.87 ± 14.93	3.84	40.4	57.5	81.3
ULAS J144458.87+105531.1	14:44:58.87	+10:55:31.10	T5	5	− 185.13 ± 12.32	− 137.62 ± 11.88	4.98	56.5	95.5	134.9
ULAS J144555.24+125735.1	14:45:55.24	+12:57:35.10	T6.5	5	− 369.47 ± 15.11	108.78 ± 14.93	4.92	37.8	54.0	76.2
ULAS J144901.91+114711.4	14:49:01.91	+11:47:11.40	T5.5		− 248.94 ± 10.8	− 252.19 ± 11.94	4.96	24.8	44.6	63.0
ULAS J145243.59+065542.9	14:52:43.59	+06:55:42.90	T4.5	13	57.71 ± 13.11	− 154.94 ± 12.25	6.79	59.7	87.4	123.5
ULAS J145935.25+085751.2	14:59:35.25	+08:57:51.20	T4.5	5	− 174.75 ± 12.06	− 78.04 ± 10.63	5.05	44.3	64.9	91.6
ULAS J150135.33+082215.2	15:01:35.33	+08:22:15.20	T4.5	6	93.61 ± 13.5	− 190.91 ± 13.57	5.70	51.8	75.9	107.2
SDSS J150411.63+102718.4	15:04:11.73	+10:27:16.90	T7	1	379.37 ± 10.5	− 382.55 ± 10.84	5.01	8.9	20.9	29.6
ULAS J150457.66+053800.8	15:04:57.66	+05:38:00.80	T6p	14	− 609.61 ± 12.68	− 514.86 ± 11.82	4.02	16.2	27.7	39.1
ULAS J150547.89+070316.6	15:05:47.89	+07:03:16.60	T4	6	37.29 ± 13.24	− 115.07 ± 12.79	5.79	67.3	101.9	143.9
ULAS J151637.89+011050.1	15:16:37.89	+01:10:50.10	T6.5		− 110.69 ± 16.45	− 80.97 ± 15.7	2.96	35.3	50.4	71.1
WISE J151721.13+052929.3	15:17:21.12	+05:29:29.03	T8p		− 78.89 ± 15.18	221.33 ± 14.49	3.18	11.8	43.5	61.5
ULAS J152526.25+095814.3	15:25:26.25	+09:58:14.30	T6.5	5	− 83.02 ± 12.05	128.17 ± 12.14	5.01	37.5	53.5	75.5
CFBDS J152655.78+034534.8	15:26:55.78	+03:45:34.80	T4	8	− 85.78 ± 12.84	− 7.49 ± 11.88	3.96	43.4	65.7	92.8
ULAS J152912.23+092228.5	15:29:12.23	+09:22:28.50	T6	5	− 125.96 ± 11.49	41.27 ± 11.43	5.03	41.1	70.1	99.1
ULAS J153406.06+055643.9	15:34:06.06	+05:56:43.90	T5		− 14.9 ± 12.06	− 107.46 ± 11.32	6.68	61.9	104.7	147.9
ULAS J153653.8001:5:0.60	15:36:53.80	+01:55:40.60	T5		− 205.16 ± 12.8	47.85 ± 14	2.97	37.6	63.5	89.7
ULAS J154427.34+081926.6	15:44:27.34	+08:19:26.60	T3.5	6	− 57.78 ± 11.17	0.08 ± 11.71	5.79	56	77.3	109.1
ULAS J154701.84+005320.3	15:47:01.84	+00:53:20.30	T5.5	6	− 76.28 ± 10.79	6.92 ± 10.37	5.68	38.7	69.5	98.2
ULAS J154914.45+262145.6	15:49:14.45	+26:21:45.60	T5		− 151.56 ± 12.61	208.94 ± 13.13	3.00	39.6	67	94.6
ULAS J160143.75+264623.4	16:01:43.75	+26:46:23.40	T6.5		− 41.6 ± 17	− 42.18 ± 17.11	2.99	35.6	50.8	71.8
ULAS J161436.96+244230.1	16:14:36.96	+24:42:30.10	T7		− 122.92 ± 11.46	32.01 ± 11.64	3.99	22.6	53.0	74.8
ULAS J161710.39+235031.4	16:17:10.39	+23:50:31.40	T6		− 146.63 ± 10.05	48.19 ± 9.97	3.99	27.3	46.6	65.8
ULAS J161934.78+235829.3	16:19:34.78	+23:58:29.30	T6		− 84.43 ± 12.4	11.54 ± 13.15	3.99	41.3	70.5	99.5
ULAS J161938.12+300756.4	16:19:38.12	+30:07:56.40	T5		− 5.54 ± 14.78	− 237.43 ± 15.47	3.03	51.3	86.7	122.5
ULAS J162655.04+252446.8	16:26:55.04	+25:24:46.80	T5		− 30.06 ± 13.66	− 44.36 ± 14.39	3.99	46.6	78.7	111.2
ULAS J163931.52+323212.7	16:39:31.52	+32:32:12.70	T3		129.07 ± 9.63	− 119.83 ± 10.96	3.06	21.2	34	48.0
ULAS J223728.91+064220.1	22:37:28.91	+06:42:20.10	T6.5p		347.86 ± 16.86	252.29 ± 15.73	2.14^{W}	41.9	59.7	84.3
ULAS J230049.08+070338.0	23:00:49.08	+07:03:38.00	T4.5		128.88 ± 41.56	− 152.06 ± 29.72	0.78^{W}	38.4	56.2	79.4
ULAS J234228.97+085620.1	23:42:28.97	+08:56:20.10	T6		242.18 ± 13.57	− 62.65 ± 21.61	2.17^{W}	14.8	25.2	35.6
ULAS J235715.98+013240.3	23:57:15.98	+01:32:40.30	T5.5p		47.32 ± 21.43	1.3 ± 25.73	1.28^{W}	42.1	75.5	106.7

1: Chiu et al. (2006); 2: Knapp et al. (2004); 3: Kirkpatrick et al. (2011); 4: Burgasser et al. (2006); 5: Burningham et al. (2010b); 6: Pinfield et al. (2008); 7: Lodieu et al. (2007b); 8: Albert et al. (2011); 9: Burningham et al. (2008); 10: Burningham et al. (2011); 11: Tsvetanov et al. (2000); 12: Burningham et al. (2010a); 13: Kendall et al. (2007); 14: Murray et al. (2011).

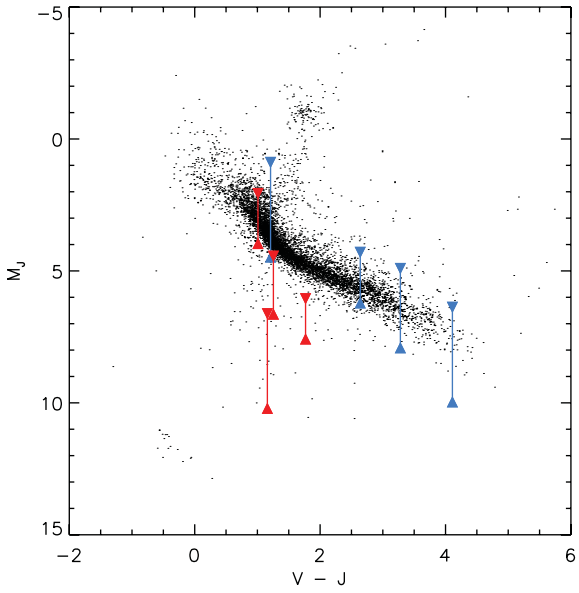

Figure 7. A $V - J$ versus M_J colour magnitude diagram showing the Hipparcos stars with V and J photometry (black dots) and our candidate primary stars. Blue symbols indicate the hypothetical range of M_J for primaries selected from LSPM, whilst the red symbols indicate the same for candidate primaries selected from NOMAD. One candidate primary lies beyond the plotted range.

LHS 6176A. Johnson V-band data were obtained using the 50 cm pt5m telescope on La Palma on the night of 2012 December 17. 56 s exposures were obtained. These exposures had the dark current and bias levels subtracted and were flat fielded using twilight sky frames. Objects were detected and instrumental magnitudes calculated using SEXTRACTOR (Bertin & Arnouts 1996). The instrumental magnitudes were calibrated against V-band magnitudes from the AAVSO Photometric All-Sky Survey[6]. The resulting transformation was $V = 0.9774 \times I + 0.1010$, where V is the calibrated Johnson V-band magnitude and I is the instrumental magnitude. The photon noise in our measurement is 0.004 mag, but this is outweighed by approximately 0.03 mag of calibration error, which we instead quote as our uncertainty (see Table 7).

We thus estimate a moderately low metallicity of [Fe/H] $= -0.43 \pm 0.19$ for LHS 6176A from the Schlaufman & Laughlin (2010) calibration and [Fe/H] $= -0.36 \pm 0.17$ dex using the Neves et al. (2012) calibration. The quoted error reflects the dispersion about the metallicity relations which dominates over our photometric uncertainties.

Method 2. We have applied the method of Mann et al. (2013) to our SNIFS optical and our *JHK* SpeX NIR spectra. From the optical regions we estimate [Fe/H] $= -0.31 \pm 0.08$ dex, whilst the NIR regions yield an estimate of [Fe/H] $= -0.25 \pm 0.05$ dex. These are consistent with one another, and the optically based estimate is consistent with the photometric estimate based on the Neves et al. (2012) relations.

Method 3. Using the strengths of metal sensitive K-band features and the calibration described by Rojas-Ayala et al. (2012) provides an estimate of [Fe/H] $= -0.26 \pm 0.14$ dex. This is consistent with all the other estimates, and matches the other spectroscopic estimates particularly well.

[6] http://www.aavso.org/apass

Although estimating M dwarf metallicities is challenging, the good agreement of the different estimates that we have obtained for LHS 6176A highlights the excellent progress that has been made in this field in recent years. We adopt the mean of the estimates from Neves et al. (2012), Mann et al. (2013) and Rojas-Ayala et al. (2012), and assign a metallicity of [Fe/H] $= -0.3 \pm 0.1$ dex for LHS 6176A. Table 7 summarizes our determined properties for LHS 6176A.

6.2.3 *The properties of LHS 6176B*

We have used our derived properties for LHS 6176A to constrain the metallicity and age of LHS 6176B, and determine more precise properties than would otherwise have been possible. Since our warm-*Spitzer* photometry is more precise than the *WISE* survey photometry, we have used it in preference in our calculations. We followed the same method as that described in Burningham et al. (2011) and Pinfield et al. (2012).

Briefly, we have calculated the bolometric flux using our *YJHK* spectroscopy flux calibrated to our J-band photometry and warm-*Spitzer* photometry. We have filled the gaps in our wavelength coverage by scaling the latest BT Settl model spectra (Allard, Homeier & Freytag 2010) to match our Y-band spectrum for wavelengths blueward of our GNIRS spectrum, and to match our Ch1 and Ch2 photometry for wavelengths redward of it. To avoid biasing our derived flux by assumptions regarding the $T_{\rm eff}$ of the target, we initially calculated the flux using a wide range of models covering $T_{\rm eff} = 500$–1000 K, $\log g = 4.5$–5.5 and metallicity, [M/H] $= 0.0$ and -0.3. The resulting flux ruled out high- and low-$T_{\rm eff}$ extremes and lowest gravity cases. We thus recalculated the flux using $T_{\rm eff} = 600$–900 K models with $\log g = 5.0$–5.5.

To account for random uncertainties in our flux calibration, we calculated each flux estimate (for each model spectrum) as the mean of a set of 100 different scalings, each offset by a random value drawn from the uncertainty in the photometry. Our final flux estimate is the mean of the estimates made using the range of models and different scalings, and our error is taken as the standard deviation on this value. Thus, our uncertainty implicitly includes both random and (identified) systematic elements. We thus calculate the flux from LHS 6176B as $F_{\rm bol} = 2.13 \pm 0.15 \times 10^{-16}$ W m^{-2}, and its luminosity as $8.94 \pm 1.30 \times 10^{20}$ W or $\log(L_*/{\rm L}_\odot) = -5.63 \pm 0.07$. This is approximately 60 per cent higher than the luminosity of the similarly metal poor benchmark T8 dwarf BD+01 2920B which was calculated using the same method (Pinfield et al. 2012).

We can use the measured luminosity for LHS 6176B, in combination with the evolutionary models of Baraffe et al. (2003), to estimate its radius and mass, assuming our estimated age for LHS 6176A. The COND models assume solar metallicity, and the effect of low metallicity on the luminosity–radius relation of brown dwarfs is not well constrained by observations. However, theoretical correlations between metallicity and radius derived by Burrows, Heng & Nampaisarn (2011) suggest radii are reduced by less than 5 per cent for a -0.5 dex shift from solar metallicity for objects at the stellar/substellar boundary, with considerably smaller shifts at lower masses. The Saumon & Marley (2008) evolutionary sequences suggest that shifts in radius of less than 1 per cent can be expected as a result of decreasing metallicity by 0.3 dex.

The derived properties also depend strongly on the assumed multiplicity (or otherwise) of LHS 6176B. If we assume that LHS 6176B is a single object, with an age in excess of 3.5 Gyr (based on the lack of Hα emission seen in LHS 6176A), we

Table 6. Initial characterization of candidate wide binary pairs selected by our cross-matches against the LSPM, NOMAD and Hipparcos catalogues. The 'Notes column includes previous discovery references and chance alignment probabilities for new candidates that passed the common distance test.

T dwarf	Primary name	Separation (arcsec)	$\Delta\mu_{\alpha\cos\delta}$	$\Delta\mu_\delta$	$V-J$	Distance match?[a]	Notes
ULAS J0950+0117	LHS 6176	52	0.5σ	3.5σ	4.11	Y	0.0002 per cent
ULAS J1043+1048	NOMAD 1006−0190624	1021	3.9σ	0.7σ	1.2	N	
ULAS J1300+1221	Ross 458	105	0.3σ	0.2σ	3.28	Y	1
ULAS J1315+0826	NOMAD 0983−0263649	382	1.6σ	2.0σ	1.3	B	2 per cent
ULAS J1335+1130	LSPM J1334+1123	1625	1.0σ	2.5σ	3.11	N	
ULAS J1339+0104	HD 118865	148	2.3σ	1.6σ	1.0	Y	0.3 per cent
ULAS J1423+0116	BD+01 2920	153	2.9σ	0.8σ	1.21	Y	2
ULAS J1459+0857	LSPM J1459+0851	386	0.6σ	1.6σ	–	–	3
ULAS J1504+0538	HIP 73786	64	0.1σ	0.8σ	2.64	Y	4,5

[a]Y = good match; N = bad match; B = requires binarity.
(1) Goldman et al. (2010); (2) Pinfield et al. (2012); (3) Day-Jones et al. (2011); (4) Scholz (2010); (5) Murray et al. (2011).

Table 7. Properties of LHS 6176AB.

	LHS 6176A	LHS 6176B
RA (ep = 2011.2579 eq = 2000)	09:50:49.8	09:50:47.3
Dec. (ep = 2011.2579 eq = 2000)	+01:18:09.4	+01:17:33.0
$PM_{\alpha\cos\delta}$ (mas yr^{-1})	242.42 ± 19.0	237.18 ± 2.84
PM_δ (mas yr^{-1})	−351.46 ± 4.50	−360.03 ± 3.13
Spectral type	M4	T8p
V	13.88 ± 0.03	–
B_J	15.2[a]	–
J (2MASS)	9.80 ± 0.02[b]	–
$J-H$ (2MASS)	0.57 ± 0.04[b]	–
$H-K_s$ (2MASS)	0.28 ± 0.04[b]	–
$V-K_s$	4.93 ± 0.04	–
J (UKIDSS)	–	18.02 ± 0.03
$Y-J$ (UKIDSS)	–	0.88 ± 0.04
$J-H$ (UKIDSS)	–	−0.38 ± 0.04
$H-K$ (UKIDSS)	–	−0.45 ± 0.08
$W1$	8.77 ± 0.02	18.05 ± 0.34
$W2$	8.60 ± 0.02	14.48 ± 0.06
$W3$	8.50 ± 0.02	>12.85
$W4$	>7.98	>9.20
[3.6]	–	16.28 ± 0.01
[4.5]	–	14.35 ± 0.02
π	46.14 ± 10.7	53.40 ± 3.51
Distance	$21.7^{+6.5}_{-4.1}$ pc	$18.73^{1.32}_{-1.15}$
[Fe/H]	−0.30 ± 0.1	–
Hα EW	−0.29 ± 0.23 Å	–
Age	>3.5 Gyr[c]	–
$\log(L_*/L_\odot)$	–	−5.63 ± 0.07
Projected separation	52 arcsec, ∼970 au	

[a]Lépine & Shara (2005).
[b]From 2MASS All-Sky Point Source Catalog.
[c]Derived from activity lifetime information presented in West et al. (2008).

estimate its radius to be $0.078\,R_\odot < R < 0.094\,R_\odot$ mass to be $0.055\,M_\odot > M > 0.030\,M_\odot$, with a corresponding temperature of $850 > T_{\rm eff} > 710$ K and gravity $5.3 > \log g > 5.0$ (respectively). If, on the other hand, we assume that LHS 6176B is an equal luminosity binary system, we find that the components would have radius $0.081\,R_\odot < R < 0.096\,R_\odot$ and mass $0.045\,M_\odot > M > 0.022\,M_\odot$, and with a corresponding temperature of $700 > T_{\rm eff} > 590$ K and gravity $5.30 > \log g > 4.8$. Although LHS 6176B has a J-band magnitude ($M_J = 16.65$) at the faint end of the scatter about the T8 mean magnitude in Dupuy & Liu (2012, $M_J = 16.39 \pm 0.35$), we cannot rule out binarity. It should be borne in mind that the mean T8 M_J is calculated from a sample that specifically excludes peculiar objects, and so is dominated by objects with higher metallicity than LHS 6176B. A comparison with other low-metallicity objects would thus be more relevant. BD+01 2920B (Pinfield et al. 2012) provides just such a comparison. LHS 6176B is approximately 0.85 mag brighter than this object the J band. It is thus quite possible that LHS 6176B is an unresolved binary system, and we refrain from adopting a single set of properties for this object.

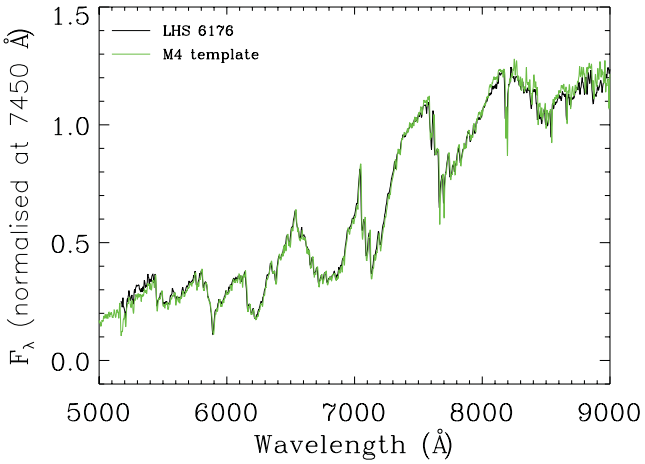

Figure 8. Our SNIFS spectrum of LHS 6176A compared with the non-active M4 template spectrum from Bochanski et al. (2007).

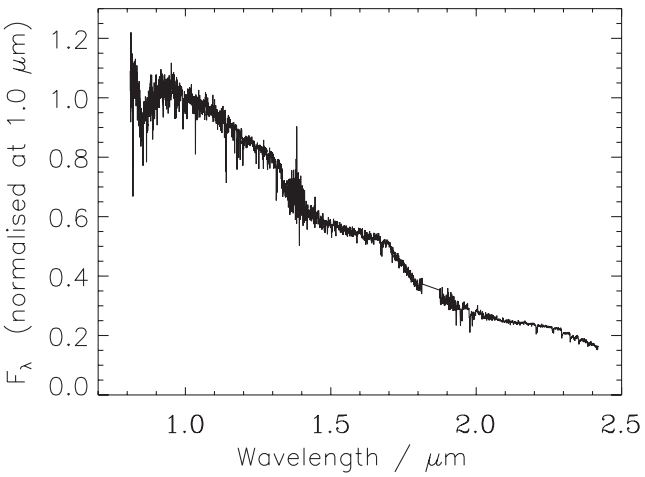

Figure 9. Our *JHK* SpeX spectrum of LHS 6176A.

Table 8. Properties of HD 118865AB.

	HD 118865A	HD 118865B
RA (J2000)	13 39 34.33[a]	13:39:43.79
Dec. (J2000)	+01 05 18.12[a]	+01:04:36.40
$PM_{\alpha\cos\delta}$ (mas yr^{-1})	-95.75 ± 0.80[a]	-130.23 ± 14.58
PM_{δ} (mas yr^{-1})	-48.81 ± 0.54[a]	-23.76 ± 14.72
Spectral type	F5	T5
B_T	8.52 ± 0.02[b]	–
V_T	7.98 ± 0.01[b]	–
J (2MASS)	6.98 ± 0.02[c]	–
$J-H$ (2MASS)	0.25 ± 0.05[c]	–
$H-K_s$ (2MASS)	0.06 ± 0.05[c]	–
J (UKIDSS)	–	18.08 ± 0.04
$Y-J$ (UKIDSS)	–	1.07 ± 0.06
$J-H$ (UKIDSS)	–	-0.31 ± 0.14
$H-K$ (UKIDSS)	–	0.0 ± 0.13
[3.6]	–	16.93 ± 0.01
[4.5]	–	16.08 ± 0.02
π	16.02 ± 0.86[a]	–
Distance	$62.4^{+3.2}_{-3.6}$ pc	–
[Fe/H]	0.09 ± 0.09[d]	–
Age	1.5–4.9 Gyr (1σ interval)[d]	
$\log(L_*/L_\odot)$	–	-5.24 ± 0.04
Projected separation	148 arcsec, ∼9200 au	

[a]van Leeuwen (2007); [b]Høg et al. (2000); [c]From 2MASS All-Sky Point Source Catalog; [d]Casagrande et al. (2011).

6.3 HD 118865 AB

The probability of chance alignment for HD 118865A and ULAS J1339+0104 is 0.2 per cent, which is significantly higher than has been found previously for wide binary systems in our searches (e.g. Burningham et al. 2009; Pinfield et al. 2012). This is due to the combination of a large range of plausible distances for the T5 dwarf (40–95 pc, allowing for the possibility that it is a binary) and the relatively low proper motions of the proposed components. However, if our range of plausible distances is reduced to account only for the spread in T5 absolute magnitudes (rather than T4.5–T5.5 and binarity; since the former arguably already incorporates these effects), then we find the probability of chance alignment is reduced to 0.001 per cent. On balance, it is reasonable to proceed with analysis of this system as a bona fide common proper motion binary system, although we caution that a parallax for the T dwarf is required to confirm beyond doubt that this pair is associated.

In many respects, HD 118865A represents an ideal benchmark primary star. With a Hipparcos parallax (Perryman et al. 1997; van Leeuwen 2007), kinematic and model-based age estimates and well-measured metallicity (Casagrande et al. 2011), it avoids many of the pitfalls associated with less massive primary stars. Indeed, the metallicity diagnostics for the M dwarf primaries that dominate the substellar wide binary sample have been benchmarked against nearby binary systems containing FGK primary stars for these reasons. The properties of HD 118865A are summarized in Table 8.

To determine the properties of HD 118865B, we have followed an identical method to that applied for LHS 6176B (see Section 6.2.3). In this case, we have used models spanning the $T_{\rm eff} = 1000$–1400 K range, $\log g = 4.5$–5.5 and solar metallicity. After a first round of calculations, we found that the lowest gravity models were inconsistent with our estimated luminosity and age for the system, and so were excluded from the next iteration. We find the flux from HD 118865B to be $F_{\rm bol} = 1.47 \pm 0.14 \times 10^{-16}$ W m^{-2} and the luminosity to be $L_{\rm bol} = 6.85 \pm 1.00 \times 10^{21}$ W or $\log(L_*/L_\odot) = -4.75 \pm 0.07$.

If we assume that HD 118865B is a single object with an age of between 1.5 and 4.9 Gyr, then we find that its luminosity corresponds to a radius of $0.080\,R_\odot < R < 0.091\,R_\odot$ and a mass of $0.065\,M_\odot > M > 0.040\,M_\odot$, with corresponding temperature $1320\,{\rm K} > T_{\rm eff} > 1240\,{\rm K}$ and gravity $5.4 > \log g > 5.0$, according to the COND evolutionary models. If HD 118865B is an equal-mass binary, these properties should be revised to $0.079\,R_\odot < R < 0.095\,R_\odot$, $0.060\,M_\odot > M > 0.030\,M_\odot$, $1120\,{\rm K} > T_{\rm eff} > 1020\,{\rm K}$ and $5.4 > \log g > 5.0$.

6.4 HIP 73786B

Scholz (2010) and Murray et al. (2011) independently identified HIP 73786AB as a wide binary system consisting of a metal poor K5 dwarf moving in common motion with a T6p dwarf, and we recovered it with our search. At the time of its discovery longer wavelength photometry for the T dwarf was not available, and so no bolometric flux estimate was made. The advent of the *WISE* all-sky release, however, allows such an estimate to made relatively conveniently and for the purposes of including this object in subsequent discussion we have estimated the properties for HIP 73786B following the same method as described in the previous sections.

In this case, we have used BT Settl models spanning the $T_{\rm eff} = 800$–1200 K range, $\log g = 4.5$–5.5 and solar metallicity, scaling the longer wavelength portions to match the *W*1 and *W*2 survey photometry, and stitching them to our flux-calibrated NIR spectrum at 2.4 μm. As before, the regions blueward of 1 μm have been filled using models scaled to match the *Y*-band flux in our NIR spectrum. The current lack of low-metallicity BT Settl models in this temperature range has prevented us from using models covering the entire expected parameter range for this object, but since we scale the models to match the long-wavelength photometry, we do not expect this to have a significant impact on our flux estimate. We find the flux from HIP 73786B to be $F_{\rm bol} = 5.31 \pm 0.30 \times 10^{-16}$ W m^{-2} and the luminosity to be $L_{\rm bol} = 2.20 \pm 0.12 \times 10^{21}$ W or $\log(L_*/L_\odot) = -5.24 \pm 0.04$.

Murray et al. (2011) loosely constrained the age of the HIP 73786AB system to be 1.6–10 Gyrs. If we accept this age for HIP 73786B, then from its luminosity and the COND evolutionary models we infer a radius of $0.076\,R_\odot < R < 0.096\,R_\odot$ and a mass of $0.063\,M_\odot > M > 0.028\,M_\odot$, with corresponding temperature $1020\,{\rm K} > T_{\rm eff} > 910\,{\rm K}$ and gravity $5.5 > \log g > 4.9$ under the assumption that it is a single object. If HIP 73786B is an equal luminosity binary then we derive a radius $0.076\,R_\odot < R < 0.098\,R_\odot$, $0.058\,M_\odot > M > 0.022\,M_\odot$, $860\,{\rm K} > T_{\rm eff} > 760\,{\rm K}$ and $5.4 > \log g > 4.8$.

6.5 Properties of the UKIDSS wide binary sample

The relatively uniform manner in which our wide binary systems have been identified allows us to draw some preliminary conclusions about the properties of the late-T dwarf wide binary companion population. First, it is apparent that with 7 wide binary companions out of a total of 92 T dwarfs within our proper motion >100 mas yr^{-1} selection, we can place a minimum value of 8 per cent on the wide binary companion fraction. This is consistent with the minimum value of 5 per cent found by Gomes et al. (2013) for L dwarfs. This represents a lower limit, as our selection of candidate primary stars is limited by available photometry for faint red primary star candidates, as highlighted in Section 6.1. This source of incompleteness also explains another feature of our binary sample. That is, that the latest type T dwarfs are significantly over-represented, with 25 per cent of T8 and later objects (3 out of 12 in our selection)

appearing as wide binary companions, compared to 5 per cent for T4.5–T6.5 dwarfs. Whether this suggests that the true wide binary companion fraction for T dwarfs is nearer the 25 per cent value seen for the latest type objects is an open issue that will require significantly improved selection of earlier type binary systems.

The scarcity of earlier type wide binary companions can be understood not in terms of bias within our proper motion sample, but rather as a reflection of the relative space densities of late- and mid-type T dwarfs, and the bias against fainter red candidate primary stars with Tycho photometry. The space density of the T8 and later dwarfs is significantly (e.g. four times) higher than that of mid-type T dwarfs. This means that a larger proportion of the latest type objects will be found at close distances, where the LSPM and NOMAD catalogues are relatively complete for primary stars and proper motions are larger. The earlier type objects, however, will be less numerous in the nearby volume, and so larger fraction will be found at larger distances, where the catalogues of potential primary stars are most incomplete for the most common M dwarf type of primaries, and proper motions are smaller making reliable identification more problematic. It thus appears, at this stage, that we can (weakly) conclude that the spectral type distribution of T dwarfs as wide binary companions does not appear to be drastically different from that of isolated (i.e. single) T dwarfs.

6.6 The colours of benchmark T dwarfs and the latest model atmospheres

Fig. 10 shows $H - K$ versus $H - [4.5]$ colour–colour plots for the compendium of MKO and *Spitzer* photometry of late-T dwarf benchmark systems including that presented by Leggett et al. (2010a) and updated with additional photometry presented here. Fig. 11 shows similar $Y - J$ versus $J - W2$ colour–colour diagrams for benchmark T dwarfs with *WISE* photometry. The properties of the benchmarks are summarized in Table 9.

Overlaid on the two panels of Figs 10 and 11 are colour tracks for the models of Saumon et al. (2012) and Morley et al. (2012), and a 1σ box for the model-predicted colours of each benchmark is connected to each objects observed colours (where a model prediction is available on these grids). These models incorporate the latest NH_3 opacities from Yurchenko, Barber & Tennyson (2011), and a new treatment of collisionally induced H_2 absorption (CIA H_2; Abel et al. 2011, 2012). The Morley et al. (2012) models also include the effects of proposed sulphide and alkali condensates, which may become important in atmospheres below $T_{\rm eff} \approx 800$ K. Low-metallicity versions of these models are not yet available, so it is not possible to assess if these recent developments have impacted the predictions for low-metallicity atmospheres.

It is difficult to draw firm conclusions about the success or otherwise of the different models by comparing the colour predictions to the observed colours of the benchmark systems as deficiencies in the models can be both masked and amplified by their differing impacts at the wavelengths of the two photometric bands being compared in any particular case. Nonetheless some of the principal differences between the models and the observations can be attributed to known deficiencies in the model grids. For example, the predicted $H - [4.5]$ and $J - W2$ colours for the solar-metallicity benchmarks are almost universally too red in both Figs 10 and 11. This is due to the fact that neither model set includes non-equilibrium chemistry, which has been demonstrated to be important for determining the emergent flux in the 4−5 μm region (e.g. Saumon et al. 2006).

The most obvious conclusion that can be drawn from examining the colours of the benchmark systems is that metallicity and gravity both have a significant impact on the near to mid-infrared colours of late-T dwarfs, along with the (generally considered) dominant influence of temperature. For example, the low-gravity benchmark Ross 458C appears only 0.15–0.2 mag redder in $H - [4.5]$ than Gl 570D and HD 3651B, despite being approximately 100K cooler. Comparing the colours of Wolf 940B with Gl 570D and HD 3651B suggests that $\Delta T_{\rm eff} = -100$ K should (approximately) correspond to $\Delta(H - [4.5]) = +0.6$ mag. This implies that the low gravity of Ross 458C imposes a blueward shift of ∼0.4 mag for $\Delta \log g \approx -0.7$ dex, or roughly +0.1 mag per +0.18 dex in $\log g$.

The impact of metallicity appears to be even more significant, with lower metallicity objects appearing redder (in e.g. $H - [4.5]$ or $J - W2$) at a given $T_{\rm eff}$ than objects with near-solar metallicity. For example, comparing the colours of LHS 6176B and BD+01 2920B with the warmer solar metallicity objects suggest that a shift of Δ[Fe/H] ≈ −0.3 dex can give rise to a shift of $\Delta(H - [4.5]) \approx +0.6$, if we assume that LHS 6176B is an unresolved binary with a $T_{\rm eff} = 645 \pm 55$ K and $\log g = 5.05 \pm 0.25$. If LHS 6176B is a single object then the apparent shift in colour due to its metallicity would more like 0.9 mag. This is somewhat higher than for BD+01 2920B, and further argues for a binary interpretation for this object.

This effect has been suggested previously, based on comparisons of photometric colours and atmospheric models (Leggett et al. 2009, 2010a), and can largely be attributed to increased flux in the 4.5 μm region due to reduced CO opacity. Comparison of solar and low-metallicity cases for the BT Settl (Allard et al. 2010) models that were first shown in Pinfield et al. (2012) and the Saumon & Marley (2008) models indicates that although both predict a colour shift due to lower metallicity, both underpredict its magnitude. The Saumon & Marley (2008) models predict $\Delta(H - [4.5]) \approx +0.2$ for Δ[M/H] = −0.3, whilst the BT Settl grid predicts $\Delta(H - [4.5]) \approx +0.3$ for the same change at $T_{\rm eff} = 700$ K, compared with the $\Delta(H - [4.5]) \approx +0.6$ shift seen in our benchmarks.

The slightly stronger metallicity dependence that the BT Settl model colours exhibit can likely be attributed to the combination of two factors. First, the BT Settl models include non-equilibrium chemistry for CO_2, which will result in a greater relative increase in flux in the [4.5] band in response to reducing the metallicity. Secondly, the BT Settl models include additional methane opacity in the H band, where the methane line lists are very incomplete, based on a statistical estimate of the contributions from the hot vibrational bands. With decreased metallicity these hot bands are likely to become more important as the chemistry shifts in favour of CH_4 over CO and CO_2 (e.g. Lodders & Fegley 2002). Indeed, it is likely that the failure of the models to accurately reproduce the strong metallicity dependence of the $H - [4.5]$ colour can be partially attributed to the incomplete nature of the methane line lists.

The strong dependence on metallicity of the $H - [4.5]$ and $J - W2$ colours should be considered carefully when using these colours to estimate the properties of cool brown dwarfs. Two specific examples worth highlighting in this context are: SDSS 1416+1338B, the second reddest known T dwarf in $H - [4.5]$ despite a spectral type of T7.5 (Burningham et al. 2010a); and WISEPC J1828+2650, which is the reddest known Y dwarf in the same colours (Cushing et al. 2011; Leggett et al. 2013). In the case of the former, its anomalously red colour was initially interpreted as being indicative of $T_{\rm eff} \approx 500$ K (Burningham et al. 2010a). However, its parallax has since been measured, and its luminosity appears to rule out such a low temperature, and its extreme colours are now attributed to some combination of low metallicity and/or high gravity with a significantly higher $T_{\rm eff}$ (Murray et al., in preparation). In the case of WISEPC J1828+2650, Leggett et al. (2013) argues that its

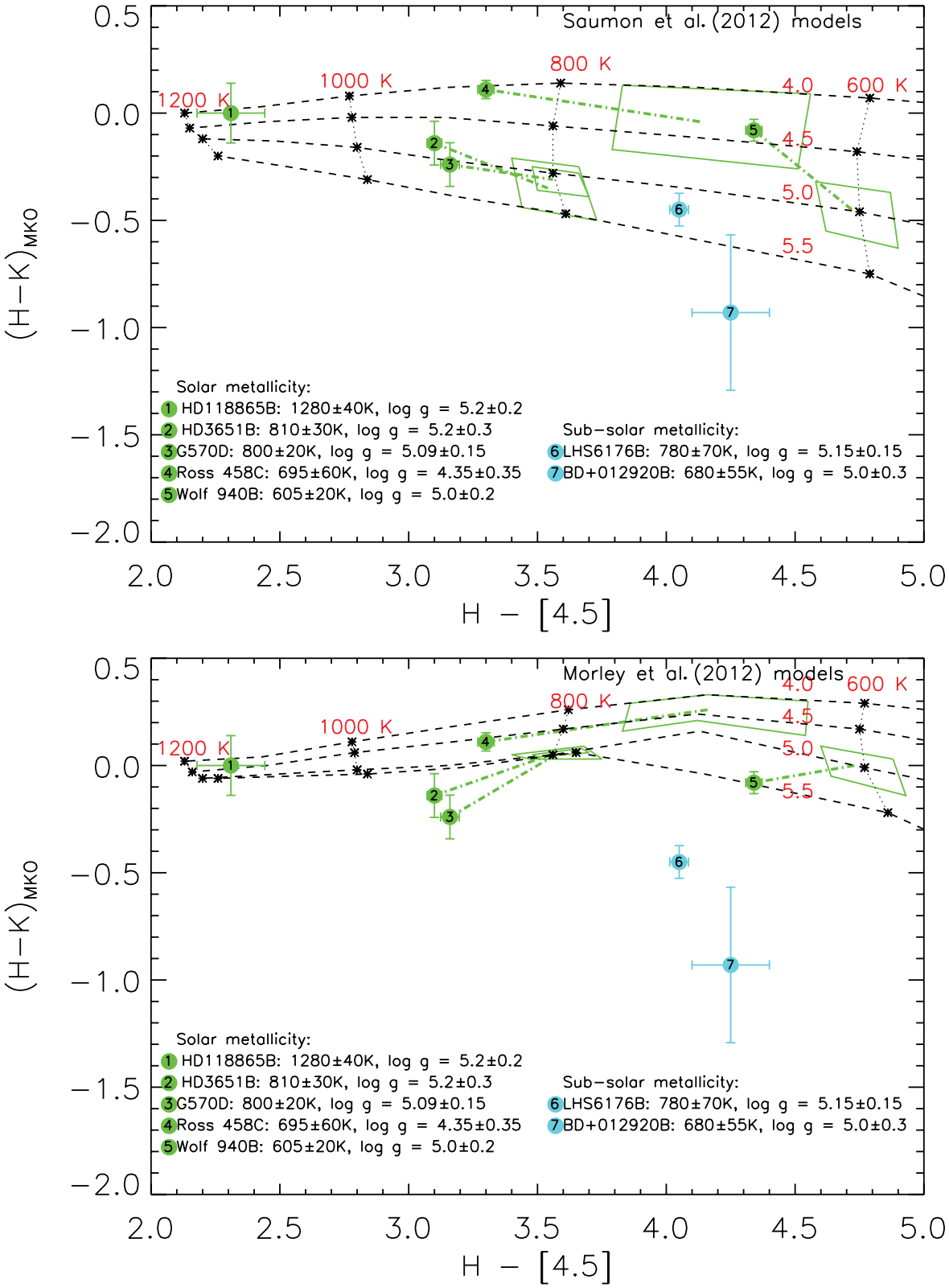

Figure 10. $H - [4.5]$ versus $H - K$ colour–colour plots for the compilation of photometry for T dwarfs from Leggett et al. (2010a) and benchmark systems from the literature, along with new photometry and benchmarks presented in this paper. Benchmark systems with roughly solar metallicity are shown in green, whilst those with subsolar metallicity are shown in blue. Model colour tracks for Saumon et al. (2012), top panel, and Morley et al. (2012), bottom panel, are shown for comparison. The latter assumed $f_{sed} = 5$. The models shown are all solar metallicity, and the T_{eff} and $\log g$ values are indicated on the colour sequences. Each benchmark object is linked to a 1σ box indicating the model prediction for its colours.

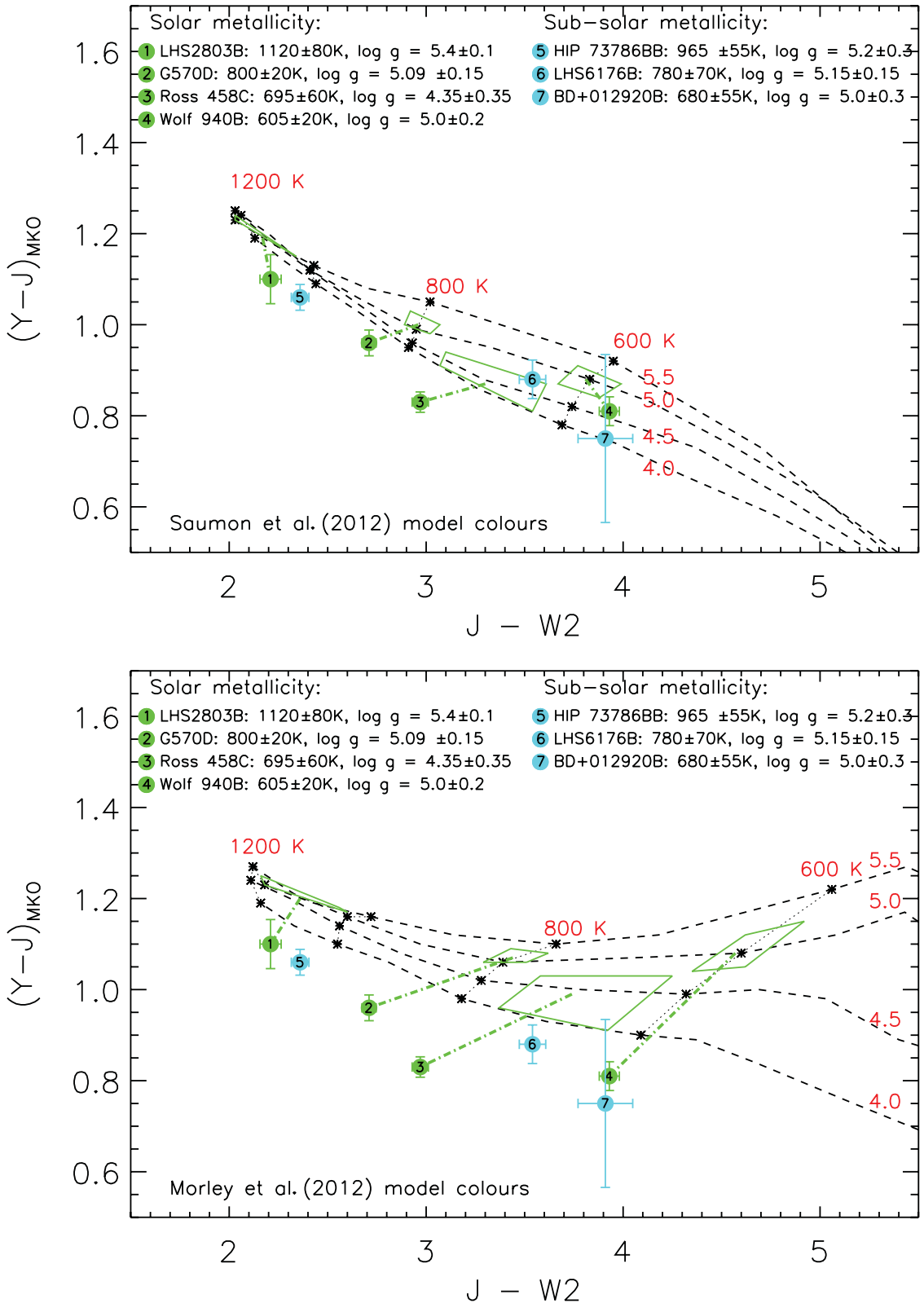

Figure 11. $J - W2$ versus $Y - J$ colour–colour plots for the UKIDSS T dwarfs with *YJ* and *WISE* photometry and benchmark systems from the literature, along with new photometry and benchmarks presented in this paper. Benchmark systems with roughly solar metallicity are shown in green, whilst those with subsolar metallicity are shown in blue. Model colour tracks for Saumon et al. (2012), top panel, and Morley et al. (2012), bottom panel, are shown for comparison. The latter assumed $f_{\rm sed} = 5$. The models shown are all solar metallicity, and the $T_{\rm eff}$ and log g values are indicated on the colour sequences. Each benchmark object is linked to a 1σ box indicating the model prediction for its colours.

Table 9. Summary of the properties of the benchmark systems shown in Figs 10 and 11.

Name	$T_{\rm eff}$ (K)	log g	[Fe/H]
Wolf 940B	605 ± 20[a]	5.0 ± 0.2[a]	+0.02 ± 0.05[b]
BD+01 2920B	680 ± 55[c]	5.0 ± 0.3[c]	−0.36 ± 0.06[c]
Ross 458C	695 ± 60[d]	4.35 ± 0.35[d]	+0.09 ± 0.05[b]
LHS 6176B	780 ± 70[e]	5.15 ± 0.15[e]	−0.30 ± 0.10[e]
Gl 570D	800 ± 20[f]	5.1 ± 0.15[f]	+0.09 ± 0.04[f]
HD 3651B	810 ± 30[g]	5.3 ± 0.2[g]	+0.12 ± 0.04[g]
HIP 73786B	965 ± 55[e]	5.2 ± 0.3[e]	−0.30 ± 0.1[h]
LHS 2803B	1120 ± 80[i]	5.4 ± 0.1[i]	∼0.0[i]
HD 118865B	1280 ± 40[e]	5.2 ± 0.2[e]	0.09 ± 0.10[e]

[a]Leggett et al. (2010b); [b]From the $V-K$ calibration of Neves et al. (2012); [c]Pinfield et al. (2012); [d]Burningham et al. (2011); [e]This work; [f]Saumon et al. (2006); [g]Liu, Leggett & Chiu (2007); [h]Murray et al. (2011); [i]Deacon et al. (2012).

extremely red $H-[4.5]$ can only be consistent with its luminosity (which is higher than for some earlier and bluer Y dwarfs) if it is either younger than 50 Myr (with a mass $<1M_{\rm Jup}$) or an unresolved binary system. Given the example of SDSS J1416+1348B and the colours of benchmark systems in Fig. 10 (albeit at higher $T_{\rm eff}$), it seems reasonable to also offer a third (somewhat speculative) interpretation e.g. this object may in fact be somewhat warmer and more massive, but with its colours reddened by low metallicity, high gravity and/or their combined impact on cloud properties.

It is important to emphasize that what follows is based on a highly simplistic extrapolation of the trends we have identified at cool T dwarf temperatures ($T_{\rm eff}=600-800$K) to Y dwarf temperatures some 200–500 K cooler. We note that at these low temperatures the gravity range is limited by the long cooling times for the most massive objects (e.g. Saumon & Marley 2008), so the bulk of any colour shift at a given $T_{\rm eff}$ must be driven by metallicity. If we apply the shift that we have identified at higher $T_{\rm eff}$ of $\Delta H-[4.5]=+0.6$ mag for roughly Δ[M/H] $=-0.3$ dex, and assume that the shift is entirely driven by extra flux in [4.5], we find that a halo-like low metallicity of [M/H] ≈ -1 could provide the additional 1.5−2.0 mag of flux seen in the 4.5 μm region from WISEPC J1828+2650 (Beichman et al. 2013; Leggett et al. 2013). Although the tangential velocity of WISEPC J1828+2650 has been measured as $51\pm5\,{\rm km\,s^{-1}}$ (Beichman et al. 2013), which is most consistent with thin-disc membership, this does not rule out a metallicity as low as [M/H] ≈ -1. Its NIR colours may also lend weight to the low-metallicity interpretation. Leggett et al. (2013) report $H-K=-0.63\pm0.43$ for this target, making it the bluest known Y dwarf in these colours, which at higher temperatures would be associated with low metallicity and/or high gravity. Its red $J-H=+0.63\pm0.33$ colour is also not at odds with low metallicity. For example, in the T dwarf regime metallicity has little impact on the $J-H$ colours of T dwarfs (see Fig. 12). Interestingly, the BT Settl models predict redder $J-H$ colours for lower metallicity T dwarfs, with a more pronounced effect at lower $T_{\rm eff}$. It will be interesting to see how the picture of the impact of varying metallicity develops as new models grids are calculated and new benchmark systems are discovered over the coming years.

7 THE DISTRIBUTION OF T DWARF COLOURS

Beyond comparisons to our benchmark sample, it is also interesting to make more qualitative comparisons between the spread in colours predicted by the atmospheric models and that seen for the wider T dwarf population. Such comparisons provide insight as to whether the impact of varying parameters such as gravity in models results in colour shifts of the similar proportions seen in the data.

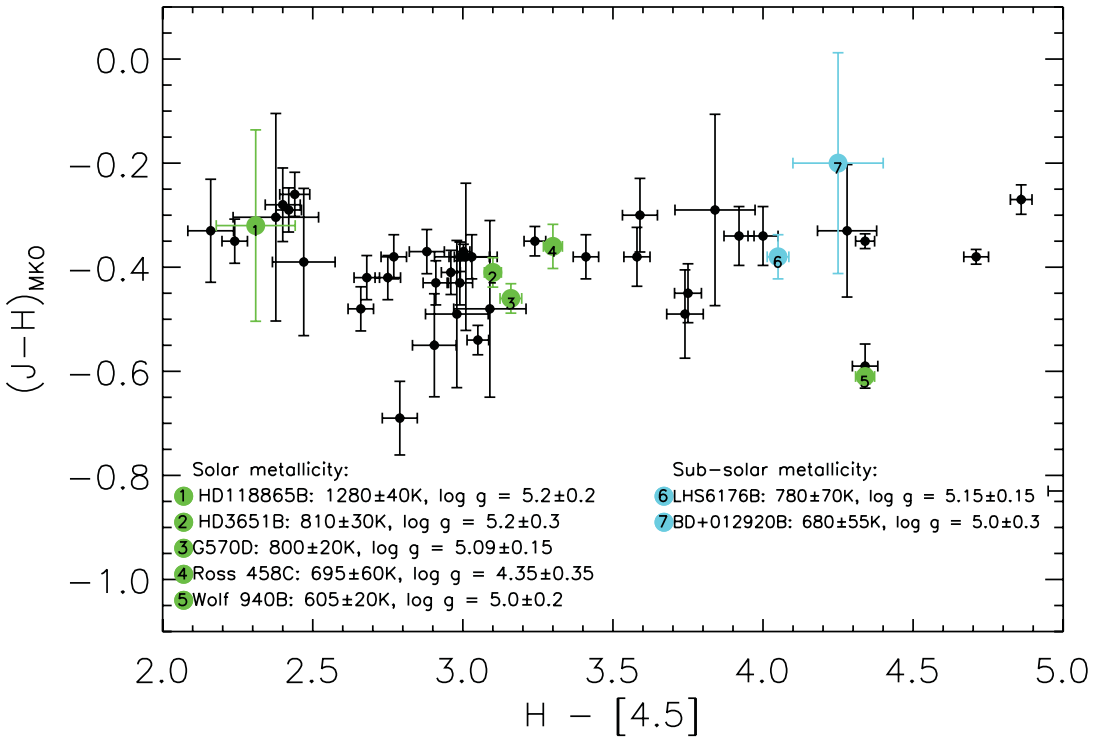

Figure 12. $H-[4.5]$ versus $J-H$ colour–colour plots for the compilation of photometry for T dwarfs from Leggett et al. (2010a), along with new photometry presented in this paper. Benchmark systems are indicated and numbered as for Fig. 10.

Fig. 10 shows $H - K$ versus $H - [4.5]$ colour–colour plots for the compendium of MKO and *Spitzer* photometry of late-T dwarfs presented by Leggett et al. (2010a), updated with additional photometry presented here. The benchmark T dwarfs are labelled as for Fig. 10. Fig. 11 shows similar $Y - J$ versus $J - W2$ colour–colour diagrams for the UKIDSS T dwarfs with *WISE* photometry. These plots reveal that the two model sets are each able to reproduce the spread in late-T dwarf colours in one of $H - K$ or $Y - J$, but not both. We note that neither set of models include refractory condensate clouds that are important at warmer $T_{\rm eff}$, and so they are not expected to match the data for earlier type T dwarfs, which they do not.

The upper panel of Fig. 13 suggests that the revised CIA H_2 opacity included in the Saumon et al. (2012) models has significantly improved the match to the spread and pattern seen in $H - K$ colours over previous model grids, which tended to predict $H - K$ that was too blue, and descending to more negative values rapidly with $T_{\rm eff}$ (e.g. Burningham et al. 2009; Pinfield et al. 2012). The lower panel of Fig. 13 shows the colour tracks for the Morley et al. (2012) models, which, in addition to using the Saumon et al. (2012) CIA H_2 opacity also include alkali and sulphide clouds that may become important at $T_{\rm eff} \lesssim 800$ K. These models show slightly redder $H - K$, with a smaller spread in $H - K$ colour as a function of gravity. The reduced spread in $H - K$ arises as higher gravity leads to thicker cloud layers, pushing the colours redward and partially counteracting the blueward trend that would otherwise result from the increased CIA H_2 opacity.

As can be seen in Fig. 14, the introduction of the low-$T_{\rm eff}$ clouds tends to increase the $Y - J$ spread due to gravity, as the effect of increasing gravity on pressure sensitive gas-phase opacities and the impact of thickening cloud layers with increasing gravity both tend to give redder $Y - J$ colours, and here the cloudy models better reproduce the observed spread in colours than those without clouds. Variations in metallicity may have a significant impact on cloud properties. Since only solar metallicity realizations are available for the new model grids, it is thus impossible to determine whether their failure to reproduce the observed colour spread in both Figs 13 and 14 merely reflects this fact, or if it suggests some other as-yet unidentified shortcoming in the theoretical approach.

We have presented plots similar to Fig. 13 in previous work (e.g. Leggett et al. 2010a; Burningham et al. 2011; Pinfield et al. 2012) comparing the colours of the late-T dwarf sample with the previous generation of models that did not include the improved CIA H_2 treatment, nor the low-temperature sulphide and alkali condensates proposed by Morley et al. (2012). The previous generations of models typically predicted significantly bluer colours in $H - K$, with $H - K$ becoming increasingly blue with decreasing $T_{\rm eff}$. The preference for redder $H - K$ colours amongst the late-T sample led us to conclude that there was some bias in favour of young, low-gravity objects either within our selection or in the population itself. The model colour tracks in the top panel of Fig. 13 match the observed spread in $H - K$ colours very well, with no need for such a young-age bias in the sample. Indeed, when both Figs 13 and 14 are considered, the strong model dependence of previous conclusions drawn from such plots is apparent.

8 KINEMATICS OF THE UKIDSS LATE-T DWARF SAMPLE

The implication from Figs 10–14 that the late-T dwarf sample is not dominated by young low-mass objects as had been previously suggested (Leggett et al. 2010a; Burningham et al. 2011; Pinfield et al. 2012) highlights the inherent model dependency of determining the properties of cool brown dwarfs from colour–colour diagrams. To shed further light on this issue, we have constructed a J-band-reduced proper motion diagram for our sample (see Fig. 15). It is apparent that there are no obvious features which distinguish the distribution of kinematic properties between the latest type T dwarfs and the earlier type objects in UKIDSS. A more robust statistical treatment to assess this will be presented by Smith et al. (in preparation). Nonetheless, it appears that the late-T dwarf sample is kinematically indistinct from the mid-T dwarfs, which themselves have been shown to match the kinematics of the earlier type L and M dwarfs, reflecting the typical Galactic disc age distribution (Faherty et al. 2009).

We note that our earliest type objects, in the T4 class, appear to be preferentially distributed to higher speeds. Previous detailed studies of T dwarf kinematics (e.g. Faherty et al. 2009) argue this is not a real effect. It likely arises as a result of the combination of our $J - H < 0.1$ and $J - K < 0.1$ colour requirements, which may exclude T4 dwarfs with redder $H - K$ colours, and $J - H$ colours near our colour cut-offs. As such, we are likely to preferentially select objects that are bluer in $H - K$, due to high gravity and/or low metallicity, in this region. Such objects can be expected to be typically older, and thus will exhibit higher velocities.

9 UPDATED SPACE DENSITY ESTIMATE

We now have near-complete follow-up of all candidates with $J < 18.8$ in UKIDSS LAS DR8. This covers 2270 square degrees of sky within the SDSS DR8 footprint. Our significantly increased sample of ≥T6 dwarfs allows us to improve on the space density estimate derived in Burningham et al. (2010b). However, the optimization of our selection method since that work (to include CH_4 imaging) somewhat complicates our completeness correction and bias selection. Unifying a sample selected in a slightly inhomogeneous manner, such as ours, to derive a space density is best achieved via a Bayesian parameter estimate method. For this reason, we defer this more rigorous derivation of the space density to a future work, since it is beyond the scope of this discovery paper. Here, instead, we follow the method of Pinfield et al. (2008) and Burningham et al. (2010b), and derive approximate correction factors for the incompleteness introduced by our different photometric cuts in the same manner as we previously did for correcting for our $J - H$ selection cut, and simply scale these by the proportion of the sample to which they were applied.

There are 76 dwarfs with measured spectral types of T6 or later with $J < 18.8$ in the region of sky covered by UKIDSS DR8 and SDSS DR8 probed by our searches. Of these, 39 have already had spectra published (Tsvetanov et al. 2000; Burgasser et al. 2004; Chiu et al. 2006, 2008; Lodieu et al. 2007b; Pinfield et al. 2008; Burningham et al. 2008, 2009, 2010b; Delorme et al. 2008; Kirkpatrick et al. 2011; Scholz et al. 2012), and 37 have been presented for the first time here. In addition, we have four targets with $CH_4s - CH_4l < -0.5$ which have not yet been followed up spectroscopically (see Table 1). The CH_4 types for two of these objects are constrained to earlier than T5.5, whilst two are consistent with types as late as T6. We thus include the latter two of these four in our sample, bringing it to a total of 78 T6 and later dwarfs.

We also have one target for which we do not have well-calibrated methane photometry and no spectroscopic observations: ULAS J 0800+1908 has a LIRIS methane colour of $H - CH_4l = -0.73$. This is suggestive of a type intermediate between that of the T7 dwarf ULAS J0746+2355 which has LIRIS $H - CH_4l = -0.87$ and the T6.5 dwarf ULAS J1023+0447.

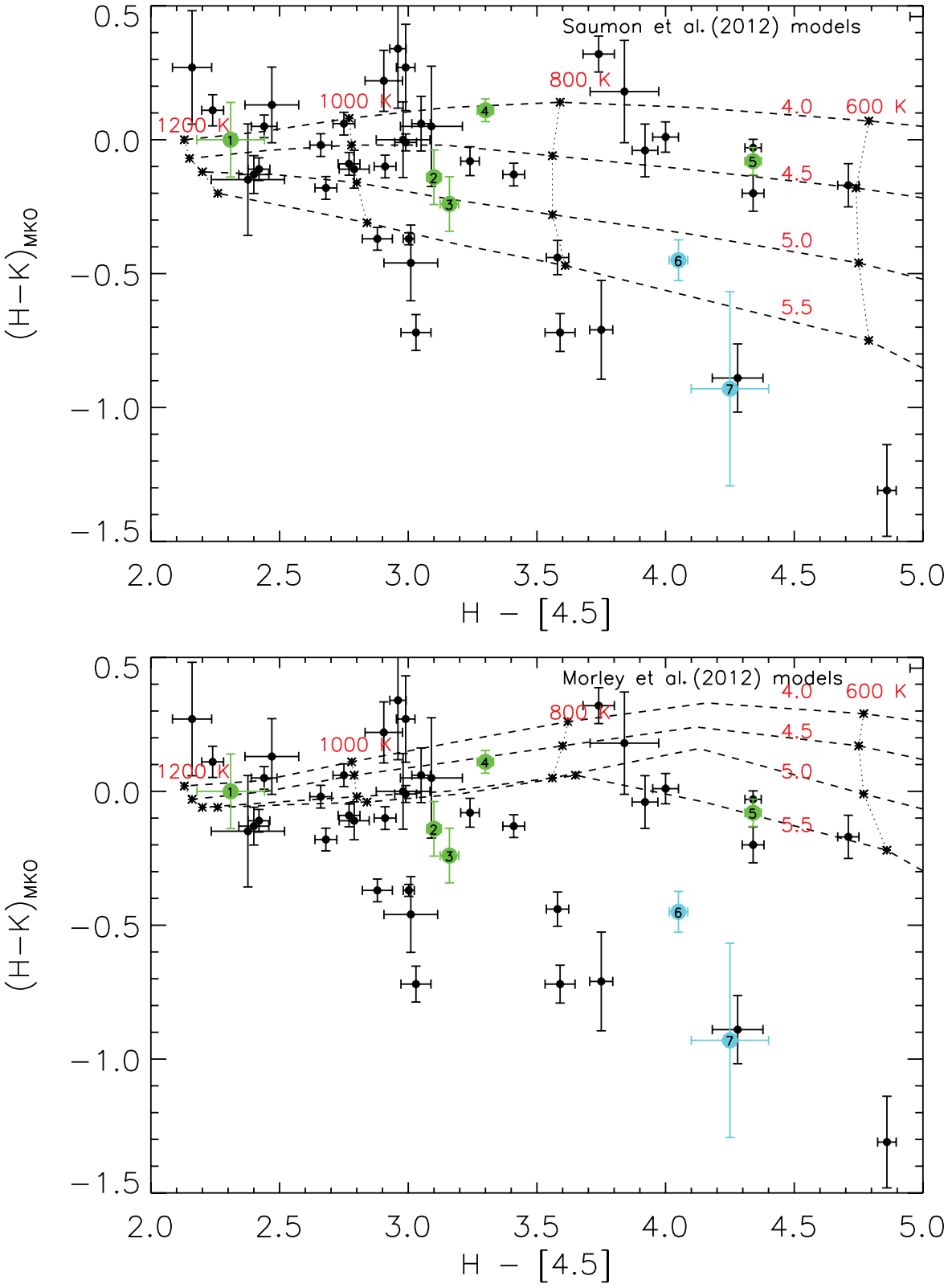

Figure 13. $H - [4.5]$ versus $H - K$ colour–colour plots for the compilation of photometry for T dwarfs from Leggett et al. (2010a), along with new photometry presented in this paper. Model colour tracks for Saumon et al. (2012), top panel, and Morley et al. (2012), bottom panel, are shown for comparison, the latter assumed $f_{\rm sed} = 5$. The models shown are all solar metallicity, and the $T_{\rm eff}$ and $\log g$ values are indicated on the colour sequences. Benchmark systems are indicated and numbered as for Fig. 10.

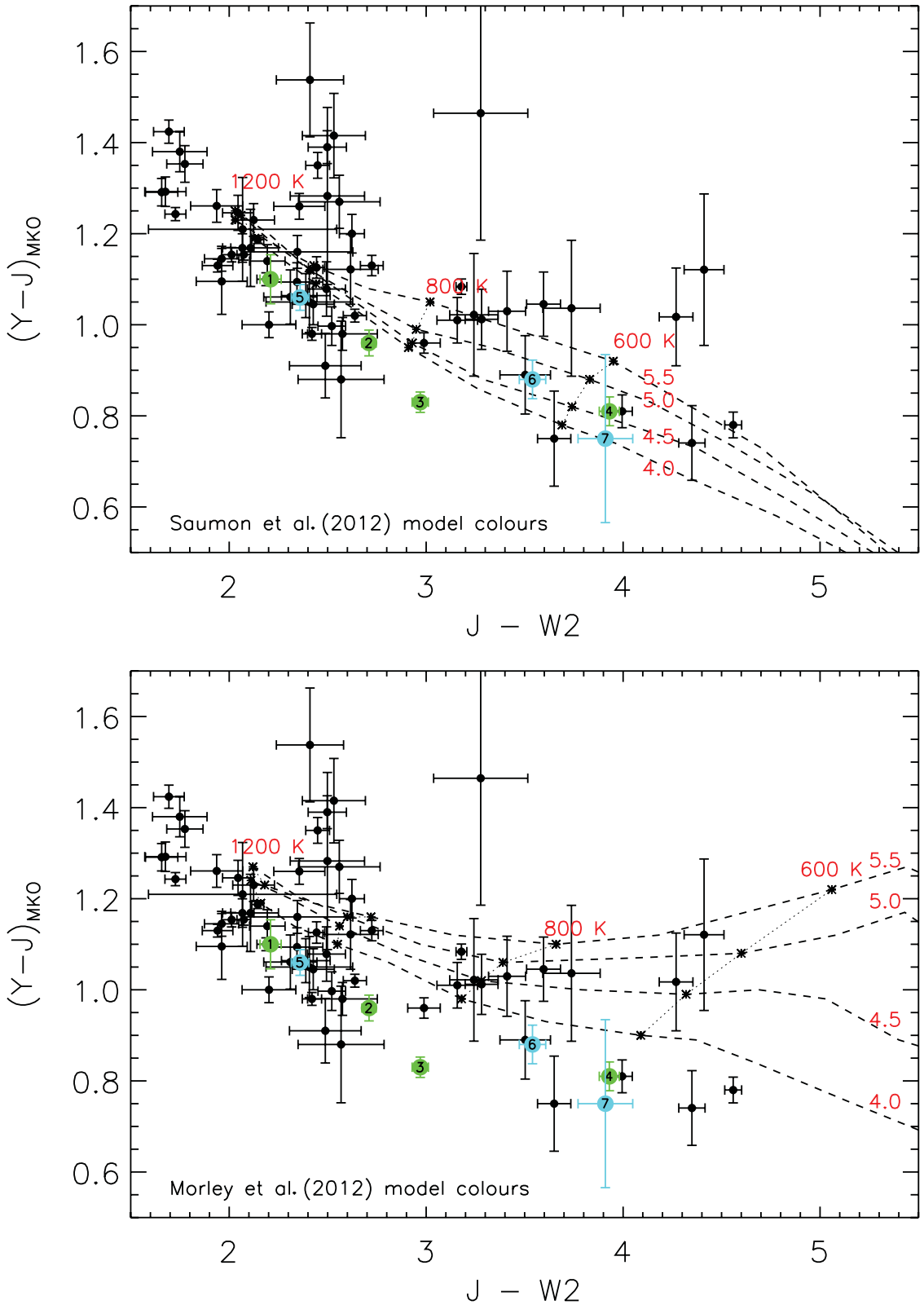

Figure 14. $J - W2$ versus $Y - J$ colour–colour plots for the UKIDSS T dwarfs with *YJ* and *WISE* photometry. Model colour tracks for Saumon et al. (2012), top panel, and Morley et al. (2012), bottom panel, are shown for comparison, the latter assumed $f_{\rm sed} = 5$. The models shown are all solar metallicity, and the $T_{\rm eff}$ and $\log g$ values are indicated on the colour sequences. Benchmark systems are indicated and numbered as for Fig. 11.

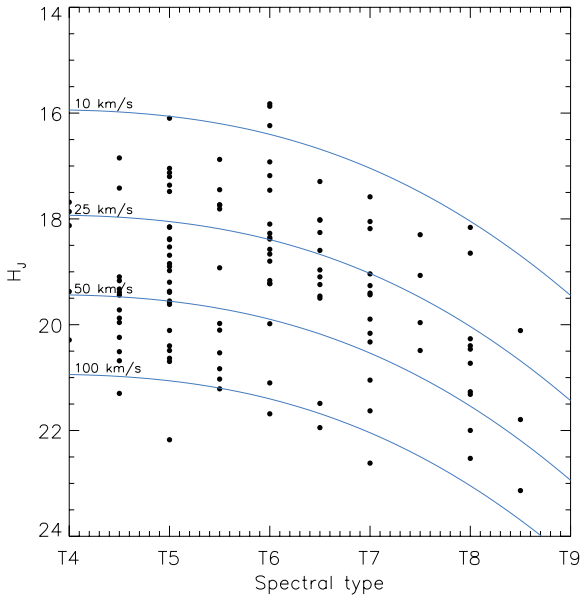

Figure 15. A *J*-band-reduced proper motion versus spectral type diagram for the UKIDSS late-T dwarfs with well measured proper motions. Iso-V_{tan} contours have been overplotted using by applying the Dupuy & Liu (2012) M_J-spectral type relations. To apply these relations, we have adopted Cushing et al. (2011) spectral types for the latest type objects.

However, the lack of a spectral type calibration for this methane colour prevents us from assigning this object to a specific spectral type bin in our sample. Instead, we incorporate it into the uncertainty in the T6 and T7 bins.

Two-thirds of our sample were selected using the method presented in Pinfield et al. (2008) and Burningham et al. (2010b). For this method, we found that a correction factor of 1.03 should be applied to all spectral type bins, to account for the biases introduced by the following effects: scatter out of our $J - H < 0.1$ selection due to photometric error; mismatching of bona fide T dwarfs with background stars in our SDSS cross-match; wide binary companions to stars (which should be excluded from a T dwarf primary space density). We do not correct for the possibility of excluding objects with the $Y - J < 0.5$ that we applied to *YJ*-only selected targets fainter than $J = 18.5$ since no T dwarfs have yet been found with such colours. Although *Y* dwarfs are now known with such blue $Y - J$ colours (Leggett et al. 2013), we are not sensitive to such objects due to their inherently faint nature.

One-third of our sample was selected using the new follow-up method described in Section 3. Since this method uses the same starting point of *YJH* and *YJ*-only colour selections, it is subject to the same biases. In addition to those, however, it also includes bias due to the z' band and CH_4 follow-up criteria. The follow-up z'-band observations delivered typically uncertainties of ± 0.2 mag for faint red T dwarfs, and considerably smaller uncertainties for bluer M dwarfs. We ruled out from further investigation targets that had $z' - J < 2.5$ after z'-band follow-up. This is roughly 3σ bluer than the bluest measured $z' - J$ for late-T dwarfs. As such, we estimate that less than 1 per cent of bona fide late-T dwarfs would be scattered out of our selection during the z'-band follow-up step.

Our CH_4 photometry step may also exclude some objects since we only obtained spectroscopy for those objects with $CH_4s - CH_4l < -0.5$. The strong dependence of CH_4 colour on spectral type means that the fractional bias must be determined for each spectral type bin. We have estimated the number of objects that we would expect to scatter out of our $CH_4s - CH_4l < -0.5$ cut by summing the probabilities of our confirmed dwarfs in each bin being scattered beyond the cut based on their measured CH_4 colours and 1σ uncertainties. We find that we would expect 8 per cent of T6–T6.5 dwarfs to be scattered out of our selection at this stage of follow-up. Following the same method for T7–T7.5 dwarfs, we find that less the 0.1 per cent will be excluded, and similarly negligible fractions for the later type bins also.

We thus find that our bias correction factors for our full sample due to our selection method are 1.03 for the T7–T7.5 and later bins, and 1.05 for our T6–T6.5 bin. We must also correct for biases inherent to any magnitude-limited survey due to preferential inclusion of unresolved binary systems and the Malmquist bias. In Burningham et al. (2010b), we derived binary correction factors of 0.97 and 0.55 based on the broadest range of likely binary fractions reported in the literature (5–45 per cent). In Pinfield et al. (2008), the Malmquist correction factor was found to be between 0.84 and 0.86. We apply these same correction factors here.

Calculating a space density from our corrected sample requires the application of some M_J-spectral type conversion to determine the volume probed for each subtype by our magnitude-limited sample. The choice of relation has a significant impact on the resulting space densities, and differences in approach to this issue can contribute significantly to differences in measured space density between different projects. In Burningham et al. (2010b), we used the M_J-spectral type relations of Liu et al. (2006). However, to take advantage of the improved sample of T dwarfs with measured parallaxes, we will instead use the polynomial relations presented by Dupuy & Liu (2012) here. Since these relations are only valid for the Cushing et al. (2011) system for the latest spectral types, we have included our T9 dwarfs in the T8–T8.5 bin. In Table 10, we provide a summary of our update to this calculation. By this method, we find that the space density of T6–T8.5 dwarfs (on the Cushing et al. 2011 system) is 3.00 ± 1.3–$5.52 \pm 2.4 \times 10^{-3}$ pc^{-3}, depending on the underlying binary fraction.

Kirkpatrick et al. (2012) also used polynomial relations to estimate the magnitudes of objects for which no trigonometric parallax is available and they applied a single 30 per cent unresolved binary correction. To allow comparison between these samples, we have carried out an additional space density calculation assuming the same binary fraction. Table 11 summarizes this calculation, from which we find a space density of $3.9 \pm 1.7 \times 10^{-3}$ pc^{-3} for T6–T8.5 dwarfs on the Cushing et al. (2011) system. This is very close to the value of $3.43 \pm 0.32 \times 10^{-3}$ pc^{-3} found by Kirkpatrick et al. (2012). The error we have assigned to Kirkpatrick value has been calculated assuming only Poisson noise in their count of each spectral subtype.

Using polynomial relations is not necessarily, however, the most appropriate way to estimate absolute magnitudes for targets of a given subtype. This is because the subtypes are not a continuous variable, but rather discrete and based on an inherently subjective spectral typing scheme. As such, polynomial fits (and their associated residuals) can mask true scatter in the M_J values of certain subtypes. We have thus performed an additional density estimate using the mean magnitudes for each spectral subtype from Dupuy & Liu (2012), and using the Cushing et al. (2011) spectral typing scheme. For the purposes of this calculation, we have also used a single binary correction factor of 30 per cent. Table 12 summarizes this calculation that we include here for illustrative purposes.

This method leads us to an estimate of $6.2 \pm 1.9 \times 10^{-3}$ pc^{-3} for the space density of T6–T8.5 dwarfs (on the system of Cushing et al. 2011). This is somewhat higher than the other methods determined (for the same binary fraction), and it is driven by the fainter absolute magnitude assigned to the coolest spectral type bin. Metchev et al. (2008) also used a mean magnitude approach for estimating their

Table 10. Summary of the updated space density calculation following the method of Burningham et al. (2010b) for our $J < 18.8$ sample of ≥T6 dwarfs. N_c refers to corrected numbers based on the sample corrections described in the text, with maximum and minimum values arising from the different possible binary corrections. The values of M_J used to calculate the distance limit and volume probed for each type were calculated using the polynomial relations in M_J versus spectral type derived by Dupuy & Liu (2012). The uncertainties in M_J reflect the rms scatter about the Dupuy & Liu (2012) polynomials. The uncertainties in the computed space densities reflect the volume uncertainty that arises from the uncertainty in M_J and Poisson noise in our sample. The minimum and maximum space densities reflect the range encompassed by likely binary fractions (see the text and Burningham et al. 2010b). The latest spectral types are on the Cushing et al. (2011) system.

Type	$T_{\rm eff}$ range	N	N_c(min)	N_c(max)	M_J(MKO)	Range (pc)	Volume (pc^3)	$\rho_{\rm min}$ (10^{-3} pc^{-3})	$\rho_{\rm max}$ (10^{-3} pc^{-3})
T6–6.5	900–1050 K	40	19.4 ± 3.1	35.6 ± 5.7	14.90 ± 0.39	60 ± 11	50 400 ± 27 100	0.39 ± 0.22	0.71 ± 0.40
T7–7.5	800–900 K	21	10.0 ± 2.2	18.5 ± 4.0	15.65 ± 0.39	43 ± 8	18 000 ± 9700	0.56 ± 0.32	1.02 ± 0.64
T8–8.5	500–800 K	17	6.7 ± 1.8	12.3 ± 3.3	16.75 ± 0.39	26 ± 5	3900 ± 2100	2.05 ± 1.21	3.79 ± 2.24

Table 11. Summary of the updated space density calculation following the method of Burningham et al. (2010b) for our $J < 18.8$ sample of ≥T6 dwarfs. N_c refers to corrected numbers based on the sample corrections described in the text, and 30 per cent binary correction as applied by Kirkpatrick et al. (2012). The values of M_J and the uncertainties are as for Table 10. The latest spectral types are on the Cushing et al. (2011) system. The uncertainties for the Kirkpatrick et al. (2012) densities estimated purely on the basis of Poisson noise on their number counts.

Type	$T_{\rm eff}$ range	N	N_c	M_J(MKO)	Range (pc)	Volume (pc^3)	ρ (10^{-3} pc^{-3})	ρ (10^{-3} pc^{-3}) Kirkpatrick et al. (2012)
T6–6.5	900–1050 K	40	25.3 ± 4.0	14.90 ± 0.39	60 ± 11	50400 ± 27100	0.50 ± 0.28	1.10 ± 0.18
T7–7.5	800–900 K	21	13.0 ± 2.8	15.65 ± 0.39	43 ± 8	18000 ± 9700	0.73 ± 0.42	0.93 ± 0.17
T8–8.5	500–800 K	17	10.5 ± 2.6	16.75 ± 0.39	26 ± 5	3900 ± 2100	2.67 ± 1.58	1.40 ± 0.21

Table 12. Summary of our space density calculation following the method of Burningham et al. (2010b) to correct biases in our $J < 18.8$ sample of ≥T6 dwarfs. N_c refers to corrected numbers based on the sample corrections described in the text, and a 30 per cent binary correction as applied by Kirkpatrick et al. (2012), and the latest spectral type bin is on the system of Cushing et al. (2011). In this case, we have used the mean absolute magnitudes of Dupuy & Liu (2012) for our M_J-spectral type conversion. We have applied these to each half subtype before combing them to arrive at space densities for full subtype bins. The uncertainties in the computed space densities reflect the volume uncertainty that arises from the uncertainty in M_J and Poisson noise in our sample.

Type	N	N_c	M_J(MKO)	Range (pc)	Volume (pc^3)	ρ (10^{-3} pc^{-3})
T6	24	15.2 ± 3.0	15.22 ± 0.15	52 ± 4	32 400 ± 6700	0.47 ± 0.12
T6.5	16	10.1 ± 2.5	15.22 ± 0.31	52 ± 7	32 400 ± 13 900	0.31 ± 0.14
T6–T6.5	40					0.78 ± 0.19
T7	14	8.7 ± 2.3	15.54 ± 0.25	45 ± 5	20 800 ± 7200	0.42 ± 0.17
T7.5	7	4.3 ± 1.6	16.05 ± 0.65	35 ± 11	10 300 ± 9200	0.42 ± 0.39
T7–T7.5	21					0.84 ± 0.43
T8	12	7.4 ± 2.1	16.39 ± 0.35	30 ± 5	6400 ± 3100	1.16 ± 0.63
T8.5	5	3.1 ± 1.4	17.81 ± 0.33	16 ± 2	900 ± 400	3.43 ± 1.77
T8–T8.5	17					4.58 ± 1.88

survey volumes, applying a mean $M_J(2{\rm MASS}) = 15.75 \pm 0.50$ to the T6–T8 bin, and deriving a space density of $4.3^{+2.9}_{-2.6} \times 10^{-3}$ pc^{-3} (for a binary fraction of ∼26 per cent). This is consistent with our value of $2.8 \pm 0.8 \times 10^{-3}$ pc^{-3} across the same spectral type range. Their slightly higher value can largely be attributed to fact that they use a single mean for the entire T6–T8 bin, which is fainter than the value we use for the most numerous T6 dwarfs. This will tend lead to an overestimate of the space density across the whole bin. This illustrates the significant impact that the assumed M_J-spectral-type relation can have on derived space densities where trigonometric parallaxes are not available for the entire sample. The uncertainties introduced by the scatter about the assumed M_J, and the systematics associated with the choice of M_J estimate relation, now significantly outweigh the random error due to our sample size.

In Fig. 16, we compare our space densities from Table 11 and that of Kirkpatrick et al. (2012), to the predictions from Monte Carlo simulations of the Galactic field population of T dwarfs assuming different forms of the IMF and brown dwarf formation history (see Deacon & Hambly 2006; Burningham et al. 2010b, for full descriptions). As in Burningham et al. (2010b) we have used the system mass function normalization of 0.0024 pc^{-3} for objects in the 0.09–0.10 $M_\odot$ range, taken from Deacon, Nelemans & Hambly (2008). For the purposes of this comparison we have transformed the space densities which are supplied from the simulations as a function of $T_{\rm eff}$, to densities as a function of spectral type using the $T_{\rm eff}$ ranges given in Table 11. These conversions are uncertain and function as a very 'broad brush' to facilitate the comparison between simulations and observation. We have also included predictions for the Chabrier (2005) log-normal system mass function, since this now appears to be the preferred function fitted to young clusters across the low-mass stellar/substellar/planetary mass regime (e.g. Bastian, Covey & Meyer 2010; Alves de Oliveira et al. 2012; Lodieu et al. 2012b, and references therein).

It is clear that the estimated space densities from both UKIDSS and *WISE* are significantly lower than predicted for an $\alpha = 0$ or log-normal mass function, coinciding best with values of $-1.0 < \alpha < -0.5$. As has been noted before (e.g. Pinfield et al. 2008; Burningham et al. 2010b), this represents a significant discrepancy

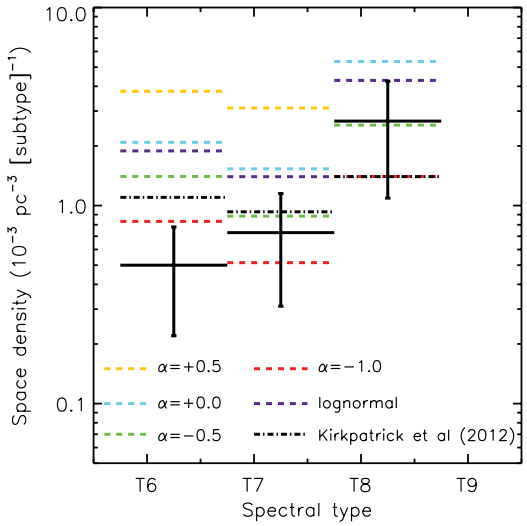

Figure 16. Computed space densities for different spectral types from Monte Carlo simulations of the field population of T dwarfs for a uniform birthrate (i.e. $\beta = 0.0$, see Deacon & Hambly 2006; Burningham et al. 2010b for full definition) and various underlying mass functions. The power-law mass functions are of the form $\psi(M) \propto M^{-\alpha}$ pc^{-3} M$_{\odot}^{-1}$, and the log-normal mass function is the Chabrier (2005) system mass function. Our observed space density is shown as solid black lines, Kirkpatrick et al. (2012) as dash–dotted black lines. Uncertainties are indicated with bars at the mid-point of each spectral type bin, and reflect volume uncertainties and Poisson counting uncertainties.

with the IMF measured in many young clusters where the mass function has been fitted with $\alpha \approx +0.6$ power laws (e.g. Barrado y Navascués et al. 2002; Lodieu et al. 2007c, 2009) or the log-normal mass function with a characteristic mass in the region of 0.2 M$_{\odot}$ that has been measured by studies using the UKIDSS Galactic Clusters Survey, amongst others (e.g. Lodieu et al. 2007a, 2009, 2011a,b, 2012b; Alves de Oliveira et al. 2012, 2013; Boudreault et al. 2012; Lodieu, Deacon & Hambly 2012a). Kirkpatrick et al. (2012) note that the ratio of stars to brown dwarfs in the field is consistent with that seen in young clusters when a universal substellar IMF is assumed (Andersen et al. 2008), and thus conclude that the underlying mass functions are the same. However, the discrepancy between the predictions based on the functional form that has been fitted to the IMF in young clusters, and observed field population should not be ignored. Assuming a 30 per cent binary fraction, both our UKIDSS T6–T8.5 space density and that of Kirkpatrick et al. (2012) are approximately half that predicted by the log-normal mass function, and corresponding to a significance of 2σ and 13σ, respectively.

The kinematics of our sample (see Section 8) imply that this discrepancy cannot be attributed to late-T dwarfs having a significantly different formation history to the rest of the Galactic disc, and we are left with two plausible options. First, errors in the evolutionary models used to estimate masses in young clusters and/or in the cooling times used to produce the Monte Carlo simulations in field could give rise to such a discrepancy. These options can be investigated by employing shifted cooling curves in the Monte Carlo simulations to investigate their impact on the predicted space densities and age profiles, and we defer further discussion of this possibility to a future work.

The second plausible origin for such a discrepancy is if the bulk of the field population formed in different environments than the nearby young clusters that have been subject to detailed study. For example, Bressert et al. (2010) have found that only 26 per cent of low-mass stars form in high-density regions, which they define as those with surface densities of young stellar objects (YSOs) $> 200\,\mathrm{pc}^{-2}$, corresponding roughly to the most dense parts of the Taurus star-forming complex. Luhman (2004) found a deficit of brown dwarfs in Taurus relative to the high densities of the Trapezium cluster, and more recent studies have further hinted at similar enrichment of the substellar component at higher densities (Andersen et al. 2011). A combination of low-density-dominated low-mass star and brown dwarf formation with a substellar IMF that declines steeply in the lowest density regions, but has the log-normal form currently preferred in higher density regions, would naturally reconcile the two conflicting views of form for the substellar IMF that we are currently presenting. Unfortunately, obtaining a statistically meaningful census of the young substellar population in the lowest density regions where Bressert et al. (2010) argue that most low-mass stars are formed (e.g. <50 YSOs pc^{-2}) is extremely challenging due to the large areas that must be surveyed and the inherently faint nature of the targets. Given the significant investment of observing time that would be required to test this hypothesis, it would make sense to first investigate the potential impact of systematic effects in the evolutionary models for both young and old objects.

10 SUMMARY

The expanded T dwarf sample presented here, along with access to the new two epoch LAS catalogue of Smith et al. (in preparation) has allowed the discovery of two new benchmark systems along with the first estimate for the wide binary companion fraction amongst late-T dwarfs. By examining the colours of the current census of late-type benchmarks, we have identified the $H - [4.5]$ and $J - W2$ as being more sensitive to metallicity than models have so far predicted, and caution that this must be considered when using these colours to estimate the relative properties of cool brown dwarfs. The expanded sample of late-T dwarfs, and the new model grids from Saumon et al. (2012) and Morley et al. (2012) also now argue against the previous conclusion of Leggett et al. (2010a) that the sample is dominated by young low-mass objects. This is supported by the kinematics of our sample.

Our updated space density for late-T dwarfs is consistent with the density reported by Kirkpatrick et al. (2012) and confirms our previous conclusion that there are far fewer late-T dwarfs than we would expect given the favoured forms for the IMF in young clusters. Whilst it is possible that this discrepancy arises from problems with either or both of the young and old evolutionary models for brown dwarfs, we also speculate that it could arise as a result of the dominant environment for low-mass star and brown dwarf formation being lower density regions than are currently probed, as suggested for low-mass stars by Bressert et al. (2010).

ACKNOWLEDGEMENTS

We thank our referee, J. Davy Kirkpatrick, for a helpful review which substantially improved the quality of this manuscript. Based on observations made under project A22TAC_96 on the Italian Telescopio Nazionale Galileo (TNG) operated on the island of La Palma by the Fundacin Galileo Galilei of the INAF (Istituto Nazionale di Astrofisica) at the Spanish Observatorio del Roque de los Muchachos of the Instituto de Astrofisica de Canarias. Based on observations obtained at the Gemini Observatory, which is operated by the Association of Universities for Research in Astronomy, Inc., under a cooperative agreement with the NSF on behalf of the Gemini partnership: the National Science Foundation (United States),

the Science and Technology Facilities Council (United Kingdom), the National Research Council (Canada), CONICYT (Chile), the Australian Research Council (Australia), Ministério da Ciência e Tecnologia (Brazil) and Ministerio de Ciencia, Tecnología e Innovación Productiva (Argentina). We would like to acknowledge the support of the Marie Curie 7th European Community Framework Programme grant no. 247593 Interpretation and Parametrization of Extremely Red COOL dwarfs (IPERCOOL) International Research Staff Exchange Scheme. ADJ is supported by a Fondecyt postdoctorado fellowship, under project number 3100098, and is also partially supported by the proyecto Basal PB06 (CATA) and the Joint Committee ESO-Government Chile. AHA thanks CNPq grant PQ306775/2009-3 and SHAO/CAS Visiting Professorship grant. CGT is supported by ARC grant DP0774000. SKL's research is supported by the Gemini Observatory. JG is supported by RoPACS, a Marie Curie Initial Training Network funded by the European Commission's Seventh Framework Programme. NL acknowledges funding from the Spanish Ministry of Science and Innovation through the Ramón y Cajal fellowship number 08-303-01-02 and the project number AYA2010-19136. This research has made use of the NASA/IPAC Infrared Science Archive, which is operated by the Jet Propulsion Laboratory, California Institute of Technology, under contract with the National Aeronautics and Space Administration. This research has made use of the SIMBAD data base, operated at CDS, Strasbourg, France, and has benefited from the SpeX Prism Spectral Libraries, maintained by Adam Burgasser at http://www.browndwarfs.org/spexprism. We wish to recognize and acknowledge the very significant cultural role and reverence that the summit of Mauna Kea has always had within the indigenous Hawaiian community. We are most fortunate to have the opportunity to conduct observations from this mountain.

REFERENCES

Abel M., Frommhold L., Li X., Hunt K. L. C., 2011, J. Chem. Phys., 115, 6805
Abel M., Frommhold L., Li X., Hunt K. L. C., 2012, J. Chem. Phys., 136, 044319
Albert L., Artigau É., Delorme P., Reylé C., Forveille T., Delfosse X., Willott C. J., 2011, AJ, 141, 203
Aldering G. et al., 2006, ApJ, 650, 510
Allard F., Homeier D., Freytag B., 2010, preprint (arXiv:1011.5405)
Alves de Oliveira C., Moraux E., Bouvier J., Bouy H., 2012, A&A, 539, A151
Alves de Oliveira C., Moraux E., Bouvier J., Duchene G., Bouy H., Maschberger T., Hudelot P., 2013, A&A, 549, A123
Andersen M., Meyer M. R., Greissl J., Aversa A., 2008, ApJ, 683, L183
Andersen M., Meyer M. R., Robberto M., Bergeron L. E., Reid N., 2011, A&A, 534, A10
Bacon R. et al., 2001, MNRAS, 326, 23
Baffa C. et al., 2001, A&A, 378, 722
Baraffe I., Chabrier G., Barman T. S., Allard F., Hauschildt P. H., 2003, A&A, 402, 701
Barrado y Navascués D., Bouvier J., Stauffer J. R., Lodieu N., McCaughrean M. J., 2002, A&A, 395, 813
Bastian N., Covey K. R., Meyer M. R., 2010, ARA&A, 48, 339
Beichman C. A., Gelino C. R., Kirkpatrick J. D., Barman T. S., Marsh K. A., Cushing M. C., Wright E. L., 2013, ApJ, 764, 101
Bertin E., Arnouts S., 1996, A&AS, 117, 393
Bochanski J. J., West A. A., Hawley S. L., Covey K. R., 2007, AJ, 133, 531
Bochanski J. J. et al., 2009, PASP, 121, 1409
Bochanski J. J., Hawley S. L., Covey K. R., West A. A., Reid I. N., Golimowski D. A., Ivezić Ž., 2010, AJ, 139, 2679
Bochanski J. J., Burgasser A. J., Simcoe R. A., West A. A., 2011, AJ, 142, 169
Boudreault S., Lodieu N., Deacon N. R., Hambly N. C., 2012, MNRAS, 426, 3419
Bressert E. et al., 2010, MNRAS, 409, L54
Burgasser A. J., 2004, ApJS, 155, 191
Burgasser A. J., McElwain M. W., Kirkpatrick J. D., Cruz K. L., Tinney C. G., Reid I. N., 2004, AJ, 127, 2856
Burgasser A. J., Geballe T. R., Leggett S. K., Kirkpatrick J. D., Golimowski D. A., 2006, ApJ, 637, 1067
Burningham B. et al., 2008, MNRAS, 391, 320
Burningham B. et al., 2009, MNRAS, 395, 1237
Burningham B. et al., 2010a, MNRAS, 404, 1952
Burningham B. et al., 2010b, MNRAS, 406, 1885
Burningham B. et al., 2011, MNRAS, 414, 3590
Burrows A., Heng K., Nampaisarn T., 2011, ApJ, 736, 47
Casagrande L., Schönrich R., Asplund M., Cassisi S., Ramírez I., Meléndez J., Bensby T., Feltzing S., 2011, A&A, 530, A138
Casali M. et al., 2007, A&A, 467, 777
Chabrier G., 2005, in Corbelli E., Palla F., Zinnecker H., eds, Astrophysics and Space Science Library, Vol. 327, The Initial Mass Function 50 Years Later. Springer, Dordrecht, p. 41
Chiu K., Fan X., Leggett S. K., Golimowski D. A., Zheng W., Geballe T. R., Schneider D. P., Brinkmann J., 2006, AJ, 131, 2722
Chiu K. et al., 2008, MNRAS, 385, L53
Cooke A., Rodgers B., 2005, in Shopbell P., Britton M., Ebert R., eds, ASP Conf. Ser. Vol. 347, Astronomical Data Analysis Software and Systems XIV. Astron. Soc. Pac., San Francisco, p. 514
Cushing M. C., Vacca W. D., Rayner J. T., 2004, PASP, 116, 362
Cushing M. C. et al., 2011, ApJ, 743, 50
Day-Jones A. C. et al., 2011, MNRAS, 410, 705
Deacon N. R., Hambly N. C., 2006, MNRAS, 371, 1722
Deacon N. R., Nelemans G., Hambly N. C., 2008, A&A, 486, 283
Deacon N. R. et al., 2012, ApJ, 757, 100
Delorme P. et al., 2008, A&A, 482, 961
Delorme P. et al., 2010, A&A, 518, A39
Dhital S., West A. A., Stassun K. G., Bochanski J. J., 2010, AJ, 139, 2566
Dupuy T. J., Liu M. C., 2012, ApJS, 201, 19
Elias J. H., Joyce R. R., Liang M., Muller G. P., Hileman E. A., George J. R., 2006, in McLean I. S., Iye M., eds, Proc. SPIE Conf. Ser. Vol. 6269, Ground-based and Airborne Instrumentation for Astronomy. SPIE, Bellingham, p. 626914
Faherty J. K., Burgasser A. J., Cruz K. L., Shara M. M., Walter F. M., Gelino C. R., 2009, AJ, 137, 1
Faherty J. K., Burgasser A. J., West A. A., Bochanski J. J., Cruz K. L., Shara M. M., Walter F. M., 2010, AJ, 139, 176
Goldman B., Marsat S., Henning T., Clemens C., Greiner J., 2010, MNRAS, 405, 1140
Gomes J. I. et al., 2013, MNRAS, 431, 2745
Hambly N. C. et al., 2008, MNRAS, 384, 637
Hodapp K. W. et al., 2003, PASP, 115, 1388
Høg E. et al., 2000, A&A, 355, L27
Irwin M. J. et al., 2004, in Quinn P. J., Bridger A., eds, Proc. SPIE Vol. 5493, Optimizing Scientific Return for Astronomy through Information Technologies. SPIE, Bellingham, p. 411
Jurić M. et al., 2008, ApJ, 673, 864
Kendall T. R. et al., 2007, A&A, 466, 1059
Kirkpatrick J. D., 2005, ARA&A, 43, 195
Kirkpatrick J. D. et al., 2011, ApJS, 197, 19
Kirkpatrick J. D. et al., 2012, ApJ, 753, 156
Knapp G. R. et al., 2004, AJ, 127, 3553
Kobayashi N. et al., 2000, in Iye M., Moorwood A. F., eds, Proc. SPIE Vol. 4008, Optical and IR Telescope Instrumentation and Detectors. SPIE, Bellingham, p. 1056
Lantz B. et al., 2004, in Mazuray L., Rogers P. J., Wartmann R., eds, Proc. SPIE Vol. 5249, Optical Design and Engineering. SPIE, Bellingham, p. 146
Lawrence A. et al., 2007, MNRAS, 379, 1599
Leggett S. K. et al., 2009, ApJ, 695, 1517
Leggett S. K. et al., 2010a, ApJ, 710, 1627

Leggett S. K., Saumon D., Burningham B., Cushing M. C., Marley M. S., Pinfield D. J., 2010b, ApJ, 720, 252
Leggett S. K., Morley C. V., Marley M. S., Saumon D., Fortney J. J., Visscher C., 2013, ApJ, 763, 130
Lepine S., Hilton E. J., Mann A. W., Wilde M., Rojas-Ayala B., Cruz K. L., Gaidos E., 2013, AJ, 145, 102
Lépine S., Shara M. M., 2005, AJ, 129, 1483
Liu M. C., Leggett S. K., Golimowski D. A., Chiu K., Fan X., Geballe T. R., Schneider D. P., Brinkmann J., 2006, ApJ, 647, 1393
Liu M. C., Leggett S. K., Chiu K., 2007, ApJ, 660, 1507
Liu M. C., Dupuy T. J., Bowler B. P., Leggett S. K., Best W. M. J., 2012, ApJ, 758, 57
Lodders K., Fegley B., 2002, Icarus, 155, 393
Lodieu N., Hambly N. C., Jameson R. F., Hodgkin S. T., Carraro G., Kendall T. R., 2007a, MNRAS, 374, 372
Lodieu N. et al., 2007b, MNRAS, 379, 1423
Lodieu N., Dobbie P. D., Deacon N. R., Hodgkin S. T., Hambly N. C., Jameson R. F., 2007c, MNRAS, 380, 712
Lodieu N., Zapatero Osorio M. R., Rebolo R., Martín E. L., Hambly N. C., 2009, A&A, 505, 1115
Lodieu N., Hambly N. C., Dobbie P. D., Cross N. J. G., Christensen L., Martin E. L., Valdivielso L., 2011a, MNRAS, 418, 2604
Lodieu N., de Wit W.-J., Carraro G., Moraux E., Bouvier J., Hambly N. C., 2011b, A&A, 532, A103
Lodieu N., Deacon N. R., Hambly N. C., 2012a, MNRAS, 422, 1495
Lodieu N., Deacon N. R., Hambly N. C., Boudreault S., 2012b, MNRAS, 426, 3403
Lodieu N. et al., 2012c, A&A, 548, A53
Looper D. L., Kirkpatrick J. D., Burgasser A. J., 2007, AJ, 134, 1162
Luhman K. L., 2004, ApJ, 617, 1216
Luhman K. L. et al., 2012, ApJ, 760, 152
Mace G. N. et al., 2013, ApJS, 205, 6
Manchado A. et al., 1998, in Fowler A. M., ed., Proc. SPIE Vol. 3354, Infrared Astronomical Instrumentation. SPIE, Bellingham, p. 448
Mann A. W., Brewer J. M., Gaidos E., Lepine S., Hilton E. J., 2013, AJ, 145, 52
Marocco F. et al., 2010, A&A, 524, A38
Masana E., Jordi C., Ribas I., 2006, A&A, 450, 735
Metchev S. A., Kirkpatrick J. D., Berriman G. B., Looper D., 2008, ApJ, 676, 1281
Molinari E., Conconi P., Pucillo M., 1997, Mem. Soc. Astron. Ital., 68, 231
Morley C. V., Fortney J. J., Marley M. S., Visscher C., Saumon D., Leggett S. K., 2012, ApJ, 756, 172
Murray D. N. et al., 2011, MNRAS, 414, 575
Neves V. et al., 2012, A&A, 538, A25
Oke J. B., 1990, AJ, 99, 1621
Perryman M. A. C. et al., 1997, A&A, 323, L49
Pinfield D. J., Jones H. R. A., Lucas P. W., Kendall T. R., Folkes S. L., Day-Jones A. C., Chappelle R. J., Steele I. A., 2006, MNRAS, 368, 1281
Pinfield D. J. et al., 2008, MNRAS, 390, 304
Pinfield D. J. et al., 2012, MNRAS, 422, 1922
Roche P. F. et al., 2003, in Iye M., Moorwood A. F. M., eds, Proc. SPIE Vol. 4841, Instrument Design and Performance for Optical/Infrared Ground-based Telescopes. SPIE, Bellingham, p. 901
Rojas-Ayala B., Covey K. R., Muirhead P. S., Lloyd J. P., 2012, ApJ, 748, 93
Saumon D., Marley M. S., 2008, ApJ, 689, 1327
Saumon D., Marley M. S., Cushing M. C., Leggett S. K., Roellig T. L., Lodders K., Freedman R. S., 2006, ApJ, 647, 552
Saumon D., Marley M. S., Abel M., Frommhold L., Freedman R. S., 2012, ApJ, 750, 74
Schlaufman K. C., Laughlin G., 2010, A&A, 519, A105
Scholz R., 2010, A&A, 515, 92
Scholz R.-D., Bihain G., Schnurr O., Storm J., 2012, A&A, 541, A163
Simcoe R. A. et al., 2008, in McLean I. S., Casali M. M., eds, Proc. SPIE Vol. 7014, Ground-based and Airborne Instrumentation for Astronomy II. SPIE, Bellingham, p. 70140U
Simcoe R. A. et al., 2010, in McLean I. S., Ramsay S. K., Takami H., eds, Proc. SPIE Vol. 7735, Ground-based and Airborne Instrumentation for Astronomy III. SPIE, Bellingham, p. 773514
Smart R. L. et al., 2010, A&A, 511, A30
Stoughton C. et al., 2002, AJ, 123, 485
Tinney C. G., Burgasser A. J., Kirkpatrick J. D., McElwain M. W., 2005, AJ, 130, 2326
Tokunaga A. T., Simons D. A., Vacca W. D., 2002, PASP, 114, 180
Tsvetanov Z. I. et al., 2000, ApJ, 531, L61
Vacca W. D., Cushing M. C., Rayner J. T., 2003, PASP, 115, 389
van Leeuwen F., 2007, A&A, 474, 653
Vernet J. et al., 2011, A&A, 536, A105
West A. A., Hawley S. L., Bochanski J. J., Covey K. R., Reid I. N., Dhital S., Hilton E. J., Masuda M., 2008, AJ, 135, 785
Wright E. L. et al., 2010, AJ, 140, 1868
Yurchenko S. N., Barber R. J., Tennyson J., 2011, MNRAS, 413, 1828
Zacharias N., Monet D. G., Levine S. E., Urban S. E., Gaume R., Wycoff G. L., 2004, BAAS, 36, 1418

APPENDIX A: SQL DATABASE QUERIES USED FOR INITIAL CANDIDATE SELECTION

The following code listings give the SQL code we used to query the WSA for our candidates. These include a cross-match against SDSS DR7. To access SDSS DR8 sky not covered by SDSS DR7 we independently cross-matched candidate lists that had passed our NIR colour cuts against SDSS DR8. Our final $J - K < 0.1$ colour cut was applied to the resulting candidate lists.

Query 1. The SQL query used to select candidates via our *YJH* channel in the case where they have been detected in SDSS.

```
SELECT las.ra,las.dec,ymj_1Pnt,ymj_1PntErr,j_1mhPnt,
     j_1mhPntErr,yAperMag3,yAperMag3Err,j_1AperMag3,
     j_1AperMag3Err,hAperMag3, hAperMag3Err,kAperMag3,
     kAperMag3Err,psfMag_u,psfMagErr_u,psfMag_g,
     psfMagErr_g,psfMag_r,psfMagErr_r,psfMag_i,
     psfMagErr_i,psfMag_z,psfMagErr_z,(psfMag_i-
     psfMag_z),(psfMag_z - j_1AperMag3)
FROM   lasSource AS las, BestDR7..PhotoObj AS dr7,
     lasSourceXDR7PhotoObj AS x
WHERE
masterObjID=las.sourceID AND slaveObjID=dr7.ObjID AND
     distanceMins <0.033333 AND
 sdssPrimary=1 AND distanceMins IN (
SELECT MIN(distanceMins)
FROM lasSourceXDR7PhotoObj
WHERE masterObjID=x.masterObjID AND sdssPrimary=1) AND
/*     Good sdss detections */
     (psfMagErr_i < 0.5 or psfMagErr_z < 0.5) AND
/*     Colour cuts for mid-T & later: */
     j_1mhPnt < 0.1        AND
     ((psfMag_z - j_1AperMag3) > 2.5 or
     (psfMag_i - psfMag_z > 1.5)) AND
/*     Unduplicated or primary duplicates only: */
     (priOrSec = 0 OR priOrSec = frameSetID) AND
/*     Generally good quality: */
     yppErrBits   < 256 AND
     j_1ppErrBits < 256 AND
     hppErrBits   < 256 AND

/*     Point-like morphological classification: */
     mergedClass BETWEEN -3.0 and -0.5 and
     mergedClassStat BETWEEN -3.0 AND +3.0 AND
/*     Reasonably circular images: */
     yEll < 0.45 AND j_1Ell < 0.45 and
/*     YJ measured to 3 sigma and */
     yAperMag3Err   < 0.30 AND
     j_1AperMag3Err < 0.30 AND
     yAperMag3 > 14.5 AND
     j_1AperMag3 > 14.5 AND
     hAperMag3 > 14.5
ORDER BY las.ra
```

Query 2. The SQL query used to select candidates via our *YJH* channel in the case where they have not been detected in SDSS.

```
SELECTra,dec,ymj_1Pnt,ymj_1PntErr,j_1mhPnt,j_1mhPntErr
    , yAperMag3,yAperMag3Err,j_1AperMag3,
    j_1AperMag3Err,hAperMag3, hAperMag3Err,kAperMag3,
    kAperMag3Err
FROM   lasSource
WHERE
/*      Colour cuts for mid-T & later: */
       j_1mhPnt < 0.1          AND
/*      Unduplicated or primary duplicates only: */
       (priOrSec = 0 OR priOrSec = frameSetID) AND
/*      Generally good quality: */
       yppErrBits   < 256 AND
       j_1ppErrBits < 256 AND
       hppErrBits   < 256 AND
/*      Source not detected above 2sigma in SDSS-DR7 i'
      or z' within 2 arcsec: */
       sourceID NOT IN (
       SELECT masterObjID
       FROM   lasSourceXDR7PhotoObj AS x,
              BestDR7..PhotoObj     AS p
       WHERE  p.objID = x.slaveObjID      AND
              (psfMagErr_i < 0.5 OR psfMagErr_z < 0.5)
                  AND
              x.distanceMins < 2.0/60.0
       ) AND
/*      Use only frame sets overlapping with SDSS-DR7:
    */
       frameSetID IN (
       SELECT DISTINCT(frameSetID)
       FROM   lasSource              AS s,
              lasSourceXDR7PhotoObj AS x
       WHERE  s.sourceID = x.masterObjID
       ) AND
/*      Point-like morphological classification: */
       mergedClass BETWEEN -3.0 and -0.5 and
       mergedClassStat BETWEEN -3.0 AND +3.0 AND
/*      Reasonably circular images: */
       yEll < 0.45 AND j_1Ell < 0.45 and
/*      YJ measured to 3 sigma and */
       yAperMag3Err   < 0.30 AND
       j_1AperMag3Err < 0.30 AND
       yAperMag3 > 14.5 AND
       j_1AperMag3 > 14.5 AND
       hAperMag3 > 14.5
ORDER BY ra
```

Query 3. The SQL query used to select candidates via our *YJ*-only channel in the case where they have been detected in SDSS.

```
SELECT las.ra,las.dec,ymj_1Pnt,ymj_1PntErr,j_1mhPnt,
    j_1mhPntErr,yAperMag3,yAperMag3Err,j_1AperMag3,
    j_1AperMag3Err,hAperMag3, hAperMag3Err,kAperMag3,
    kAperMag3Err,psfMag_u,psfMagErr_u,psfMag_g,
    psfMagErr_g,psfMag_r,psfMagErr_r,psfMag_i,
    psfMagErr_i,psfMag_z,psfMagErr_z,(psfMag_i-
    psfMag_z),(psfMag_z - j_1AperMag3)
FROM   lasSource AS las, BestDR7..PhotoObj AS dr7,
    lasSourceXDR7PhotoObj AS x
WHERE
masterObjID=las.sourceID AND slaveObjID=dr7.ObjID AND
    distanceMins<0.033333 AND
 sdssPrimary=1 AND distanceMins IN (
SELECT MIN(distanceMins)
FROM lasSourceXDR7PhotoObj
WHERE masterObjID=x.masterObjID AND sdssPrimary=1) AND
/*     Good sdss detections  */
       (psfMagErr_i < 0.5 or psfMagErr_z < 0.5) AND
/*     Colour cuts for mid-T & later: */
       ((psfMag_z - j_1AperMag3) > 2.5 or
       (psfMag_i - psfMag_z > 1.5)) AND
/*  H and K dropout: */
  hAPerMag3Err < 0 AND kAperMag3Err < 0 AND
  hAperMag3 < 0 AND kAperMag3 < 0 AND
/*      Unduplicated or primary duplicates only: */
       (priOrSec = 0 OR priOrSec = frameSetID) AND
/*      Generally good quality: */
       yppErrBits   < 256 AND
       j_1ppErrBits < 256 AND
/*      Point-like morphological classification: */
       mergedClass BETWEEN -3.0 and -0.5 and
       mergedClassStat BETWEEN -3.0 AND +3.0 AND
/*      Reasonably circular images: */
       yEll < 0.45 AND j_1Ell < 0.45 and
/*      YJ measured to 3 sigma and */
       yAperMag3Err   < 0.30 AND
       j_1AperMag3Err < 0.30 AND
       yAperMag3 > 14.5 AND
       j_1AperMag3 > 14.5
```

Query 4. The SQL query used to select candidates via our *YJ*-only channel in the case where they have not been detected in SDSS.

```
SELECT  s.ra,s.dec,s.ymj_1Pnt,s.ymj_1PntErr,s.j_1mhPnt
    ,s.j_1mhPntErr,
        s.yAperMag3,s.yAperMag3Err,s.j_1AperMag3,s.
            j_1AperMag3Err,my.mjdObs - mj.mjdObs, s.
            mergedClass
  /* Only frames with full coverage */
FROM   lasYJHKSource As s, lasYJHKmergeLog AS l,
    Multiframe AS my, Multiframe AS mj
WHERE
/*      Colour cuts for mid-T & later or bright enough
     that its not M dwarf: */
       (s.ymj_1Pnt > 0.5   OR s.j_1AperMag3 < 18.5)
           AND
/*      Unduplicated or primary duplicates only: */
       (s.priOrSec = 0 OR s.priOrSec = s.frameSetID)
           AND
/*      Generally good quality: */
       s.yppErrBits   < 256 AND
       s.j_1ppErrBits < 256 AND
  s.frameSetID = l.frameSetID AND
/*  Pick out the YJHK frames to get the mjds*/
    l.ymfID = my.multiframeID AND
    l.j_1mfID = mj.multiframeID AND
/*      Source not detected above 2sigma in SDSS-DR7 i'
     or z' within 2 arcsec: */
       sourceID NOT IN (
       SELECT masterObjID
       FROM   lasSourceXDR7PhotoObj AS x,
              BestDR7..PhotoObj     AS p
       WHERE  p.objID = x.slaveObjID      AND
              (psfMagErr_i < 0.5 OR psfMagErr_z < 0.5)
                  AND
              x.distanceMins < 1.0/60.0
       ) AND
/*      Use only frame sets overlapping with SDSS-DR7:
    */
       s.frameSetID IN (
       SELECT DISTINCT(s.frameSetID)
       FROM   lasSource              AS n,
              lasSourceXDR7PhotoObj AS x
       WHERE  n.sourceID = x.masterObjID
       ) AND
/*      Star-like morphological classification: */
       s.mergedClass BETWEEN -2.0 and -1.0 AND
       s.mergedClassStat BETWEEN -3.0 AND +3.0 AND
/*      Reasonably circular images: */
       s.yEll < 0.45 AND s.j_1Ell < 0.45 AND
/*      IR pairs within 0.75 arcsec: */
  (((s.yXi  BETWEEN -0.75 AND +0.75) AND
  (s.yEta   BETWEEN -0.75 AND +0.75) AND
       (s.j_1Xi  BETWEEN -0.75 AND +0.75) AND
       (s.j_1Eta BETWEEN -0.75 AND +0.75)) OR
/*  Or MJD of OBS separated by more than 1 days */
  ((my.mjdObs - mj.mjdObs) > 1 or (mj.mjdObs - my.
      mjdObs) > 1)) AND
/*  YJ measured to 3: */
       s.yAperMag3Err   < 0.30 AND s.yAperMag3Err   >
           0 AND
       s.j_1AperMag3Err < 0.30 AND s.j_1AperMag3Err >
           0 AND
/*  H and K dropout: */
  s.hAPerMag3Err < 0 AND s.kAperMag3Err < 0 AND
  s.hAperMag3 < 0 AND s.kAperMag3 < 0 AND
/*  J brighter than 19.5 */
  s.j_1AperMag3 < 19.30
ORDER BY ra
```

APPENDIX B: SUMMARY OF PHOTOMETRIC OBSERVATIONS

Table B1. Summary of broad-band photometric observations.

Object	Filter	Instrument	UT date	Programme ID	$T_{\rm int}$ (s)
ULAS J0128+0633	z'	ACAM	2011-01-08	W/10B/P16	1800
ULAS J0130+0804	MKO *Y*	WFCAM	2010-11-22	U/10B/8	280
	MKO *J*	WFCAM	2010-11-22	U/10B/8	120
	MKO *H*	WFCAM	2010-11-22	U/10B/8	1000
	MKO *K*	WFCAM	2010-11-22	U/10B/8	1000
ULAS J0226+0702	MKO *Y*	WFCAM	2010-11-22	U/10B/8	280
	MKO *J*	WFCAM	2010-11-22	U/10B/8	120
	MKO *H*	WFCAM	2010-11-22	U/10B/8	1000
	MKO *K*	WFCAM	2010-11-22	U/10B/8	1000
ULAS J0245+0653	MKO *J*	WFCAM	2009-12-16	U/09B/7	120
ULAS J0255+0616	MKO *J*	WFCAM	2009-12-16	U/09B/7	120
	MKO *H*	WFCAM	2009-12-16	U/09B/7	1000
ULAS J0329+0430	MKO *Y*	WFCAM	2010-11-24	U/10B/8	280
	MKO *J*	WFCAM	2010-11-24	U/10B/8	120
	MKO *H*	WFCAM	2010-11-24	U/10B/8	1000
	MKO *K*	WFCAM	2010-11-24	U/10B/8	1000
ULAS J0746+2355	z'	DOLORES	2010-12-27	A22TAC_96	1200
	H	LIRIS	2011-01-09	W/10B/P16	3000
	CH_4l	LIRIS	2011-01-09	W/10B/P16	3000
ULAS J0747+2455	MKO *Y*	WFCAM	2010-04-19	U/10A/6	280
	MKO *J*	WFCAM	2010-04-19	U/10A/6	120
	MKO *H*	WFCAM	2010-04-19	U/10A/6	1000
	MKO *K*	WFCAM	2010-04-19	U/10A/6	1000
ULAS J0758+2225	MKO *J*	WFCAM	2009-12-16	U/09B/7	120
	MKO *H*	WFCAM	2009-12-16	U/09B/7	1000
ULAS J0759+1855	z'	DOLORES	2010-12-18	A22TAC_96	1200
ULAS J0800+1908	z'	DOLORES	2010-12-28	A22TAC_96	1200
ULAS J0809+2126	MKO *J*	WFCAM	2010-01-08	U/09B/7	120
	MKO *H*	WFCAM	2010-01-08	U/09B/7	1000
ULAS J0814+2452	z'	DOLORES	2010-12-28	A22TAC_96	1200
	H	LIRIS	2011-01-09	W/2010B/P16	740
	CH_4l	LIRIS	2011-01-09	W/2010B/P16	740
ULAS J0815+2711	MKO *J*	WFCAM	2010-01-10	U/09B/7	120
	MKO *H*	WFCAM	2010-01-10	U/09B/7	1000
ULAS J0821+2509	MKO *J*	WFCAM	2010-01-11	U/09B/7	120
	MKO *H*	WFCAM	2010-01-11	U/09B/7	1000
ULAS J0847+0350	z'	ACAM	2011-01-12	W/10B/P16	1200
	MKO *Y*	WFCAM	2010-11-22	U/10B/8	280
	MKO *J*	WFCAM	2010-11-22	U/10B/8	120
	MKO *H*	WFCAM	2010-11-22	U/10B/8	1000
	MKO *K*	WFCAM	2010-11-22	U/10B/8	1000
ULAS J0927+3413	z'	DOLORES	2011-05-11	A23TAC_28	1200
ULAS J0929+0409	MKO *Y*	WFCAM	2010-11-22	U/10B/8	280
	MKO *J*	WFCAM	2010-11-22	U/10B/8	120
	MKO *H*	WFCAM	2010-11-22	U/10B/8	1000
	MKO *K*	WFCAM	2010-11-22	U/10B/8	1000
ULAS J0950+0117	MKO *Y*	WFCAM	2010-01-08	U/09B/7	280
	MKO *J*	WFCAM	2009-12-16	U/09B/7	120
	MKO *H*	WFCAM	2009-12-16	U/09B/7	1000
	MKO *K*	WFCAM	2010-01-08	U/09B/7	1000
ULAS J0954+0623	MKO *Y*	WFCAM	2010-11-23	U/10B/8	280
	MKO *J*	WFCAM	2010-11-23	U/10B/8	120
	MKO *H*	WFCAM	2010-11-23	U/10B/8	1000
	MKO *K*	WFCAM	2010-11-23	U/10B/8	1000
ULAS J1021+0544	MKO *Y*	WFCAM	2010-11-25	U/10B/8	280
	MKO *J*	WFCAM	2010-11-25	U/10B/8	120
	MKO *H*	WFCAM	2010-11-25	U/10B/8	1000
	MKO *K*	WFCAM	2010-11-25	U/10B/8	1000

Table B1 – *continued*

Object	Filter	Instrument	UT date	Programme ID	$T_{\rm int}$ (s)
ULAS J1023+0447	z'	DOLORES	2010-12-28	A22TAC_96	900
	MKO *Y*	WFCAM	2010-11-26	U/10B/8	280
	MKO *J*	WFCAM	2010-11-26	U/10B/8	120
	H	LIRIS	2011-01-09	W/2010B/P16	900
	CH_4l	LIRIS	2011-01-09	W/2010B/P16	900
	MKO *H*	WFCAM	2010-11-26	U/10B/8	1000
	MKO *K*	WFCAM	2010-11-26	U/10B/8	1000
ULAS J1029+0935	MKO *Y*	WFCAM	2010-11-23	U/10B/8	280
	MKO *J*	WFCAM	2010-11-23	U/10B/8	120
	MKO *H*	WFCAM	2010-11-23	U/10B/8	1000
	MKO *K*	WFCAM	2010-11-23	U/10B/8	1000
ULAS J1043+1048	MKO *Y*	WFCAM	2010-12-06	U/10B/8	280
	MKO *J*	WFCAM	2010-12-06	U/10B/8	120
	MKO *H*	WFCAM	2010-12-06	U/10B/8	1000
	MKO *K*	WFCAM	2010-12-06	U/10B/8	1000
ULAS J1051−0154	MKO *Y*	WFCAM	2010-12-06	U/10B/8	280
	MKO *J*	WFCAM	2010-12-06	U/10B/8	120
	MKO *H*	WFCAM	2010-12-06	U/10B/8	1000
	MKO *K*	WFCAM	2010-12-06	U/10B/8	1000
ULAS J1137+1126	z'	DOLORES	2011-05-08	A23TAC_28	900
ULAS J1204−0150	MKO *J*	UFTI	2009-01-25	U/08B/15	300
	MKO *H*	UFTI	2009-01-25	U/08B/15	1800
ULAS J1206+1018	MKO *J*	WFCAM	2009-07-14	U/09A/1	120
	MKO *H*	WFCAM	2009-07-14	U/09A/1	1000
ULAS J1212+1010	MKO *J*	WFCAM	2009-07-13	U/09A/1	120
	MKO *H*	WFCAM	2009-07-13	U/09A/1	1000
ULAS J1258+0307	MKO *J*	WFCAM	2010-04-20	U/10A/6	120
	MKO *H*	WFCAM	2010-04-20	U/10A/6	1000
ULAS J1302+1434	z'	DOLORES	2011-07-07	A23TAC_28	1200
	MKO *J*	WFCAM	2009-07-12	U/09A/1	120
	MKO *H*	WFCAM	2009-07-12	U/09A/1	1000
ULAS J1335+1506	MKO *Y*	UFTI	2009-01-11	U/08B/15	540
	MKO *J*	UFTI	2009-01-11	U/08B/15	300
	MKO *H*	UFTI	2009-01-11	U/08B/15	1800
ULAS J1338−0142	MKO *Y*	WFCAM	2010-05-13	U/10A/6	280
	MKO *J*	WFCAM	2010-05-13	U/10A/6	120
	MKO *H*	WFCAM	2010-05-13	U/10A/6	1000
	MKO *K*	WFCAM	2010-05-13	U/10A/6	1000
ULAS J1339−0056	MKO *Y*	WFCAM	2010-05-12	U/10A/6	280
	MKO *J*	WFCAM	2010-05-12	U/10A/6	120
	MKO *H*	WFCAM	2010-05-12	U/10A/6	1000
	MKO *K*	WFCAM	2010-05-12	U/10A/6	1000
ULAS J1421+0136	MKO *J*	WFCAM	2009-07-12	U/09A/1	120
	MKO *H*	WFCAM	2009-07-12	U/09A/1	1000
ULAS J1425+0451	z'	DOLORES	2011-05-12	A23TAC_28	1200
ULAS J1516+0110	MKO *J*	WFCAM	2010-04-20	U/10A/6	120
	MKO *H*	WFCAM	2010-04-20	U/10A/6	1000
ULAS J1534+0556	z'	DOLORES	2011-05-12	A23TAC_28	1800
ULAS J1549+2621	MKO *J*	WFCAM	2010-05-09	U/10A/6	120
	MKO *H*	WFCAM	2010-05-09	U/10A/6	1000
ULAS J1601+2646	z'	DOLORES	2011-05-14	A23TAC_28	1650
	MKO *Y*	WFCAM	2010-05-15	U/10A/6	280
	MKO *J*	WFCAM	2010-05-15	U/10A/6	120
	MKO *H*	WFCAM	2010-05-15	U/10A/6	1000
	MKO *K*	WFCAM	2010-05-15	U/10A/6	1000
ULAS J1614+2442	z'	DOLORES	2011-05-09	A23TAC_28	1200
ULAS J1619+2358	MKO *J*	WFCAM	2010-05-11	U/10A/6	120
	MKO *H*	WFCAM	2010-05-11	U/10A/6	1000
ULAS J1619+3007	MKO *J*	WFCAM	2010-05-12	U/10A/6	120
	MKO *H*	WFCAM	2010-05-12	U/10A/6	1000
ULAS J1626+2524	MKO *J*	WFCAM	2010-06-13	U/10A/6	120
	MKO *H*	WFCAM	2010-06-13	U/10A/6	1000
ULAS J2116−0101	z'	DOLORES	2011-05-11	A23TAC_28	900

Table B1 – *continued*

Object	Filter	Instrument	UT date	Programme ID	T_{int} (s)
ULAS J2237+0642	MKO *Y*	WFCAM	2010-07-11	U/10B/8	280
	MKO *J*	WFCAM	2010-11-22	U/10B/8	260
	MKO *H*	WFCAM	2010-11-22	U/10B/8	2000
	MKO *K*	WFCAM	2010-11-03	U/10B/8	2000
ULAS J2300+0703	z'	DOLORES	2011-07-08	A23TAC_28	900
	MKO *Y*	WFCAM	2009-07-14	U/09A/1	120
	MKO *J*	WFCAM	2009-07-14	U/09A/1	120
	MKO *H*	WFCAM	2009-07-14	U/09A/1	400
	MKO *K*	WFCAM	2009-07-14	U/09A/1	400
ULAS J2318+0433	z'	DOLORES	2011-11-16	A24TAC_49	900
ULAS J2326+0509	z'	DOLORES	2012-01-13	A24TAC_49	900
ULAS J2331+0426	z'	DOLORES	2011-11-16	A24TAC_49	900
ULAS J2342+0856	MKO *Y*	WFCAM	2010-11-25	U/10B/8	280
	MKO *J*	WFCAM	2010-11-25	U/10B/8	120
	MKO *H*	WFCAM	2010-11-25	U/10B/8	1000
	MKO *K*	WFCAM	2010-11-25	U/10B/8	1000
ULAS J2357+0132	z'	DOLORES	2011-07-08	A23TAC_28	900
	MKO *Y*	WFCAM	2010-11-22	U/10B/8	280
	MKO *J*	WFCAM	2010-11-22	U/10B/8	120
	MKO *H*	WFCAM	2010-11-22	U/10B/8	1000
	MKO *K*	WFCAM	2010-11-22	U/10B/8	1000

Table B2. Summary of methane photometric observations using the TNG. T_{int} gives the integration time for each co-add, N_{coadd} is the number of co-added images at each dither point, N_{dither} is the number of dither points in the mosaic.

Name	TNG programme	UT date	T_{int} (s)	N_{coadds}	N_{dither}
ULAS J0007+0112	A24TAC_49	2011-10-27	30.0	1	30
ULAS J0127+1539	A24TAC_49	2011-11-19	20.0	2	30
ULAS J0128+0633	A22TAC_96	2010-11-06	20.0	3	30
ULAS J0130+0804	A22TAC_96	2010-12-25	30.0	1	30
ULAS J0133+0231	A24TAC_49	2011-11-18	20.0	2	30
ULAS J0139+1503	A24TAC_49	2011-10-27	45.0	1	30
ULAS J0200+0908	A24TAC_49	2011-10-28	30.0	1	30
ULAS J0745+2332	A24TAC_49	2011-10-28	60.0	1	30
ULAS J0759+1855	A24TAC_49	2011-10-27	60.0	1	30
ULAS J0811+2529	A22TAC_96	2010-12-27	30.0	1	30
ULAS J0847+0350	A23TAC_28	2011-05-07	30.0	1	30
ULAS J0926+0402	A25TAC_32	2012-04-29	30.0	4	10
ULAS J0927+3413	A23TAC_28	2011-05-12	30.0	2	30
ULAS J0929+0409	A23TAC_28	2011-05-07	30.0	1	30
ULAS J0954+0623	A23TAC_28	2011-05-09	30.0	1	30
ULAS J1021+0544	A24TAC_49	2012-01-16	30.0	4	10
ULAS J1029+0935	A23TAC_28	2011-05-09	30.0	1	30
ULAS J1042+1212	A24TAC_49	2012-01-16	30.0	4	10
ULAS J1043+1048	A23TAC_28	2011-05-09	20.0	2	30
ULAS J1051−0154	A23TAC_28	2011-05-10	30.0	1	30
ULAS J1053+0157	A24TAC_49	2012-01-16	30.0	4	10
ULAS J1137+1126	A23TAC_28	2011-05-10	20.0	2	30
ULAS J1152+0359	A22TAC_96	2010-12-26	30.0	1	30
ULAS J1152+1134	A24TAC_49	2012-01-17	30.0	4	10
ULAS J1223-0131	A25TAC_32	2012-04-29	30.0	4	10
ULAS J1228+0407	A23TAC_28	2011-05-11	30.0	1	30
ULAS J1254+1222	A24TAC_49	2012-01-14	30.0	4	10
ULAS J1259+2933	A24TAC_49	2012-02-01	30.0	4	10
ULAS J1302+1434	A24TAC_49	2012-01-16	30.0	4	10
ULAS J1335+1506	A23TAC_28	2011-05-10	30.0	1	30
ULAS J1417+1330	A23TAC_28	2011-05-07	30.0	1	30
ULAS J1425+0451	A23TAC_28	2011-05-13	30.0	2	30
ULAS J1449+1147	A23TAC_28	2011-05-07	30.0	1	30
ULAS J1516+0110	A23TAC_28	2011-07-09	30.0	1	30

Table B2 – *continued*

Name	TNG programme	UT date	T_{int} (s)	N_{coadds}	N_{dither}
ULAS J1534+0556	A23TAC_28	2011-05-13	30.0	2	30
ULAS J1549+2621	A23TAC_28	2011-07-10	30.0	1	30
ULAS J1614+2442	A23TAC_28	2011-05-10	30.0	1	30
ULAS J1617+2350	A23TAC_28	2011-05-07	30.0	1	30
ULAS J1619+2358	A23TAC_28	2011-07-11	30.0	2	30
ULAS J1619+3007	A23TAC_28	2011-05-08	30.0	2	30
ULAS J2116−0101	A24TAC_49	2011-10-26	45.0	1	30
ULAS J2300+0703	A23TAC_28	2011-07-09	30.0	1	30
ULAS J2315+0344	A24TAC_49	2011-10-27	60.0	1	30
ULAS J2318+0433	A24TAC_49	2012-01-16	30.0	4	10
ULAS J2326+0201	A24TAC_49	2011-10-27	45.0	1	30
ULAS J2326+0509	A24TAC_49	2012-01-16	30.0	4	10
ULAS J2352+1244	A24TAC_49	2011-10-28	30.0	1	30

APPENDIX C: SUMMARY OF SPECTROSCOPIC OBSERVATIONS

Table C1. Dates, instruments and programme numbers for spectra obtained for this work.

Target	Instrument	UT date	Programme ID
ULAS J0007+0112	GNIRS	2011-11-14	GN-2011B-Q-5
ULAS J0127+1539	GNIRS	2011-12-31	GN-2011B-Q-43
ULAS J0128+0633	GNIRS	2010-12-15	GN-2010B-Q-41
ULAS J0130+0804	GNIRS	2011-10-15	GN-2011B-Q-5
ULAS J0133+0231	GNIRS	2011-12-17	GN-2011B-Q-43
ULAS J0139+1503	GNIRS	2011-11-24	GN-2011B-Q-43
ULAS J0200+0908	GNIRS	2011-11-26	GN-2011B-Q-43
ULAS J0226+0702	GNIRS	2011-10-15	GN-2011B-Q-5
ULAS J0245+0653	IRCS	2009-12-30	o09164
ULAS J0255+0616	XSHOOTER	2010-12-01	086.C-0450(A)
ULAS J0329+0430	NIRI	2009-11-03	GN-2009B-Q-62
ULAS J0745+2332	GNIRS	2011-11-22	GN-2011B-Q-43
ULAS J0746+2355	GNIRS	2011-04-23	GN-2011A-Q-73
ULAS J0747+2455	IRCS	2009-12-30	o09164
ULAS J0758+2225	IRCS	2009-12-31	o09164
ULAS J0759+1855	GNIRS	2011-11-25	GN-2011B-Q-5
ULAS J0809+2126	IRCS	2009-12-30	o09164
ULAS J0811+2529	GNIRS	2010-12-30	GN-2010B-Q-41
ULAS J0814+2452	GNIRS	2011-04-19	GN-2011A-Q-73
ULAS J0815+2711	IRCS	2009-12-30	o09164
ULAS J0819+2103	NIRI	2009-11-01	GN-2009B-Q-62
ULAS J0821+2509	NIRI	2009-12-31	GN-2009B-Q-62
ULAS J0926+0402	FIRE	2012-05-09	
ULAS J0927+2524	GNIRS	2011-06-16	GN-2011A-Q-73
ULAS J0929+0409	IRCS	2011-01-24	o10148
ULAS J0932+3102	NIRI	2009-12-31	GN-2009B-Q-62
ULAS J0950+0117	IRCS	2009-05-07	o09118
ULAS J0950+0117	NIRI(H)	2009-12-08	GN-2009B-Q-62
ULAS J0950+0117	NIRI(K)	2009-12-30	GN-2009B-Q-62
ULAS J0954+2452	FIRE	2012-05-09	
ULAS J1021+0544	IRCS	2011-01-23	o10148
ULAS J1023+0447	GNIRS	2011-06-12	GN-2011A-Q-73
ULAS J1029+0935	IRCS	2011-01-23	o10148
ULAS J1042+1212	GNIRS	2012-03-05	GN-2012A-Q-84
ULAS J1043+1048	GNIRS	2011-06-17	GN-2011A-Q-73
ULAS J1051+0154	IRCS	2011-01-24	o10148
ULAS J1053+0157	FIRE	2012-05-09	
ULAS J1111+0518	FIRE	2012-05-09	
ULAS J1152+0359	IRCS	2011-01-24	o10148
ULAS J1152+1134	GNIRS	2012-06-06	GN-2012A-Q-84

Table C1 – *continued*

Target	Instrument	UT Date	Programme ID
ULAS J1155+0445	NIRI	2009-12-31	GN-2009B-Q-62
ULAS J1204+0150	NIRI	2009-04-16	GN-2009A-Q-16
ULAS J1206+1018	NIRI	2010-02-06	GN-2010A-Q-44
ULAS J1212+1010	NIRI	2010-01-28	GN-2009B-Q-62
ULAS J1223−0131	FIRE	2012-05-09	
ULAS J1228+0407	FIRE	2012-05-09	
ULAS J1258+0307	IRCS	2010-04-05	o10121
ULAS J1259+2933	GNIRS	2012-04-20	GN-2012A-Q-84
ULAS J1302+1434	FIRE	2012-05-09	
ULAS J1335+1506	IRCS	2009-05-06	o09118
ULAS J1338−0142	NIRI	2010-05-01	GN-2010A-Q-44
ULAS J1339−0056	IRCS	2010-04-05	o10121
ULAS J1339+0104	IRCS	2010-04-05	o10121
ULAS J1417+1330	GNIRS	2011-05-16	GN-2011A-Q-73
ULAS J1421+0136	NIRI	2010-01-28	GN-2009B-Q-62
ULAS J1425+0451	GNIRS	2011-07-09	GN-2011A-Q-73
ULAS J1449+1147	GNIRS	2011-05-15	GN-2011A-Q-73
ULAS J1516+0110	IRCS	2010-04-06	o10121
ULAS J1517+0529	GNIRS	2011-08-13	GN-2011B-Q-5
ULAS J1534+0556	GNIRS	2011-07-09	GN-2011A-Q-73
ULAS J1536+0155	IRCS	2010-04-05	o10121
ULAS J1549+2621	IRCS	2010-04-06	o10121
ULAS J1601+2646	GNIRS	2011-03-17	GN-2011A-Q-73
ULAS J1614+2442	GNIRS	2011-07-10	GN-2011A-Q-73
ULAS J1617+2350	GNIRS	2011-05-15	GN-2011A-Q-73
ULAS J1619+2358	NIRI	2010-04-27	GN-2010A-Q-44
ULAS J1619+3007	GNIRS	2012-05-31	GN-2012A-Q-84
ULAS J1626+2524	IRCS	2010-04-05	o10121
ULAS J1639+3232	NIRI	2010-04-30	GN-2010A-Q-44
ULAS J2116−0101	GNIRS	2011-11-14	GN-2011B-Q-5
ULAS J2237+0642	GNIRS	2010-12-07	GN-2010B-Q-41
ULAS J2300+0703	NIRI	2009-06-15	GN-2009A-Q-16
ULAS J2315+0344	GNIRS	2011-12-24	GN-2011B-Q-43
ULAS J2318+0433	GNIRS	2012-06-02	GN-2012A-Q-84
ULAS J2326+0201	GNIRS	2011-11-28	GN-2011B-Q-43
ULAS J2331+0426	GNIRS	2012-06-06	GN-2012A-Q-84
ULAS J2342+0856	NIRI	2009-10-31	GN-2009B-Q-62
ULAS J2352+1244	GNIRS	2011-11-16	GN-2011B-Q-43
ULAS J2357+0132	GNIRS	2010-12-08	GN-2010B-Q-41

This paper has been typeset from a TEX/LATEX file prepared by the author.